MICROFLUIDIC SYNTHESIS AND PROPERTIES OF BIO-INSPIRED COLLOIDS

by

HARRY ZIJIAN AN

B.S. Chemical Engineering, Carnegie Mellon University (2008)
M. Eng. Chemical Engineering Practice, Massachusetts Institute of Technology (2014)

Submitted to the Department of Chemical Engineering
in partial fulfillment of the requirements for the degree of

Doctor of Philosophy in Chemical Engineering

at the

MASSACHUSETTS INSTITUTE OF TECHNOLOGY

August 2014 [September 2014]

Author Signature redacted
Department of Chemical Engineering
Mon Day, 2014

Certified by Signature redacted
Patrick S. Doyle
Professor of Chemical Engineering
Thesis Supervisor

Accepted by Signature redacted
Patrick S. Doyle
Professor of Chemical Engineering
Chairman, Department Committee on Graduate Students

Abstract

MICROFLUIDIC SYNTHESIS AND PROPERTIES OF BIO-INSPIRED COLLOIDS

by

Harry Zijian An

Submitted to the Department of Chemical Engineering on August 14, 2014
in partial fulfillment of the requirements for the degree of
Doctor of Philosophy in Chemical Engineering

Today, custom-tailored polymeric hydrogel microparticles are routinely used for drug delivery, medical diagnostics, as well as many fundamental studies in colloidal science. There is growing consensus that physical attributes, such as size, shape, internal structure, and mechanical deformability, of the particles can influence material performance, especially when they are placed into a biological setting. Over the past two decades, a host of particle fabrication techniques have been proposed, which are able to produce microgels with various physical properties, though maintaining independent control over them remains to be difficult. This thesis explores the synthesis of a new class of functional microparticles bearing the likeness of mammalian cells through the use of a new microfluidics-based lithography process, and demonstrates the utility of these biomimetic microparticles in novel biomedical applications.

First, we devise a microscope projection technique based on stop-flow lithography (SFL), which allows free-standing microparticles of any arbitrary 2D-extruded, mask-defined shape to be patterned down to the cellular size regime ($\leq$ 10 μm) from UV-crosslinkable oligomer formulations in a semi-continuous fashion. By modulating the degree of oxygen inhibition during synthesis, we achieve previously unattainable particle sizes. Brownian diffusion of colloidal discs in bulk suggests the out-of-plane dimension can be as small as 0.8 μm, which agrees with confocal microscopy measurements. We measure the hindered diffusion of microdiscs near a solid interface and compared our results to theoretical predictions. These biocompatible colloidal particles can also flow through physiological microvascular networks formed by endothelial cells undergoing vasculogensis under minimal hydrostatic pressure.

Second, inspired by the hierarchical structure of eukaryotic cells, we synthesize composite microparticles containing a homogenous distribution of hydrophobic compartments from crosslinkable silicone oil-in-water nanoemulsions. The nanoemulsion loadings achieved in our composite microgels have, to our knowledge, among the highest ever demonstrated in a hydrogel material. In addition, we perform proof-of-concept assays to show several orthogonal motifs, such as tunable hydrophobic anchoring at the oil/water interface and matrix degradation at high pH, by which both hydrophobic and hydrophilic compounds, including small molecules, proteins and the nanoemulsion droplets themselves, can be effectively encapsulated in and released from the resulting microparticles over a wide range of timescales.

Abstract

And last, we fabricate red blood cell-mimicking, oxygen-carrying composite microparticles from perfluorocalin-in-water nanoemulsions. Unlike silicone oil nanoemulsions, the PFD-based formulations require osmotic stabilization due to a finite solubility of oil in the aqueous continuous phase. The presence of perfluorocarbon oil droplets increases the solubility and diffusivity of oxygen in the prepolymer solution, thereby enhancing the rate of O_2 inhibition during microparticle synthesis. We develop a simple model that successfully predicts the augmented O_2 mass transport, which agrees well with experimental data. Encapsulating nanodroplets in the hydrogel network allows us to generate and preserve small droplets under nearly surfactant-free conditions via quick washing steps post-synthesis.

Thesis Supervisor: Patrick S. Doyle
Title: Professor of Chemical Engineering

ACKNOWLEDGEMENTS

I visited Cambridge, Massachusetts for the very first time soon after my arrival in the US, almost two decades ago. I still remember quite a few minute details about my first run-in with MIT: my younger self, sporting an oversized Nautica polo shirt, beige cargo shorts and a sheepish grin, standing in front of the McLaurin Building near the end of the short, self-guided tour. I knew, even back then, that earning an advanced degree was something I wanted to do (partly because similar educational opportunities were simply unavailable to my parents back in China). But, I could have never predicted the tortuous path that I took to make my aspirations a reality.

Working towards my Ph.D. has been one of the most humbling and rewarding experiences of my life. The past six years has dealt me an invaluable lesson in perseverance. A few months from now, I will surely walk away from graduate school more capable of solving difficult scientific problems, and recovering from unforeseen setbacks, than ever before.

Over my tenure at MIT, I have had the good fortune of learning from incredible mentors, who taught me the technical know-how to complete my thesis research.

First and foremost, I'd like to thank my advisor Prof. Pat Doyle. Pat, you painstakingly taught me how to think critically and pushed me to do impactful, original research. Your constant guidance is the singular factor that kept me on task, and gradually gave me the confidence to solve new and challenging problems.

Also, I'm grateful for the insightful questions and suggestions from my thesis committee, Profs. Krystyn Van Vliet and Brad Olsen.

I'm forever indebted to a trio of post-docs: Ramin Haghgooie, who showed me the basics of flow lithography in my first year; Matt Helgeson, who provided the much needed spark to jumpstart

my research at a time when nothing seems to work; and Burak Eral, my neighbor in the office and collaborator on multiple projects, who regularly provided valuable advice (on research, and life in general), and urged me to press on, even during the most trying of times.

I'd like to thank my fellow Doyle lab members, past and present, especially Rathi Srinivas, Will Uspal, Ben Renner, Lynna Chen, Jae Jung Kim, Jeremy Jones, Jane Hung, Ankur Gupta, Hyundo Lee, Alona Birjiniuk, Steve Chapin, Ki Wan Bong, Su Kyung Suh, Priyadarshi Panda. Special shout-out to Eric Safai, my very first UROP. I had a blast working alongside all of you. My graduate school experience would not be half of what it is now without being surrounded by such a driven, capable and caring group of scholars.

I'd also like to thank my collaborators from other labs: Michelle Chen (Kamm lab, MIT) and Dr. Katherine Whitehead (Anderson lab, MIT), and Doyle group administrative staff: Barbara Balkwill, Gwen Wilcox and Anton Janulis.

All my friends in Boston, who made this bustling city feel like a second home to me, especially Adam Wagner, Simon Choong, Kittipong Saetia, Jeffrey Mo, Vivian Hsieh, Bonnie Shum, Paul Minnice, Jon Chow, Nils Wernerfelt (and the rest of the TV group), Jen Lee, Yuko Kida, Steven Mikes, Scott Kaneshiro, Chris Mcguire and Alice Wang. You have each, in very unique ways, shaped my life outside of the lab.

And my close friends from high school and college: Lucy Xu, Hannah Xu, Andrew Hurrell, Monica Koncicki, Christine Han, Alice Chan, Andy Chang, Krishnan Aiyer, Catherine Huang, Christine Fong, Gabriel Huh, Ivan Lee et al., home is wherever you all are.

Many thanks to ABP, Chipotle and Starbucks, for breakfast, lunch/dinner and iced tea lemonades for the better part of the last 6 years.

Last but certainly not least, I want to acknowledge two of the greatest influences of my life: my parents. Mom, you have been my biggest supporter and most reliable caretaker from day one. Thank you, among *many* other things, for taking the time to call/text message me every day and to personally deliver homemade food from hundreds of miles away to Pittsburgh and Boston. Dad, you have worked so hard for so long in order to achieve the life we enjoy as a family, today. Thanks to both of you, for believing in me and my abilities, even when I didn't believe in myself.

This work was supported by the Institute for Collaborative Biotechnologies through grant W911NF-09-0001 from the U.S. Army Research Office. The content of the information does not necessarily reflect the position or the policy of the Government, and no official endorsement should be inferred.

TABLE OF CONTENTS

LIST OF FIGURES

LIST OF TABLES

CHAPTER 1

Introduction

1.1 Motivation

Polymeric hydrogel microparticles are promising biomaterials for a wide range of medical applications, such as encapsulation and delivery of exogenous cargoes (e.g., chemotherapeutics, imaging contrast agents) [1], diagnostics of disease biomarkers [2, 3], as well as fundamental studies of cellular interactions. Recently, substantial effort has been undertaken towards mimicking key physicochemical attributes of mammalian cells – including their size, shape, hierarchical structure, and mechanical deformability – using synthetic systems [4]. The inspiration for this is two-fold: first, most biological systems are soft, highly hydrated, and non-spherical, all of which are characteristics attainable using designer hydrogel microgels; and second, there is growing appreciation that eukaryotic cells resort to physics-derived mechanisms to overcome biological hurdles, recognize foreign objects, and to minimize off-target deposition.

A prime example of the latter is red blood cells. Owing to their unique morphology (8 μm x 2 μm biconcave discs, in humans) and elasticity, RBCs are optimized to reversibly deform so as to negotiate through narrow microvasculature and deliver oxygen for a prolonged period of time (~120 days) [5]. Several studies reported different schemes for generating biomimetic particles with RBC-like functional and structural properties. Haghgooie et al. fabricated PEG-based particles with size and shape reminiscent of RBCs that can pass through thin contractions under physiological driving pressures [6]. Doshi and coworkers created oxygen-carrying microparticles by incorporating hemoglobin via layer-by-layer assembly [7]. Merkel et al. and

Kozlovskaya et al. demonstrated prolonged circulation time and reduced cellular uptake for soft RBC-mimics [8, 9], respectively. These results are consistent with the slow clearance of 8 μm long cylindrical micelles [10]. Evidently, the combination of a clear, molecular understanding of the delivery strategies that are used by red blood cells, among other efficient biological carriers (e.g., pathogens [11]), and versatile particle fabrication methods will ultimately result in advanced cargo carriers and other particle-based biotechnology devices.

1.2 Current Synthesis Methods

Over the course of the past decade, a variety of synthesis techniques have been proposed for generating non-spherical, anisotropic microparticles, including self-assembly [12, 13], template molding [14], electrohydrodynamic cojetting [15], droplet microfluidics [16], layer-by-layer assembly [17], photolithography [18, 19], template stretching [20, 21], and so on [22]. However, not all techniques can freely access the same particle architecture, material composition, or length scale. More importantly, custom tailoring physicochemical attributes of the particles *independently* remains a difficult task. For example, self-assembly of block copolymers gives rise to colloidal micellar strutures with a highly polydisperse size distribution and limited morphologies (e.g., spheres, cylinders). Similarly, although electrohydrodynamic cojetting can be used to generate many unique, non-equilibrium particle morphologies, its ability to do so is intimately tied to processing conditions (e.g., flow rate, polymer concentration). And lastly, monodisperse microparticles (and vesicles [23]) fabricated using droplet microfluidics are often limited to spheres or deformations thereof by surface tension forces.

1.3.1 *Stop-flow lithography*

Recently, Doyle and coworkers introduced a new particle synthesis method called stop-flow lithography (SFL) that is capable of efficiently generate monodisperse hydrogel microparticles [24]. We will use utilize different iterations of SFL throughout this work for particle synthesis. SFL combines the precise shape control intrinsic to microscope projection photolithography and the continuous processing capabilities of microfluidics [25]. To date, a wide variety of simple, composite and multifunctional particles of different shapes, sizes and chemistries have been successfully prepared using SFL (Fig. 1.1). A wide spectrum of desirable characteristics has been conferred upon as-prepared microparticles, including mechanical deformability (Fig. 1.1A), biocompatibility (Fig. 1.1C), field-responsiveness (Fig. 1.1E) and degradability (Fig. 1.1F) [26-29]. Interestingly, these particles can also be serves as templates for heterogeneous crystallization (Fig. 1.1B) and growth of magnetic nanoparticles (Fig. 1.1H) post synthesis.

SFL essentially consists of three steps, repeated in a cyclic fashion: 1) stopping the flow of a photo-curable prepolymer solution; 2) flashing a pulse of mask-defined ultraviolet (UV) light into the stagnant prepolymer stream, the exposed portions of which are crosslinked, leading to the formation of solid structures almost instantaneously; 3) the particles formed are then driven out of the microchannel via a controlled pressure pulse for particle recovery. The main advantages of SFL over traditional lithography include the ability to process hydrogel precursors and other nontraditional photoresist materials, co-flow multiple laminar streams to produce layered/striped particles, and utilize low-cost transparency photomasks for rapid prototyping of new ideas.

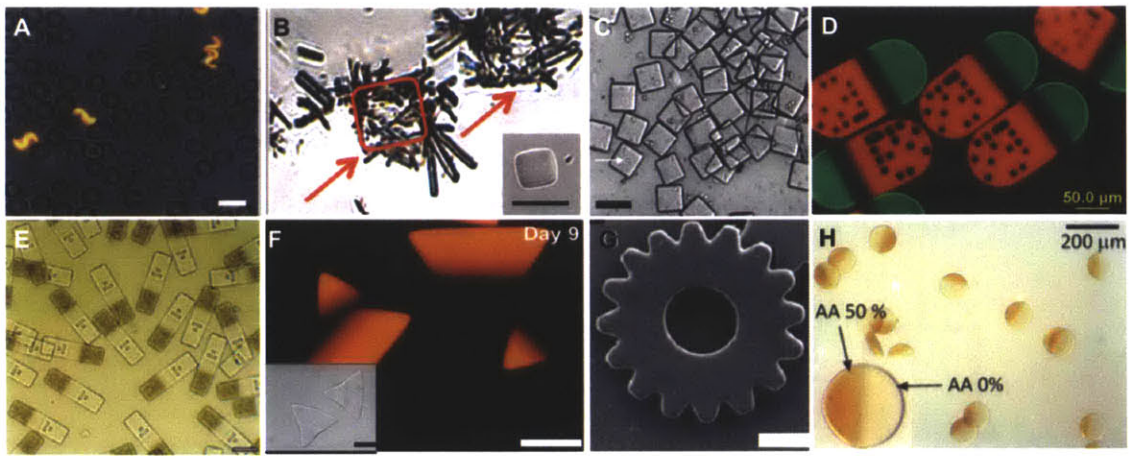

Figure 1.1 – Particles synthesized using stop-flow lithography (SFL): (A) composite bright-field and fluorescent images of diluted human whole blood (grayscale) and PEG S-shaped particles (fluorescent) mixed together in PBS [6]. (B) Carbamazepine (form II) needles grown on cuboid microparticles (red contour, inset) [30]. (C) Cell-laden microblocks (arrow points an encapsulated mouse fibroblast cell) [31], (D) multifunctional bar-coded particles [32], (E) magnetic bar-coded particles [33], (F) composite multi-block hydrogels formed by co-flowing three streams: diacrylate PLA-*b*-PEG-*b*-PLA [PLA = poly(lactic acid)] 20 wt % in the middle stream and PEG-DA 30 wt % in each side stream, only the center block is degradable, inset in (F) shows bright-field image of intact triangular-shaped particles [34]. (G) SEM image of a dried glassy silica microgear [35], (H) magnetic nanoparticles grown on Janus hydrogel discs containing carboxyl groups (AA = acrylic acid) [36]. Scale bars are 10 µm in (A), 50 µm in (B), (D) and (G), 100 µm in (C), (E) and (F), 200 µm in (H).

The ability to generate free-standing microstructures using SFL can be attributed to the presence of oxygen-induced inhibition of polymerization at the surfaces of the poly(dimethylsiloxane) (PDMS) microfluidic device. During the polymerization process, oxygen continuously diffuses through the porous PDMS channel walls and reacts with free radicals, converting them to chain-terminating peroxide species [37]. This results in the formation of a thin, uncrosslinked lubricating layer of prepolymer, $\delta \sim O(1\ \mu m)$, near the PDMS walls that enables the particles to flow without adhering to the walls of the device. A schematic of the SFL setup is shown in Fig. 1.2.

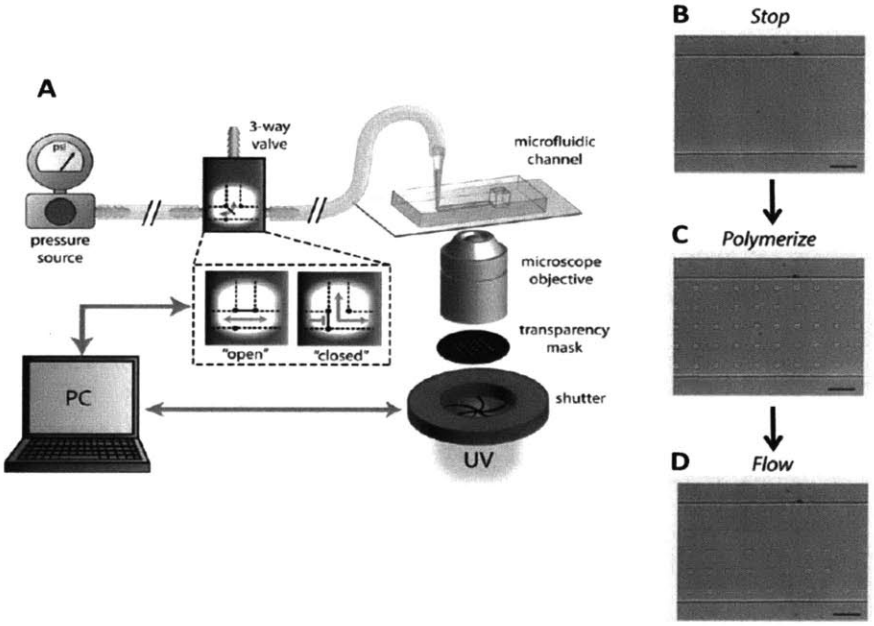

Figure 1.2 – Stop-flow lithography setup. (A) Schematic showing the computer-controlled flow setup. Prepolymer solution flowing within a microfluidic channel are driven using a pressure profile provided by a computer controlled 3-way solenoid valve that alternates between atmospheric pressure (closed) and a specified input pressure (open). The computer also controls the exposure time provided by the shutter. (B)-(D) Microscope images showing the three states of the process. In the first state (stop), the flow is stopped by closing the 3-way valve. In the second state (polymerize), an array of particles is polymerized into the stationary monomer film by opening the shutter while keeping the 3-way valve closed. In the third state (flow), polymerized particles are flushed out of the channel by opening the 3-way valve while keeping the shutter closed. The scale bars shown in (B)-(D) are 50 μm. Schematics are taken from ref. [25].

In order to generate particles with good shape fidelity, the duration of UV exposure should exceed the induction time, τ_i, which is necessary to deplete the prepolymer solution of oxygen, thereby allowing polymerization to proceed [37]. τ_i scales inversely with the Damköhler number, Da, which denotes the competition between oxygen inhibition (or reaction) and oxygen diffusion:

$$Da = \frac{\varphi \varepsilon [PI] I_o H^2}{D[O_2]_{eqb}} \tag{1.1}$$

where φ is the quantum yield of formation of initiating radicals, ε is the molar extinction coefficient of the photo-initiator at 365 nm, $[PI]$ is the photo-initiator concentration, I_o is the

light intensity, H is the channel height, D is the diffusivity of oxygen in the prepolymer solution, $[O_2]_{eqb}$ is the equilibrium concentration of oxygen in the prepolymer solution [25]. For effective synthesis, Da should be $\sim O(10)$. The quadratic dependence of Da on H is, in part, why synthesizing microparticles down to the cellular length scale ($\sim O(10$ um)) and below is technically challenging.

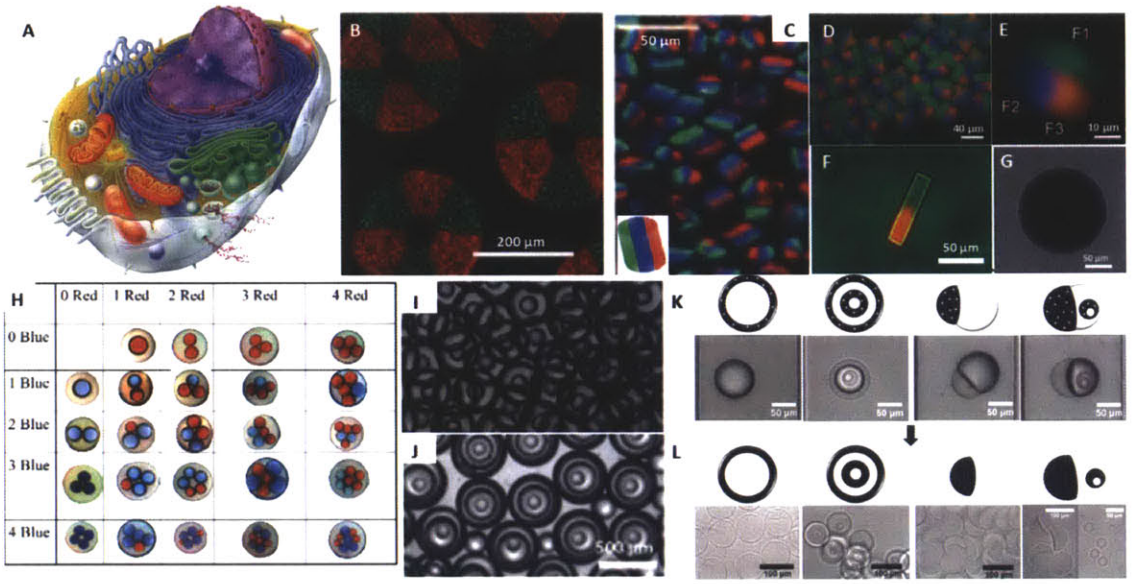

Figure 1.3 – Examples of compartmentalized particles synthesized to date. (A) Schematic diagram (taken from *http://gardeningstudio.com/eukaryotic-cells/*) showing the compartmentalized organization within a representative eukaryotic cell. (B) Hollow microfibers with six-compartmental shell layers [38]. (C) Poly(lactic-co-glycolic acid) tri-phasic microcylinders (inset: schematic) [39]. (D) Dual-axis tri-compartmental particle [40]. (E) Close-up side view of a particle shown in (C), scale bar is 10 μm. (F) Janus, bi-compartmental particle. Diffusion-limited mixing is seen at the interface between the two halves of the particle [41]. (G) Temperature-sensitive *N*-isopropylacrylamide particle containing hexadecane nanodroplets (~400 nm, 10% v/v) [42]. (H) Monodispersed double emulsion containing distinct number/type (blue or red) of inner compartments [43]. (I) Triple and (J) quadruple emulsion containing two or more nested compartments for simultaneous encapsulation of incompatible actives [44]. The emulsion droplets can be solidified into anisotropic microparticles by photopolymerization. (K) Schematics and images of multiple emulsions undergoing phase separation and de-wetting induced by the partitioning of photoinitiator and surfactant, respectively [45]. (L) Particles produced through photopolymerization of the compound droplets shown in (K); from left, hollow microcapsules with ultra-thin shells, onion microcapsules, hemispheres, and hollow microcapsules with thick shells.

1.3 Compartmentalized Microparticles

Compartmentalization is one of the universal architectural features of eukaryotic cells that sets them apart from other more primitive forms of life. The interior of eukaryotic cells contains numerous membrane-bound structures (i.e., organelles), within which multiple, often competing, biochemical reactions occur simultaneously. A typical mammalian cell is depicted schematically in Fig. 1.3A. Realization of this abundant natural concept in the form of synthetic microparticles can give rise to versatile vehicles for *carrying, protecting and directing* valuable therapeutic cargoes and other emerging biomedical applications. Multicompartmental particles can be independently loaded with different payloads (e.g., biologicals, hydrophobic drugs, dyes),

and be made using different matrix materials, which enable further surface functionalization and control over particle rigidity, permeability, release rate and environmental responsiveness (to changes in pH, osmolarity, temperature, etc).

Up until now, however, only a limited number of studies managed to create designer multicompartmental particles. Fig. 1.3 highlights some recurring motifs: core-shell capsules, higher-order emulsion droplets, as well as layered or striped patterns. Unlike existing bottom-up methods, which typically rely on self-assembly, emerging particle technologies (e.g., droplet microfluidics [16], flow lithography, electrohydrodynamic spraying) utilize simple fluid manipulations, followed by rapid phase transitions to achieve unique, non-equilibrium particle structures. One of the major technical limitations of these versatile top-down methods has been the difficulty with synthesizing compartmentalized particles with size in the cellular regime (note the scale bars in Fig. 1.3).

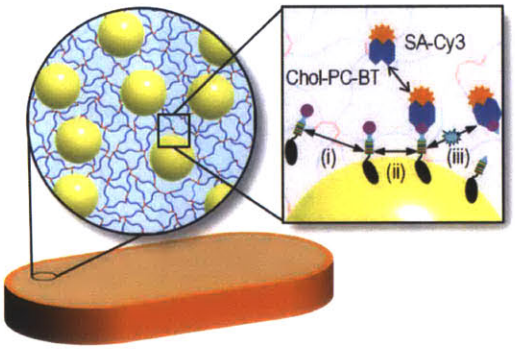

Figure 1.4 – Schematic diagram of a tablet-shaped nanoemulsion composite microparticle containing functionalizable oil/water interfaces, for encapsulation (i)-(ii) and release (iii) of fragile active compounds.

Consequently, motivated by the need to generate truly cell-like synthetic microparticles, we sought to advance the synthetic capability of SFL. We explore flow lithography under controlled oxygen environments (Chapter 2) as a way to generate *cell-sized, composite microparticles with stable internal compartments* from polymerizable nanoemulsions (which are metastable nano-sized dispersions consisting of two immiscible fluids, frequently used in cosmetic and food-related applications, see ref. [46], for example). The anisotropic nature of the composite particles dramatically enhances their overall functionality (Fig. 1.4), as we will show in Chapters 4 and 5.

1.4 Thesis Organization

This thesis is broken down into several parts. Following a brief introduction, the workhorse flow lithography technique used throughout this work is presented. Next, characterization and novel applications of designer polymeric materials will be explored as individual case studies. Lastly, a few final words on the future directions of this research will be discussed. Specifically,

Chapter 1 discusses the motivation and general scope for this work.

Chapter 2 presents oxygen-controlled stop-flow lithography technique, the method we use to synthesize colloidal and nanoemulsion composite hydrogels.

Chapter 3 describes several applications of non-spherical colloids synthesized using O_2-controlled SFL, focusing in particular on 1) their Brownian dynamics near a solid interface, and 2) their ability to navigate through microvascular networks.

Chapter 4 describes the synthesis of composite microparticles from crosslinkable silicone oil-in-water nanoemulsions. We perform demonstrative assays to show the utility of these particles in the encapsulation and controlled release of model actives.

Chapter 5 describes the synthesis of red blood cell-mimicking (~10 μm) composite microparticles from crosslinkable perfluorodecalin-in-water nanoemulsions. We propose engineering solutions to address the issue of emulsion instability and enhanced oxygen mass transport during photopolymerization.

Chapter 6 summarizes the conclusions from this work and comments on future direction.

CHAPTER 2

Oxygen-controlled Stop-flow Lithography

2.1 Overview

To begin, we introduce the mechanics of the photolithography synthesis approach, derived from stop-flow lithography (SFL), that we use to generate biomimetic colloidal (Chapter 3) and compartmentalized (Chapter 5) particles with any 2D-extruded shape.

The results presented in here are adapted from a recently accepted *Soft Matter* article.

2.2 Introduction

Controlled synthesis of non-spherical microparticles is an important problem in biomaterial design and drug delivery. Deviation from simple spherical symmetry in particle architecture dramatically improves the utility of these particles in a wide spectrum of biomedical applications, including multiplexed sensing and diagnostics of clinically relevant disease markers [33, 47], mimicry of naturally occurring biological entities (such as red blood cells [6-8, 48, 49] or platelets [50, 51]), programmed encapsulation of drugs and imaging probes [52, 53], followed by their systemic or targeted delivery in due course.

In general, performance of designer particulate systems is the product of a complex interplay of material characteristics. This is especially true for microfabricated drug delivery vectors:

modulating the size [54, 55], shape [56], elasticity, and surface chemistry of the particles has been shown to delay internationalization by immune cells[54], influence intracellular trafficking [57, 58], and prolong *in vivo* circulation [8, 59].

In order to elucidate a complete set of design criteria for maximizing selectivity at the cell and tissue levels, synthesis methods need to afford independent control over the physicochemical properties of the resulting particles. A variety of versatile top-down particle fabrication techniques have emerged in the past decade, chief among them microfluidics [60], lithography [14], electrospraying [15], template stretching [20, 21], or combinations thereof [25, 41]. However, not all techniques can freely access the material composition, particle architecture, or length scale ($\leq 10\mu m$) relevant to biological assays, especially cellular uptake, and intravenous injections. For example, particles synthesized using droplet microfluidics are often restricted to spheres or deformations thereof due to surface energy minimization, with characteristic size $\sim O(10\mu m)$. Electrohydrodynamic jetting can be used to create many unique non-equilibrium particle structures. However, its ability to do so hinges heavily on prepolymer flow characteristics, which varies according to particle composition. Up to now, techniques for generating geometrically-complex, and structurally-anisotropic microparticles with size in the colloidal regime remain elusive.

To ameliorate the experimental bottleneck on biocompatible anisotropic microgel synthesis, we developed a modified flow lithography technique. This versatile method builds upon stop-flow lithography [25] (SFL), which allows microparticles of any 2D-extruded, mask-defined shape to be patterned from UV-crosslinkable oligomer formulations in a semi-continuous fashion. With the exception of an additional conditioning step (see section 2.4 for details), modified SFL and its predecessor essentially consist of the same three steps, repeated in a cyclic fashion: 1) stopping the flow of a photo-curable prepolymer solution; 2) flashing a pulse of mask-defined ultraviolet (UV) light into the stagnant prepolymer stream, the exposed portions of which are crosslinked, leading to the formation of solid structures almost instantaneously; 3) the particles formed are then driven out of the microchannel via a controlled pressure pulse for particle recovery.

During normal operation, oxygen, a polymerization inhibitor, rapidly diffuses through the PDMS sidewalls, and gives rise to lubricating layers of thickness δ above and below the particle. However, this fortuitous ability to easily create free-standing structures, but leads to other problems: δ limits the feature resolution of the technique to ~ 2 μm in the out-of-plane direction [6]. By controlling the inhibitory effects of ambient oxygen [37] via simple purge (Fig. 2.1), the improved experimental setup extends the particle synthesis capabilities of SFL to ~ 5 μm in diameter (in-plane resolution) and sub-micron in height, simultaneously. In comparison, 5 μm diameter cylinders can only be synthesized via SFL using devices that are at least 10 μm tall [25]. We will discuss in greater detail regarding how we went about experimentally validating the minimum achievable feature size in the next chapter.

2.3 Experimental Method

2.3.1 Materials

Solutions of poly(ethylene glycol) diacrylate (PEG-DA, M_n = 700 g/mol, Sigma Aldrich) and 2-hydroxy-2-methyl-1-phenyl-propan-1-one (Darocur® 1173, Sigma Aldrich) were used for

particle synthesis. Methacryloxyethyl thiocarbamoyl rhodamine B ($\lambda_{ex}/\lambda_{em}$ = 548/570 nm, Polysciences) was used to label the gel particles for fluorescence imaging.

2.3.2 Microfluidic devices

The microfluidic devices were prepared using standard soft-lithography molding by pouring polydimethylsiloxane (PDMS, Sylgard 184, Dow Corning) in a 10:1 (monomer to curing agent) onto a 4 inch silicon wafer containing positive-relief SU-8 features. The devices were fully cured in an oven overnight at 65°C. Access ports were bored into each device using a syringe needle (blunt tip) to enable solution flow. Devices were then placed on glass slides spin-coated with PDMS (~1 mm) to ensure that the prepolymer solution was exposed only to PDMS surfaces during synthesis. Procedures for device fabrication and assembly are discussed in detail elsewhere [61].

The devices used for particle synthesis contain parallel rectangular channels 100 μm in width and 2 μm in height. Thickness over the synthesis section of each device was tuned between 1 to 3 mm by varying the amount of PDMS used. To make tiered synthesis devices (Fig. 2.5), a second layer of PDMS was poured near the inlet and outlet reservoirs to support modified pipette tips [62] (used to inject prepolymer mixtures) and blunt needles (used to collect particles).

The synthesis devices were placed inside a custom-made sealed chamber with multiple purge gas inlet and outlet apertures, and mounted on an inverted microscope (Axiovert 200, Zeiss). A prepolymer mixture consisting of 80% (v/v) PEG-DA, 15% (v/v) photoinitiator and 5% (v/v) fluorescent dye stock solution (1 mg/mL PEG200) was injected into a synthesis device using modified pipette tips (Molecular BioProducts) under moderate forcing pressure (~4 psi). Concurrently, air and argon purge streams (DPG4000-30, Omega) were introduced into the chamber according to a predetermined calibration curve to achieve a targeted oxygen concentration, between 0% and 21%. The enclosed microfluidic device and prepolymer mixture were allowed to equilibrate with the exchanged gas mixture for up to 90 minutes, depending on the device thickness.

2.3.3 Photopolymerization setup

Phtomasks designed using Autocad were plotted with 32,512 dpi resolution using Fineline Imaging (Colorado Springs, CO). The masks were inserted into the field-stop plane of a Zeiss Axiovert 200 inverted microscope. Colloidal microparticles were patterned by projecting mask-defined UV light from a Lumen 200 metal arc lamp (Prior Scientific, 100% setting) through a wide excitation UV filter set (300-380 nm, 11000v2 UV, Chroma Technology) using a 20x objective. A shutter system (VS25, Uniblitz) interfaced with a custom-written Python automation script precisely controlled the duration of UV exposure. Microparticle formation was visualized *in situ* using a cooled interline charge-coupled device camera (Clara, Andor).

2.3.4 *Determination of oxygen concentration in purge chamber*

The gas-phase oxygen concentration inside the purge chamber was monitored non-invasively using the RedEye™ oxygen sensing patches (Foxy, Ocean Optics) placed directly above the purge gas outlet (Fig. 2.1). The patches (a sol-gel matrix) contain immobilized indicator dyes that quench in the presence of oxygen molecules [63]. The degree of quenching correlates

quantitatively with the partial pressure of oxygen (pO_2) according to Stern-Volmer Equation, ${}^{t_0}/_{t} = 1 + K_{SV} pO_2$, where t_0 and t is the fluorescence lifetime in the absence and presence of oxygen, respectively, K_{SV} is the Stern-Volmer coefficient. Lifetime-based O_2 detection is a more robust, and quantitative alternative to traditional intensity-based detection methods, which are prone to photo-degradation.

Ambient oxygen concentration was varied from 0% to 20.9% by adjusting the relative flow rates of argon and air into the chamber, and measured from a linear calibration curve. A 2-point calibration was performed prior to each sensing experiment. Typically, fluorescence lifetime decreased from 2.848 μs for 0% oxygen to 1.990 μs for 20.9% oxygen.

2.4 Results

O_2-controlled flow lithography improvesupon a versatile lithography technique – SFL – introduced by Doyle and colleagues [25]. In conventional SFL, pulses of mask-defined UV light are projected through a microscope objective to generate free-standing gel structures within a microfluidic device. This method essentially converts any compound microscope into a particle printing press. The particles of height h are flanked above and below by lubricating layers of thickness, δ, which is normally ~O(1μm). The boundary of the inhibition layer is determined by the delicate balance between oxygen diffusion and consumption via the inhibition reaction with propagating oligomers.

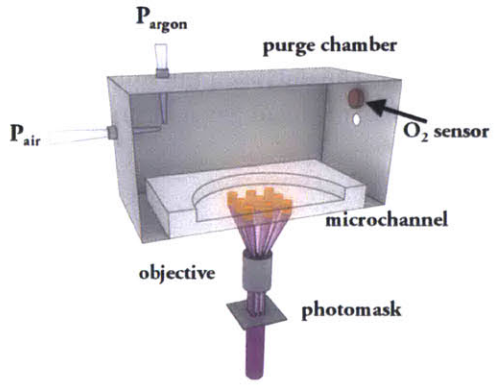

Figure 2.1 – Oxygen-controlled SFL experimental setup. Schematic diagram showing the fabrication of an array of colloidal discs under reduced oxygen atmosphere. A PEG-based prepolymer is flowed through a tiered PDMS synthesis device and polymerized via controlled pulses of mask-defined UV light through a microscope objective. The gel particles can then then advected downstream for collection. The synthesis device is placed in a custom-made purge chamber, which allows the exchange of an air/argon mixture to control the overall ambient oxygen concentration. A RedEye™ oxygen sensor patch is mounted above the gas outlet to measure the oxygen concentration.

The modified flow lithography experimental setup is shown in Fig. 2.1. We use a purge chamber in order to exercise control over the oxygen concentration in the immediate vicinity of the synthesis microfluidic device. The precise benefits of this apparatus will become clear soon. Suffice it to say that, for now, the chamber is made in-house and latches onto the microscope

stage. During particle synthesis, oxygen concentration inside the chamber can be altered by passing air and argon (which contains 20.9% and 0% O_2 by volume, respectively) in the desired proportions through the two purge gas inlet apertures. Placing the two nozzles at a right angle facilitates gas mixing. We maintain the flow rates of the purge gases for the duration of the experiment in order to prevent gas leakage through any microscopic cracks on the chamber walls (Fig. 2.2).

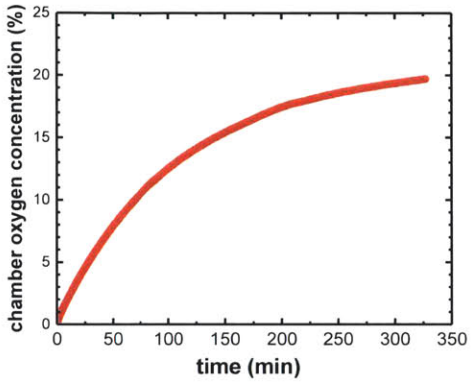

Figure 2.2 – Oxygen concentration in the purge chamber slowly approaches atmospheric conditions over time. The measurements were made using the RedEye™ probes starting from an initially argon-filled chamber. The gas inlet apertures were plugged in order to highlight alternative routes via which air can seep in.

Use of the purge chamber introduces an additional conditioning step in the normal experimental workflow. At the beginning of each synthesis experiment, a brief waiting period is required for 1) the individual purge gas streams to mix and 2) the microfluidic device and its contents to equilibrate with the air/argon mixture within the chamber. In practice, the former occurs more rapidly than the latter. We placed a RedEye™ oxygen sensor patch above the purge gas outlet to monitor the oxygen concentration in the gas phase (Fig. 2.1). The patch contains an immobilized dye molecule that quenches dynamically in the presence of O_2. To make chamber oxygen readings, we point a bifurcated optical fiber (RE-BIFBORO-2) at the RedEye™ patch. The fiber directs a blue LED excitation light toward the patch, and excites the sensor dye. The red emitted signal is then collected by the optical probe and transmitted to a fluorometer, which measures the fluorescence lifetime, t. t is related to the partial pressure of oxygen by the well-known Stern-Volmer equation [64]. Fig. 2.3 shows the chamber oxygen concentration as a function of time for a range of air inlet pressures. In all cases, the oxygen concentration reached an equilibrium value approximately 1 minute after the onset of purge, indicating efficient gas mixing.

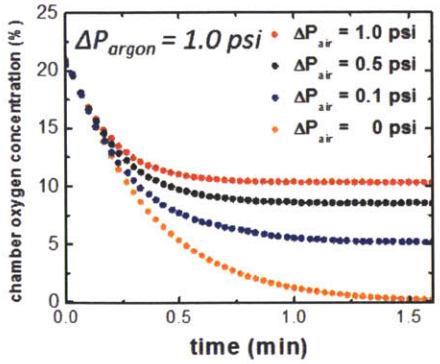

Figure 2.3 – Chamber oxygen concentration for a range of air feed pressures: 0 psi (orange circles), 0.1 psi (blue circles), 0.5 psi (black circles), 1.0 psi (red circles). Pressure of the argon stream is fixed at 1 psi. Efficient mixing at the gas stream inlets result in short time lags (< 1.5 min) until a final chamber oxygen concentration plateau is reached.

A second time delay is associated with the synthesis device and the prepolymer solution within coming to equilibrium with the surrounding chamber gas mixture. Duration of the delay or response time is determined by the thickness of the PDMS device. To demonstrate this, we assembled synthesis microchannels of varying thickness by pouring different amounts of PDMS onto the device wafer. The practical lower threshold (~2 mm) is set by the minimum height necessary to reliably secure fluidic connections into the device inlet and outlet reservoirs. Using a canonical composition (80% v/v PEG-DA700, and 15% v/v Darocur®1173, and 5% v/v rhodamine B), we synthesized cuboids of decreasing size in 2 μm tall channels under constant influx of pure argon (1.0 psi). Fig. 2.4 shows the time necessary for the smallest feature (5 μm square) to stick to the confining PDMS surfaces due to lack of oxygen inhibition near the channel periphery. The observed linear trend in log-log format, with a power-law slope of 0.5, is consistent with a simple diffusive mechanism, in which the PDMS layer above the synthesis device acts as the dominant barrier for mass transfer. We estimate the characteristic diffusion coefficient to be ~O(10^{-9}m^2/s), on par with the diffusivity of oxygen [65] and argon [66] through PDMS.

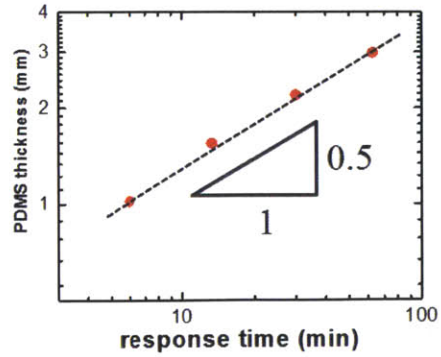

Figure 2.4 – Thickness of the PDMS synthesis device determines the threshold response time (defined as the duration of continuous gas purge needed to reach equilibrium). The measured response time obeys a power-law trend, with exponent of 0.5 (a dashed line is drawn to guide the eye), which suggests a simple diffusion-based mechanism, with a characteristic coefficient ~O(10^{-9}) m^2/s, typical of oxygen [64] and argon [65] diffusion through porous PDMS.

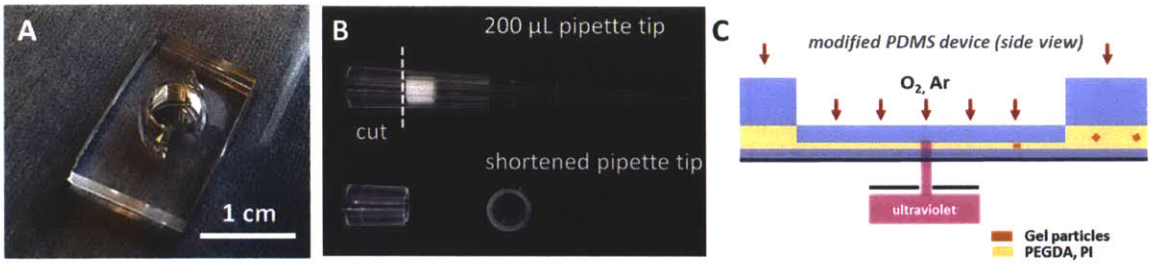

Figure 2.5 – Tiered microfluidic device: (A) Image of a tiered microfluidic device. Scale bar is 1 cm. (B) Shortened pipette tip (bottom, two orthogonal views) made from a 200 µL pipette tip (top) via the cut mark indicated by the dashed line. (C) Schematic of the tiered microfluidic device (not drawn to scale). Particle synthesis takes place in the center, where the PDMS slab is thinnest.

In order to limit the overall equilibration time prior to synthesis to ~5 min, we developed a tiered PDMS synthesis device (Fig. 2.5) using a two-step curing process. First, we poured a thin layer (~1 mm) of PDMS over the device wafer and partially cured in the oven at 65°C for ~25 min. Then, pipette tips (200 µL) were used to shield the central synthesis portion of each device and allow a second layer of PDMS to coat only the inlet and outlet regions, where rapid gas transport is unessential. The sacrificial pipette tips were removed from the wafer once the PDMS fully cured after baking overnight at 65°C.

Fabrication of free-standing gel particles using SFL requires non-zero oxygen concentrations in the purge chamber in order to avoid particle sticking. As such, we systematically calibrated the equilibrium chamber oxygen concentration for a wide range of air pressures using the RedEye™ sensor. The concentration measurements were collapsed using a simple model derived from the Blasius correlation for high Re flow in smooth pipes [67] (Fig. 2.6). This approach is justified since the Re for purge gas flow estimated using a typical pressure drop of 1 psi was >4000. Applying the Blasius equation, gas flow rate, Q_i, where i stands for either air or argon, can be expressed as:

$$Q_i = 2.26\left(\frac{\Delta P_i}{L_i}\right)^{4/7}(\rho_i{}^3\eta_i)^{-1/7}d^{19/7} \qquad (2.1)$$

$\Delta P/L$ is the pressure drop per unit length of tubing, d is the nozzle diameter (~1 mm), ρ and η are the density and kinematic viscosity, respectively. Therefore, setting $L_{argon} = L_{air}$, the volume fraction of air introduced Q_{air}/Q_{total} is:

$$\frac{Q_{air}}{Q_{total}} = \frac{\Delta P_{air}{}^{4/7}}{\Delta P_{air}{}^{4/7} + a\Delta P_{argon}{}^{4/7}} \qquad (2.2)$$

Here, $a = (\rho_{air}{}^3\eta_{air}/\rho_{argon}{}^3\eta_{argon})^{1/7}$ and is numerically equal to 0.845 once we substitute in values for the physical properties (Table 2.1). To achieve symmetric mixing, length of the tubing for the argon needs to be decreased by ~18%. The experimental data and model predictions (Fig. 2.6) are in excellent agreement.

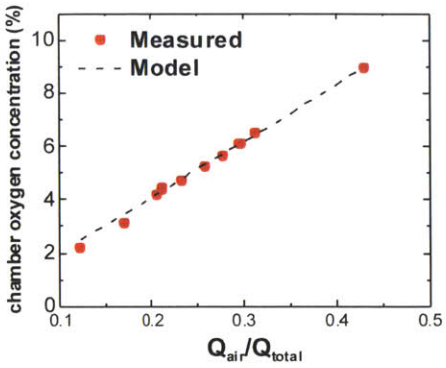

Figure 2.6 – Equilibrium oxygen concentration in the purge chamber as a function of volume fraction of air introduced. The empirical measurements (red circles) made using the RedEye™ oxygen sensors are in excellent agreement with a simple model of high Re gas mixing derived from the Blasius correlation (dotted line, Eq. (2.2)).

Table 2.1 – Density and viscosity values of air and argon at room temperature.

Parameter	Value	Units
ρ_{air}	1.20	kg/m^3
ρ_{argon}	1.66	kg/m^3
η_{air}	18.52	10^{-6} Pa s
η_{argon}	22.61	10^{-6} Pa s

2.5 Conclusions

In summary, we discussed the key differences between oxygen-controlled SFL and its predecessor. The modifications made facilitate (and are driven by) the synthesis of non-spherical colloidal and oxygen-carrying microparticles. We will present our accomplishments in each of those areas, sequentially, starting in the next chapter.

Finally, we refer readers to *Appendix A.1* for potentially helpful tips on how to use this technique.

CHAPTER 3

Sub-micron Tall Colloidal Microgels

3.1 Overview

Here, we show that by modulating the degree of oxygen inhibition during synthesis via the modified SFL process introduced earlier, we can achieve previously unattainable particle sizes. Brownian diffusion of colloidal discs in bulk suggests the out-of-plane dimension can be as small as 0.8 μm, which agrees with confocal microscopy measurements. We measured the hindered diffusion of microdiscs near a solid surface and compared our results to theoretical predictions. These colloidal particles can also flow through physiological microvascular networks formed by endothelial cells undergoing vasculogensis under minimal hydrostatic pressure.

The results presented in here are adapted from a recently accepted *Soft Matter* article.

3.2 Introduction

In this chapter, we substantiate the colloidal nature of the thin microparticles fabricated using oxygen-controlled SFL by examining their diffusion in bulk and near an interface. In the latter case, we construct a simple argument based on Boltzmann statistics for estimating the hindered diffusion coefficient near a planar wall.

In addition, we perform proof-of-concept experiments showing the flow of polyethylene glycol (PEG)-based hydrogel colloids through multi-culture microfluidic vascular networks (μVNs) formed by human umbilical vein endothelial cells undergoing vasculogenesis [68]. These self-organized, perfusable 3D μVNs were recently used to better understand extravasation events in tumor cell metastasis [69]. The *in vitro* microvascular network platform is a very useful tool for systematically studying transport of microparticles in real time, with increased physiological relevance compared to microfluidics-based flow assays (similar to other bio-inspired experiments [6, 70]).

3.3 Experimental Method

3.3.1 Materials

Solutions of poly(ethylene glycol) diacrylate (PEG-DA, M_n = 700 g/mol, Sigma Aldrich) and 2-hydroxy-2-methyl-1-phenyl-propan-1-one (Darocur® 1173, Sigma Aldrich) were used for particle synthesis. Methacryloxyethyl thiocarbamoyl rhodamine B ($\lambda_{ex}/\lambda_{em}$ = 548/570 nm, Polysciences) was used to label the gel particles for fluorescence imaging.

3.3.2 Particle synthesis

All of the particles shown here were prepared using the modified stop-flow lithography (SFL) technique described in the previous chapter.

3.3.3 Particle characterization

3.3.3.1 Particle diffusivity measurements

We used multiple particle tracking to measure the diffusion coefficient of colloidal discs suspended in aqueous buffer with 0% or 90% deuterium oxide, by volume. Particle samples (~30 μL) were loaded into observation chambers that consist of two parallel strips of parafilm sandwiched between a glass slide (24 mm x 60 mm, No. 1.5, VWR) and a coverslip (18 mm x 18 mm, VWR). Prior to assembly, the slide and coverslip were immersed in a base bath (1M NaOH), rinsed with DI water and ethanol, and dried with compressed argon. The chamber was sealed on all sides by a thin layer of ultraviolet-cured optical glue (#65, Norland) to minimize drift and prevent evaporation.

The slides were transferred to an inverted microscope (Axiovert 200, Zeiss) equipped with an EC Plan Neofluar® objective (40x, NA = 0.75) and observed under fluorescence mode. Movies of up to 2500 frames were recorded using a cooled interline CCD camera (Clara, Andor) at a rate of 13.6 fps with an exposure time of 20 ms to minimize dynamic error. We used a public-domain MATLAB algorithm written by Kilfoil and coworkers [71] to extract two-dimensional particle trajectories from the movies. To extract particle mobility, trajectories were averaged to obtain the unbiased mean-squared displacement (MSD), $\langle \Delta R(\tau) \rangle$ as a function of lag time, τ. The static error ($\bar{\xi}^2$) due to camera noise was deduced from MSDs of immobilized discs at short lag time [72] to be 10^{-4} μm^2.

3.3.3.2 *Confocal microscopy*

Colloidal microparticles were immobilized in a viscous solution (2% alginate , $\eta/\eta_{water} = 18$) [73] and loaded into a thin observation chamber. A confocal laser scanning microscope (LSM 700, Zeiss) equipped with a high numerical aperature, oil immersion objective (NA = 1.3) was used to best resolve the out-of-plane dimension. Successive x-y scans were acquired under fluorescence ($\lambda = 568$ nm) at intervals of 60 nm through representative particles. The images were processed using the 3D viewer feature in ImageJ (NIH).

3.3.3.3 *Numerical solutions of mass transport equations*

The simulation results shown in Fig. 3.1 were obtained by numerically integrating the conservation equations for oxygen and unconverted oligomers using a custom-written script in Fortran 77. Eq. (3.4) and (3.5) were discretized into 500 uniform mesh elements along the channel height (z) direction between 0 (channel bottom) and 1 (channel top), and propagated in dimensionless time intervals of 10^{-6} for $\geq 10^4$ steps.

3.3.3.4 *Particle flow experiments*

The vasculogenesis flow devices (height = 100 μm) were molded in PDMS and permanently bonded to glass slides via oxygen plasma treatment. Device contains three parallel, spatially segregated gel regions. Each gel region is flanked by medium channels to provide adequate nutrients and gas exchange, and direct access to the openings of the vasculature. Human umbilical vein endothelial cells (HUVECs) were encapsulated in fibrin gels and cultured alongside human lung fibroblasts (HLFs). Two columns of equally spaced trapezoidal PDMS posts, one on either side of the central HUVEC gel region, were introduced to 1) enable uniform gel-fluidic interfaces, and 2) minimize spillage into medium channels during gel filling. HLFs prevent nascent vascular networks from regressing after ~4 days under non-contact co-culture conditions. For detailed procedures for device assembly, cell culture, and gel filling, see ref. [68].

To introduce colloidal particles into the microvascular networks, media from the reservoirs of the two channels flanking the endothelial cell channel was aspirated and 40 μL of the particle suspension containing ~300,000 particles/mL was deposited into one of the reservoirs connected to the central media channel. This creates a pressure drop of 5.2 mmH_2O across the vascular network, drawing the particles into the vasculature.

Videos were recorded, under both fluorescence and DIC conditions simultaneously on an Olympus confocal microscope (10x objective, 2.4x optical zoom) at a frame rate of 0.33 fps. Composite images were created using ImageJ showing the outlines of the microvascular network and the particle trajectory.

After the flow experiment, vessels were fixed with 4% paraformaldehyde (Electron Microscopy Sciences) for 15 min, permeabilized with 0.01% Triton X (Sigma) and stained for actin using Alexa Fluor® 488 Phalloidin (Invitrogen) at 1:200 dilution. Fluorescent confocal images (Olympus IX81) were then taken and processed using the IMARIS imaging software (Bitplane).

3.4 Results

3.4.1 Modeling of photopolymerization

The importance of controlling ambient oxygen concentration in enabling thin particle synthesis can be understood using a simple reaction-diffusion model. This one-dimensional description of particle formation in a microfluidic channel was first formulated by Dendukuri et al [37]. It has since been adapted [74] and further validated via experiments [48].

This model considers the spatial and temporal variation of dissolved oxygen concentration [O_2] and un-crosslinked oligomers [M] within a prepolymer mixture between confining PDMS channel boundaries (z-direction). Using mass action kinetics, we can write the governing equations as:

$$\frac{\partial[O_2]}{\partial t} = D_{ox}\frac{\partial^2[O_2]}{\partial z^2} - k_o[O_2][\dot{X}] \tag{3.1}$$

$$\frac{\partial[M]}{\partial t} = -k_p[M][\dot{X}] \tag{3.2}$$

The RHS terms of Eq. (3.1) correspond to oxygen diffusion in the prepolymer (with D_{ox} as the diffusion coefficient) and reaction with propagating radical species, $\dot{X}$ (with rate constant k_o), respectively. This model neglects the diffusion of oligomers due to their bulky size relative to that of oxygen. As a result, only the propagation reaction (with rate constant k_P) contributes to the decrease in [M] over time. The two expressions are coupled via the inhibition reaction where oxygen quenches further polymerization by reacting with propagating radical species. $[\dot{X}]$ can be estimated by invoking the quasi-steady state approximation, and setting the rate of radical generation (r_a) in a thin film of prepolymer at height z equal to the rate of consumption by the inhibition and termination reactions:

$$[\dot{X}] = \frac{-k_o[O_2]+\sqrt{(k_o[O_2])^2+4k_t r_a}}{2k_t} \tag{3.3}$$

where $r_a = \psi\varepsilon[PI]I_o exp(-\varepsilon[PI]z)$. ψ is the quantum yield of the initiating radical species. ε and $[PI]$ is the molar extinction coefficient (at 365 nm) and concentration of the photoinitiator, respectively. I_o is the incident light intensity. k_t is the rate constant for the bimolecular termination reaction. For detailed derivation of the model equations and full reaction mechanism, see ref. [37].

The governing equations, Eq. (3.1) and (3.2), can be non-dimensionalized using

$$\tau = tD_{ox}/H^2 \qquad \eta = z/H$$
$$\theta = [O_2]/[O_2]_{eq} \qquad \xi = [M]/[M]_0$$

to obtain:

$$\frac{\partial\theta}{\partial\tau} = \frac{\partial^2\theta}{\partial\eta^2} - Da_1\theta\left(-\theta + \sqrt{\theta^2 + \alpha\, exp(-\beta\eta)}\right) \tag{3.4}$$

$$\frac{\partial\xi}{\partial\tau} = -Da_2\xi\left(-\theta + \sqrt{\theta^2 + \alpha\, exp(-\beta\eta)}\right) \tag{3.5}$$

where H is the channel height, $[O_2]_{eq}$ is the equilibrium concentration of dissolved oxygen in the oligomer, and $[M]_0$ is the initial concentration of oligomer species. Resulting expressions for the dimensionless parameters are as follows:

$$Da_1 = \frac{k_O{}^2 H^2 [O_2]_{eq}}{2D_{ox}k_t} \qquad Da_2 = \frac{k_p k_O H^2 [O_2]_{eq}}{2D_{ox}k_t}$$

$$\alpha = \frac{4\psi\varepsilon[PI]I_o k_t}{Ek_O{}^2[O_2]_{eq}{}^2} \qquad \beta = \varepsilon[PI]H$$

Da_1 and Da_2 are Damköhler numbers. The former quantifies the relative rates of oxygen inhibition and oxygen diffusion, while the latter quantifies the relative rates of chain propagation and oxygen diffusion. We note that the expression for α differs from its counterpart in the original contribution by a factor of E, which denotes the energy content of a mole of photons at 365 nm (328 kJ/mol) [37]. This conversion factor was not explicitly stated previously. However, we do so here to maintain dimensional consistency.

Table 3.1 – Summary of model parameters used in the simulation.

Parameter	Value	Units	Source
k_p	25	$m^3/mol\ s$	ref [75]
k_t	2.52×10^3	$m^3/mol\ s$	ref [75]
k_o	5×10^5	$m^3/mol\ s$	ref [76]
D_{ox}	2.84×10^{-11}	m^2/s	ref [77]
H	2	μm	Measured
I_o	1.25×10^4	W/m^2	Measured
$[PI]$	990	mol/m^3	Calculated
ε	1.6	$m^3/mol\ m$	ref [78]
$[O_2]_{ea}$	1.5	mol/m^3	ref [79]
φ	0.6	-	ref [78]

To computationally show the feasibility of creating thin particles by controlling the chamber oxygen concentration, we numerically integrated Eq. (3.4) and (3.5) to obtain θ and ξ given the parameters listed in Table 3.1 and the following boundary conditions:

$$\theta(0,\tau) = 1$$
$$\theta(1,\tau) = 1$$
$$\theta(\eta,0) = 1$$

which assume that the oligomer contains its equilibrium concentration of O_2 both initially and at the PDMS walls.

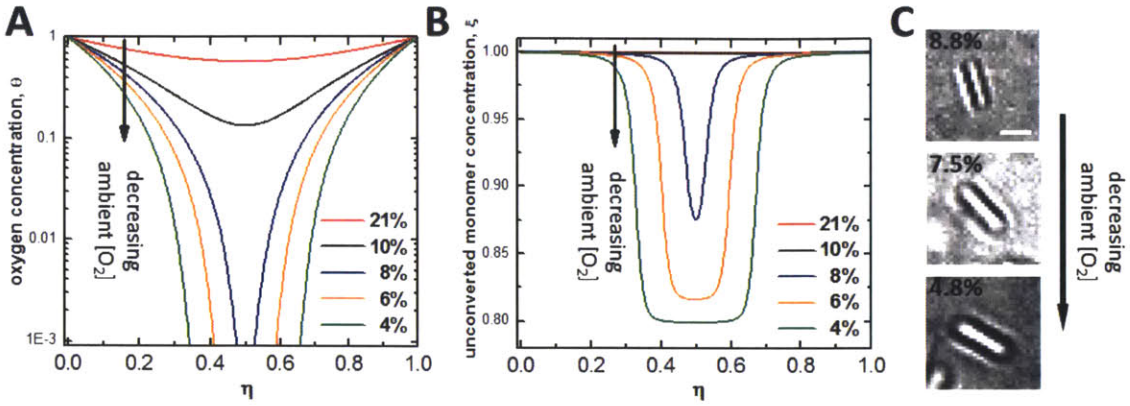

Figure 3.1 – Steady state profiles of oxygen (θ) and unconverted monomer concentration (ξ) as a function of non-dimensionalized channel height (η). The results shown in (A) and (B) were obtained by numerically integrating Eq. (3.4) and (3.5) using the parameter values listed in Table 3.1 for a range of ambient oxygen concentrations. Decreasing ambient O_2 concentration leads to a reduction in oxygen penetration depth near the channel walls, where rapid oxygen diffusion prevents particle formation. Cross-linked structures start to grow from the channel center as θ and ξ fall below a critical threshold value ($\theta_c \sim 10^{-3}$, $\xi_c = 0.98$) for gelation. Modulating the chamber $[O_2]$ allows particle height to approach the sub-micron regime. (C) A series of bright-field micrographs showing the change in height of 10 μm diameter discs for a range of chamber $[O_2]$ (noted in the upper left corner). Above ~10%, no particles can be made, in agreement with model predictions. Scale bar is 5 μm.

In order to vary $[O_2]$ in the chamber, we assumed 1) the equilibrium dissolved oxygen concentration $[O_2]_{eq}$ in the prepolymer mixture obeys Henry's law, with a proportionality constant k_H of 140 L atm/mol; and 2), $[O_2]_{eq}$=1.5 mol/m^3 under standard ambient conditions (20.9% O_2). Simulation results for τ = 0.1 are shown in Fig. 3.1. Physically, this corresponds to ~100 ms for a 2 μm tall device, similar to exposure times used during synthesis. Keeping the exposure time short helps to generate more uniform particles [80].

At high chamber oxygen concentrations (≥ 10%), transport of oxygen near the channel interfaces occurs rapidly and prevents particle formation. Here, we adopt the convention that gelation occurs when monomer conversion first reaches 2% (ξ_c = 0.98), similar to what was done previously [37]. Below 10% O_2, the propagation reaction dominates the inhibition reaction between radical species and dissolved oxygen. As a result, particles grow from the channel center, where the dissolved oxygen concentration is at a minimum, outward. The 10% O_2 threshold satisfies the critical *Da* criterion for effective synthesis ($Da \geq 4$) developed by Dendukuri et al [37].

To confirm the validity of the simulations, we synthesized 10 μm discs in a 2 μm-tall tiered microfluidic device (Fig. 2.5) under a range of chamber oxygen concentrations. We imaged the resulting gel structures *in situ*. When $[O_2]$ was above ~10%, particle could not be made even using extended exposure durations (~1 sec), in agreement with model predictions. However, as $[O_2]$ in the purge chamber was decreased, discs formed according to the mask pattern with *increasing* height (Fig. 3.1C). A similar trend was qualitatively forecast by simulations (Fig. 3.1B). In practice, performing synthesis with chamber oxygen level below 4% is not ideal, as it leads to excessive particle sticking after ~10 min of operation.

Synthesis of thinner particles in microfluidic channels with height $H < 2$ μm will be difficult for two reasons 1) the window of opportunity for effective synthesis is small (Da scales quadratically with H but only linearly with $[O_2]_{eq}$), and 2) the pressure drop needed to drive flow scales as H^{-3} [81]. Therefore, device modifications may be required to prevent channels from bursting.

3.4.2 Brownian motion of microparticles

Achieving the colloidal (or cellular) size regime is a necessary synthesis milestone for probing the interactions of designer microparticles with biological or biomimetic environments. It is well known that one of the hallmarks of colloidal objects is they undergo spontaneous, random walk when suspended in a viscous fluid. A common statistical measure for particle dynamics in an inherently stochastic process is mean-squared displacement (MSD), $\langle \Delta R^2(\tau) \rangle$, calculated from particle trajectories:

$$\langle \Delta R^2(\tau) \rangle = \langle \big(R(t+\tau) - R(t) \big)^2 \rangle \qquad (3.6)$$

where $R(t)$ is the position of the particle at time t, and τ is the lag time between the two positions occupied by the same particle. <...> denotes a time-average. In a Newtonian fluid, such as water, the MSD of particles moving in a plane (2D) grows linearly with lag time,

$$\langle \Delta R^2(\tau) \rangle = 4 D_i \tau \qquad (3.7)$$

where D_i is the translational diffusion coefficient in bulk ($i = \infty$) or near the surface ($i = 0$).

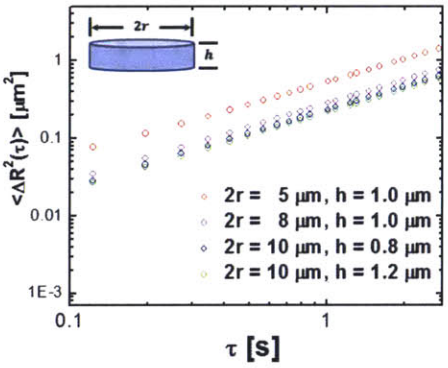

Figure 3.2 – Mean-square displacement $\langle \Delta \boldsymbol{R^2} \rangle$ in bulk as a function of lag time, τ for various colloidal discs suspended in 90% v/v D_2O. The MSD curves show a power-law slope of 1, which is consistent with Brownian motion, revealing the colloidal nature of these disc-shaped particles. For Brownian motion in 2-dimensions, $\langle \Delta \boldsymbol{R^2} \rangle = \boldsymbol{4D\tau}$, where $\boldsymbol{D}$ is the translational diffusivity. The value of $\boldsymbol{h}$ for each particle sample was calculated from Eq. (3.9) given the diffusivity measurement.

To demonstrate the colloidal nature of the microparticles generated using the modified SFL technique, we synthesized 5 μm and 8 μm diameter discs in the presence of 8.5% O_2. These synthesis experiments would not be feasible without lowering the oxygen concentration in the vicinity of the synthesis microfluidic device. Rhodamine B was covalently conjugated to the hydrogel backbone during synthesis to facilitate particle tracking. We recorded the motion of the microdiscs at least 4 particle diameters away from the rigid bottom surface of the observation

chamber. The experimental buffer solution was density-matched by adding 90% v/v deuterium oxide in order to prolong the observation period, in which the particles remain in the focal plane of the microscope objective. We did not observe any particle swelling after D_2O addition. The choice to synthesize discs rather than more complex shapes enables the use of a public-domain algorithm to first locate the particles, then extract the particle trajectories, and finally calculate the MSDs [82] (Fig. 3.2). Trajectories were constructed by linking of the brightness centroid locations of candidate particles found on at least 10 consecutive frames, until they fell out of focus. The resulting MSD curves are linear in τ, consistent with Brownian motion. The corresponding translational diffusivity coefficients in bulk (D_∞) were calculated from lines of best fit to the data using Eq. (3.7) (Table 3.2). The values of D_∞ decrease as the size of the discs increase, as one would intuitively expect.

Table 3.2 – Bulk diffusivity of the microdiscs measured using multiple particle tracking experiments. Values of $\boldsymbol{h}$ were calculated using Eq. (3.9). $\boldsymbol{r_s}$ is related to $\boldsymbol{h}$ by $\boldsymbol{r_s = \sqrt[3]{3/4r^2h}}$.

r (μm)	r_s (μm)	h (μm)	D_∞ (μm²/s)
2.5	1.67	1.0	0.105
4	2.29	1.0	0.070
5	2.47	0.8	0.059
5	2.82	1.2	0.055

We can use the bulk diffusivity measurements to estimate the height of the colloidal particles. This method is valuable because the out-of-plane dimension of non-spherical colloids is often difficult to directly quantify using conventional optical microscopy techniques. In general, bulk diffusivities are affected by particle geometry and size. In the simplest case, translational diffusion coefficient, D_S, of a sphere is related to its radius, r_S, by the Stokes-Einstein equation:

$$D_S = \frac{kT}{6\pi\eta r_S} \tag{3.8}$$

where k is the Boltzmann constant, T is the absolute temperature, η is the fluid viscosity.

For thin discoids, the bulk diffusivity, D_∞, is a function of the aspect ratio, $p = h/2r$, where h is the height, and r is the radius of the disc. Hansen [83] developed the following correlation that fits results from Monte Carlo simulations:

$$D_S/D_\infty = 1.0304 + 0.0193\ln p + 0.0623(\ln p)^2 + 0.0048(\ln p)^3 + 0.0017(\ln p)^4 \tag{3.9}$$

where D_S is the bulk diffusion coefficient of a sphere with the same volume as the disc. Similar empirical expressions for D_∞ also exist (see for example, ref. [84]); the impact of choosing one equation over another to estimate the height of the discs is minimal (± 1-3%) over the narrow regime of aspect ratio under consideration. It is readily seen that deviation from spherical symmetry reduces particle mobility. But as the particle aspect ratio $p \to 1$, $D_\infty \cong D_S$.

To estimate the height of colloidal discs using Eq. (3.8) and (3.9), we assumed the diameter of the particles to be the size of the mask pattern. This is a good assumption for two reasons: 1) the coefficient of variation for SFL is no more than a few percent[3], and 2) the high PEGDA concentration minimizes any swelling effects. High resolution confocal imaging of a 10 μm disc

supports this assumption (Fig. 3.4C). Particle height calculated from diffusivity measurements and Eq. (3.9) are shown in Table 3.2. Error introduced in h through the uncertainties in the bulk diffusivity measurement (± 0.002 μm²/s) is less than 0.1 μm in all cases (Fig. 3.3). We note that the 5 μm x 1 μm discs are the smallest particles synthesized to date using SFL.

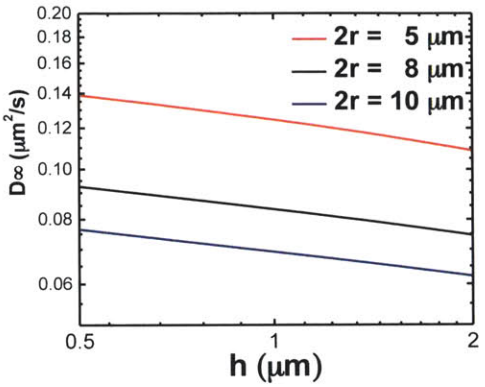

Figure 3.3 – Bulk diffusivity as a function of particle height h and radius r, calculated using Eq. (3.9).

While size and geometry of the in-plane feature is defined by the photomask, height of the particles can be tuned by adjusting the chamber oxygen concentration [48]. And more importantly, sub-micron-tall particles can be generated by lowering the chamber O_2 concentration close to the critical threshold of 10%. To show this, we synthesized 10 μm discs using 8% and 9.5% O_2, and measured their bulk diffusivities in a 90% (v/v) D_2O aqueous mixture (Fig. 3.2). We estimated the out-of-plane dimension of the particles to be 1.2 and 0.8 μm, respectively (Table 3.2).

To verify the latter result, a laser scanning confocal microscope equipped with a high numerical aperture oil immersion objective (NA = 1.3) was used to directly visualize the thinnest particle sample (10 μm x 0.8 μm discs). Confocal microscopy relies on point illumination through a pinhole to eliminate out-of-focus light in the region of interest (ROI) within the sample, resulting in increased optical resolution. Using an excitation wavelength appropriate for rhodamine B (568 nm), the in-plane resolution is ~0.25 μm. The particles were immersed in 2% alginate solution to arrest their orientation, and imaged on the bottom surface. The image stack was assembled using ImageJ to construct the 3D structure of the microgels (Fig. 3.4B). Dimensions of the particle were gauged at full width at half-maximum (FWHM) from spatially-resolved intensity profiles (Fig. 3.4). Accordingly, the particle height was estimated to be ~0.8 μm, in agreement with predictions made based on diffusivity measurements. Error introduced by Brownian motion during imaging acquisition is estimated to be ~0.1 μm.

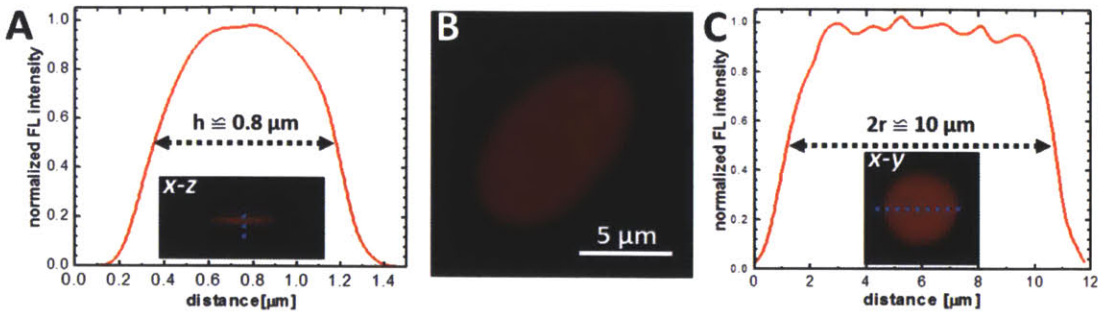

Figure 3.4 – Laser scanning confocal image of a representative 10 μm disc synthesized using 9.5% O_2 (B). Normalized fluorescence intensity profiles taken across the x-z (A, blue dotted line) and x-y (C, blue dotted line) planes of the particle. Particle height is estimated to be ~0.8 ± 0.1 μm. Full width at half-maximum (FWHM), as indicated black dotted lines, was used to define the particle boundaries.

Next, we examine the Brownian motion of discoids near a planar solid surface. Studying the transport behavior of non-spherical particles near physical boundaries has proven to be a difficult task both theoretically and experimentally. Analytical expressions from theoretical treatment of hindered diffusion are limited to the simplest particle geometries (i.e., spheres [85] and discs). Techniques which are capable of creating exotic particle morphologies (i.e., lock-key particles [86], boomerangs [87], etc.), have only recently been introduced.

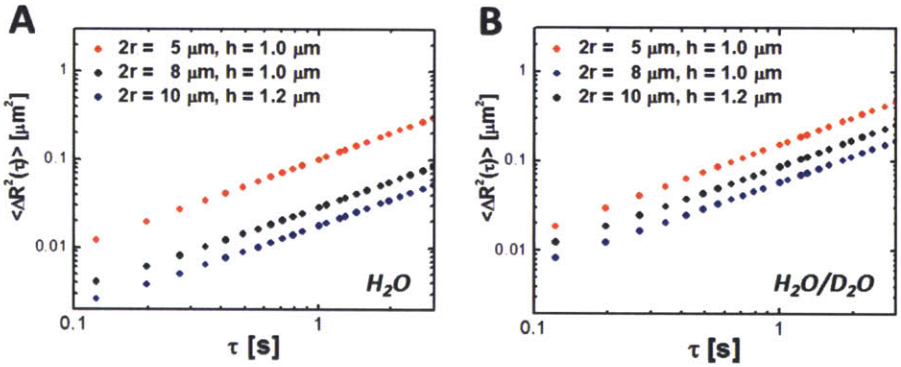

Figure 3.5 – Mean-square displacement $\langle \Delta R^2 \rangle$ near a wall as a function of lag time, τ for various colloidal discs in (A) water and (B) a mixture of deuterium oxide and water (9:1 ratio by volume).

To measure the hindered diffusion coefficients of discs experimentally, we suspended the particles in an aqueous buffer and allowed ample time for them to sediment to the bottom surface of the observation chamber prior to imaging. Up to 2500 frames were collected per movie in order to gather at least 20,000 particle trajectories in total and extract the in-plane translational diffusion coefficient, D_0. Fig. 3.5 and Table 3.3 show MSDs and hindered diffusivities, respectively, in two different buffers. Unlike their bulk counterparts (Table 3.2), mobility of microparticles is reduced by as much as ~80% owing to hydrodynamic interactions with the wall. For thin discs diffusing close to a wall, the preferred mode of motion is in the plane of the particle, parallel to the glass slide. Addition of 90% deuterium oxide by volume reduced

the density mismatch ($\Delta\rho$) between the aqueous buffer and the particles from 0.10 to 0.02 g/mL. The particle density was estimated using the weighted sum of PEG-DA and the photoinitiator densities to be 1.1 g/mL. This assumes 100% conversion, and represents the density upper bound. As a result, the average gravitational height of the particles,

$$h_g = \frac{kT}{\Delta\rho V_p g} \tag{3.10}$$

increases, as does the value of D_0 (Table 3.3). In Eq. (3.10), V_p is the particle volume, and g is the constant of gravitational acceleration (9.81 m/s^2). The elevation-dependent Brownian dynamics are clearly seen for the 8 and 10 μm discs, for which viscous drag forces opposing edgewise translation decreases most rapidly [88].

Table 3.3 – Hindered diffusivity estimates for colloidal discs from experiment and theory Eq. (3.11) in two particle storage buffers. Addition of D_2O decreases density mismatch between the buffer and the particle, causing the average gravitational height to increase.

			D_0(μm^2/s)	
r (μm)	**Buffer**	**h_g(nm)**	*Experiment*	*model*
2.5	H_2O	213.4	0.0285	0.0271
2.5	D_2O/H_2O	1067	0.0381	0.0814
4	H_2O	83.3	0.0069	0.0056
4	D_2O/H_2O	416.7	0.0210	0.0199
5	H_2O	44.5	0.0042	0.0029
5	D_2O/H_2O	266.7	0.0129	0.0093

In reality, the equilibrium separation distance between the particle and the surface continuously fluctuates as a result of thermal motion. It is difficult to isolate the dynamics of a particle sliding parallel to the glass slide from movement in the transverse direction without resorting to specialized techniques, such as total internal reflection microscopy [89]. As a result, the experimentally-determined D_0 values are in fact apparent diffusion coefficients that encompass the cumulative effect of sampling a range of gap heights on particle motion:

$$D_0 = \langle D_0 \rangle = \int_0^\infty kT f^{-1}(a) p(a)\, da \tag{3.11}$$

where $p(a)$ is the normalized probability of finding the particle at a distance a from the bottom surface, $f(a)$ is the friction coefficient of the particle in close proximity to the wall.

Kim et al. derived an analytical expression for $f(a)$, characterizing the edgewise translation of a thin circular plate parallel to an infinite plane [88]:

$$f(a) = \eta\left(\frac{\pi r}{a} + 3\ln\frac{r}{a} + 6.294\right) r \tag{3.12}$$

At equilibrium, $p(a)$ is the Boltzmann distribution, with h_g as the average lubricating gap distance, where potential and thermal energies balance:

$$p(a) \propto exp(-a/h_g) \tag{3.13}$$

Substituting Eq. (3.12) and (3.13) into Eq. (3.11), we can calculate the hindered diffusivity as long as the particle dimensions are known *a priori*. This simple model contains no adjustable parameters, and captures the essential physics. It can predict D_0 to within 25% when $h_g \ll r$ (Table 3.3). This can be attributed, at least in part, to overestimating the conversion and therefore, particle density. As the separation distance grows, however, this model breaks down, as the colloidal discs can no longer be approximated as infinitely thin (Table 3.3, 2.5 μm radius discs in D_2O/H_2O). We note that a similar approach was used to understand the Brownian fluctuations of charge-stabilized colloidal spheres located near a flat plate [90]. The close agreement between the model predictions and experimental data gave us confidence regarding the accuracy with which we estimated the particle dimensions using multiple particle tracking. This model can be used to guide the self-assembly of non-spherical particles near a solid boundary.

Figure 3.6 – A representative bright-field image showing a portion of the central vascularized region of the flow device. Red arrows indicate openings where particles can enter the microvascular network (above) from the adjacent medium channel (below).

3.4.3 Flow of hydrogel colloids through microvascular networks

The ability of SFL to generate anisotropic colloidal particles allows us to begin to probe the flow behaviour of particles in a biological environment. Past experiments revealed interesting shape [6] and elasticity [7, 91] induced passage properties, both *in vitro* and *in vivo*. A novel method for understanding particle flow characteristics involves the use of engineered, microfluidic vascular networks (μVNs). μVNs can be formed by endothelial cells (HUVECs) undergoing the process of vasculogenesis. In the presence of human lung fibroblasts, HUVECs gradually develop stable networks of interconnected, perfusable vessels after ~4 days in non-contact cell culture [68]. Phenotypic state of the network, such as the number of branches, and average diameter or length of the vessels, can be tuned by adjusting initial input parameters during cell culture (e.g., concentration of growth factors). To demonstrate the passage of fluorescent PEG-based colloids through μVNs, we flowed 10 μm x 1.2 μm discs by applying a small (~5 mmH_2O) hydrostatic driving pressure across the vascularized region on the microfluidic device. Particles entered the network via vessel openings to the adjacent medium channel (Fig. 3.6), and navigated through by exploiting the path of least fluidic resistance. A representative particle trajectory through a portion of the network is shown in Fig. 3.7. The fluorescence signal from the candidate particle was isolated from consecutive frames of experimental movies and superimposed on top of a

bright-field image showing the layout of the microvessels in the ROI. To preserve mass conservation, particles accelerated (marked by the spreading of their fluorescence signals) when they encountered contractions, and vice versa. Importantly, particles do not adhere to the vessel walls (Fig. 3.7A, right panel), showing signs of bio-inertness. To clearly show the size of a representative vessel in 3D relative to that of a particle, we fluorescently stained for actin with Alexa Fluor® 488 phalloidin after the flow experiment and imaged a residual particle lingering in the lumen. These results demonstrate the feasibility of using μVNs as a useful tool to study particle passage properties. Future experiments may offer mechanistic insight on shape or size effects on particle flow that ultimately result in distribution patterns seen in animal studies.

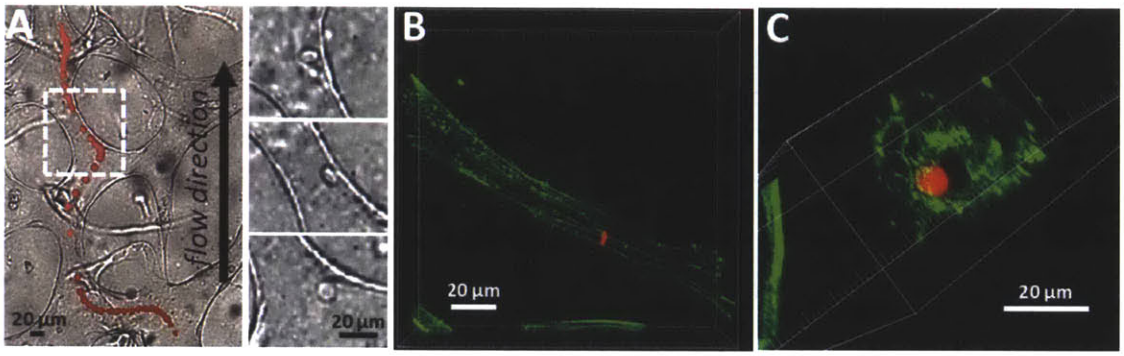

Figure 3.7 - (A) Trajectory of a colloidal disc ($\boldsymbol{d}$ = 10 μm, $\boldsymbol{h}$ = 1.2 μm) through the microvascular network grown on a multi-culture microfluidic device. The black arrow indicates the general direction flow driven by a small hydrostatic pressure difference across the network. The discs assume different orientations during their passage. The close-ups also show that they do not adhere to the microvessel walls. Confocal micrographs of the longitudinal (B) and the transverse (C) directions of a vessel segment (green) containing a residual particle (red).

3.5 Conclusions

In summary, we have shown that controlling the oxygen concentration surrounding the synthesis microfluidic device allows us to synthesize colloidal particles using flow lithography. One of the key advantages of this technique is that geometry of the particles is mask-defined, and as a result, not limited to simple polygonal shapes. Morphologically-complex colloids are critical for efficient assembly of ordered functional materials. In addition, passage of non-spherical colloids through microfluidic vascular networks deserves further attention. This platform can be used to understand the effect of particle shape and deformability on passage properties in a physiological, yet controlled setting.

CHAPTER 4

Nanoemulsion Composite Microgels for Orthogonal Encapsulation and Release

4.1 Overview

In this chapter, we present the synthesis of composite microgels containing stable hydrophobic compartments from crosslinkable silicone oil-in-water nanoemulsions. The microgels are used to demonstrate a number of motifs for controlled encapsulation and release of active compounds, including small molecules, proteins, and nanoparticles, from a single material platform.

We highlight several unique capabilities of the new composite particle platform which would be impossible to achieve with traditional polymer hydrogels. For instance, the nanoemulsion composites possess hitherto unachieved levels of loading capacity for hydrophobic compounds due to the homogeneously distributed liquid compartments with easily controllable size and concentration. Furthermore, photo-patterning of the nanoemulsions using flow lithography allows the production of microgels with controlled shape independently of the gelation or encapsulation process, which has proven important for *in vitro* delivery of microparticles [92]. Finally, the chemical interface and high surface area provided by the nanoemulsion enable new and efficient non-covalent motifs for immobilization and controlled release of both lipophilic and soluble actives. As these properties can be achieved while retaining independent control over the crosslinked polymer network in the continuous phase, our materials hold potential advantages for a number of applications, including therapeutic scaffolding materials and delivery vehicles for combination drug therapy [93, 94].

The results discussed in this chapter have been published in ref. [52] and [95].

4.2 Introduction

Polymer hydrogels and microgels have been widely exploited for the controlled storage, delivery and detection of active compounds, including small molecules and biologics [96, 97]. However, due to their intrinsically hydrated microenvironment, the development of hydrogels for encapsulation and/or release of poorly water-soluble cargos remains a persistent challenge [93]. As such, the development of novel hydrogels with well-controlled hydrophobic compartments remains important to a number of delivery applications including pharmaceuticals [93, 94], cosmetics [98], foods [99], imaging [100], and sensors [3]. Recent strategies to overcome this challenge include modification of the hydrogel polymer network by co-polymerizing or grafting hydrophobic units to create hydrophobic domains within the polymer matrix, thereby increasing solubility of poorly-soluble actives [101], or by direct conjugation of such actives to the polymer itself [102]. However, these approaches are limited by relatively low loading capacities and the need for designer polymers [93]. An alternative approach is to incorporate hydrophobic colloidal species into the hydrogel matrix, including nanoparticles [103-105], vesicles [106], micelles [107], emulsions [108] and microemulsions [109]. Although such hydrogel composites have shown some success, material systems that can simultaneously achieve high loading with tunable release for a range of poorly-soluble actives are lacking [100].

Recently, we have demonstrated the formation of nanoemulsions with controlled droplet size, loading, and stability in which nanoscale oil droplets are suspended in a hydrogel pre-cursor [95]. The immobilization of nanoemulsions within a hydrogel matrix afforded by these materials presents several advantages compared with other advanced materials for encapsulation of hydrophobic compounds. The ability to produce nanoemulsions at high volume fractions allows for precise control of loading within the hydrogel, and the ability to tune the hydrogel network allows for a controlled barrier to release [93, 110]. Compared to ordinary emulsions, nanoemulsions also exhibit increased surface-to-volume ratio, which enhances release kinetics and bioavailability, and greater kinetic stability, which improves shelf life [110]. Furthermore, the inherent control and homogeneity of droplet properties such as their size [111] distinguishes them from polymeric micellar [112] and vesicular [113] cargos, which are inherently polydisperse and can be adversely affected by a polymer matrix [114].

In this chapter, we demonstrate the synthesis of cargo-carrying composite microgel particles from crosslinkable nanoemulsions using flow lithography (FL). Flow lithography [18, 115] has been used to generate microgels with sophisticated architecture (as mentioned in the introductory chapter), including shape and chemical anisotropy [40, 116], and tunable diffusion [117] and degradation [34] profiles. As such, the potential to combine crosslinkable nanoemulsions with FL can provide particle-based delivery vehicles with homogeneous nano-scale distribution of hydrophobic compartments, while at the same time allowing their spatial localization within the hydrogel matrix, a combination which is lacking in other fluidic-based approaches [4, 118-121]. Here, we consider various novel motifs for multi-platform encapsulation and delivery of active compounds from nanoemulsion composite microparticles. In doing so, we demonstrate several orthogonal methods by which both hydrophobic and hydrophilic compounds, including small molecules, proteins and the nanoemulsion droplets themselves, can be effectively encapsulated in and released from a single microparticle.

4.3 Experimental Method

4.3.1 Materials and nanoemulsion preparation

The prepolymer mixture used in this work contain silicone oil (Dow Corning, viscosity ~5 cP) dispersed in an aqueous phase consisting of poly(ethylene glycol) diacrylate (PEG-DA, M_n = 700 g mol^{-1}) and sodium dodecyl sulfate (SDS). Additives included the photoinitiator 2-hydroxy-2-methyl-1-phenyl-propan-1-one (Darocur® 1173) and 1 mM solutions of lipophilic dyes, PKH26 ($\lambda_{ex}/\lambda_{em}$ = 551/567 nm), Nile Red ($\lambda_{ex}/\lambda_{em}$ = 550/626 nm) and 3,3'-dioctadecyloxacarbocyanine perchlorate ($DiO(C_{18})_2$, $\lambda_{ex}/\lambda_{em}$ = 484/501 nm, Invitrogen) in ethanol were used to fluorescently label the oil nanodroplets. Unless otherwise noted, all materials were obtained from Sigma Aldrich and used as supplied.

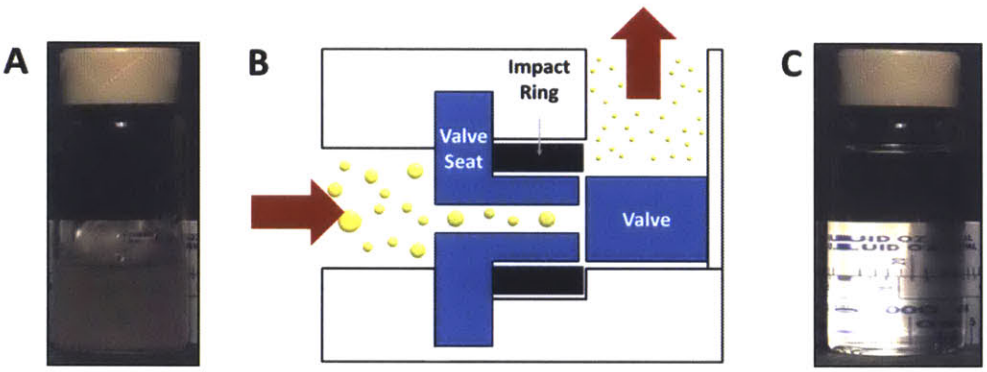

Figure 4.1 – (A) A turbid pre-emulsion (or macroemulsion). Microscale emulsions exhibit strong multiple scattering of light, hence appears opaque. As the pre-emulsion passes through the homogenizer valve (B) cyclically, droplets undergo deformation and break-up due to high elongational stress, impingement, and cavitation. (C) A optically transparent nanoemulsion after ~16 iterative passes.

To prepare the photocrosslinkable nanoemulsions, a crude pre-emulsion (Fig. 4.1A) was first generated by adding silicone oil drop-wise to a pre-mixed aqueous continuous phase containing 33% (v/v) PEGDA and 100 mM SDS under constant agitation using a magnetic stirrer. The corresponding nanoemulsion (Fig. 4.1C) was then created by high pressure homogenization (EmulsiFlex C3, Avestin) at 15 kpsi for 16 passes, with cooling in between passes to 4 °C. Standard operating procedures for the EmulsiFlex C3 can be found in *Appendix A8*. Dynamic light scattering measurements (BI200-SM, Brookhaven Instruments) indicate the as-prepared nanoemulsion had an average droplet diameter, $\langle D \rangle$, of 45 nm (Fig. 4.2). 2% (v/v) Darocur® 1173 (I = 0.02) and 5-10 μM lipophilic dyes (as necessary) were added to aliquots of nanoemulsion, followed by vortex mixing. The resulting fluid was passed through a 25 mm Acrodisc® syringe filter (0.45 μm Supor® Memberane, Pall Corporation) to eliminate any coalesced droplets, and finally stored at 4°C until further use.

4.3.2 Particle synthesis

All of the particles shown in this chapter were prepared using stop-flow lithography in multi-inlet (up to six inlet ports) rectangular microfluidic channels (PDMS, Sylgard 184, Dow Corning). Briefly, the pre-cursor mixture was injected into a synthesis device using modified pipette tips (Molecular BioProducts) as delivery chambers under moderate forcing pressure (~3 psi). Composite microparticles were patterned by projecting mask-defined UV light from a Lumen 200 metal arc lamp (Prior Scientific) through a wide excitation UV filter set (11000v2 UV, Chroma Technology). A shutter system (VS25, Uniblitz) interfaced with a custom-written Python automation script precisely controls the duration of UV exposure, which typically ranged from 150 to 800 ms depending on particle shape and size. The formation of the microparticles was visualized using a cooled interline charge-coupled device camera (Clara, Andor).

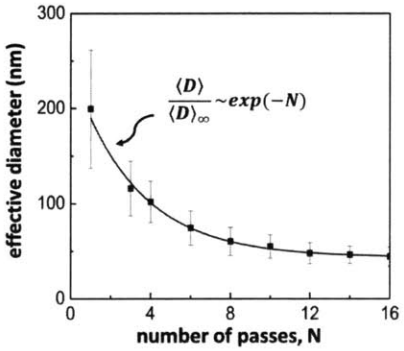

Figure 4.2 – Evolution of average droplet diameter <*D*> with increasing number of passes, ***N***, through the high pressure homogenizer for a silicone oil nanoemulsions containing droplet volume fraction φ = 0.33, volume fraction of PEG-DA in the continuous phase P = 0.33, concentration of surfactant (SDS) C_S = 100 mM at a homogenization pressure of 15 kpsi. Line gives fit to the empirical relationship proposed by Meleson *et al.* [111].

Following polymerization, particles were transferred from the outlet reservoir of the synthesis microfluidic device to a clean 1.5 mL Eppendorf tube containing 300 µL PBST (1X phosphate buffered saline with 0.5% (v/v) Tween® 20 (Sigma Aldrich). Particles were washed and re-suspended at least four times via centrifugal separation followed by decanting and replacement of the supernatant, and subsequent storage at room temperature for imaging.

4.3.3 Particle characterization

Droplets of samples containing up to 100 fluorescently labeled particles were transferred onto a glass slide and visualized by bright-field and fluorescence optical microscopy using long-pass filter sets (XF101-2 for PKH26, Cy3 and Nile Red, XF100-2 for DiO(C_{18})$_2$, Omega Optical). High resolution fluorescent images of the particles were captured with a digital SLR camera (D200, Nikon) and processed using ImageJ (NIH) software to obtain size and fluorescence intensity data. For all measurements, images of at least 10 particles were taken in order to obtain sufficient statistical information. Care was taken to standardize the experimental conditions (e.g., camera exposure time, lamp intensity setting, microscope objective, etc.) used in imaging studies. Prior to each imaging session, the lamp intensity was calibrated with a power meter (Model 1815-C, Newport).

4.3.4 *Encapsulation and release studies*

4.3.4.1 Solubilization of small molecules

For solubility-based assays, square-shaped particles were synthesized from a prepolymer (ϕ = 0.33, P = 0.33, C_s = 100 mM, I = 0.02) containing 5 μM PKH26 dye and purified into 1x PBST buffer. Fluorescence imaging and subsequent photoluminescence analysis was then used to monitor the particle fluorescence over time for a period of several weeks. Particles were stored and imaged at 23°C. Particles depleted of PKH26 (after ~5 weeks of sustained release) were incubated with dye overnight at 35°C and 1500 rpm (H5000-HC, Biomega). To achieve dye reloading, the particle concentration in the remaining suspension was first approximated via bright-field imaging, and then used to gauge the quantity of PKH26 necessary, relative to the initial basal level present during synthesis. The particles were then washed in PBST buffer containing the estimated PKH26 concentration. After incubation, the particles were washed four times in neat PBST buffer and imaged under the same conditions as those used throughout the protracted study of dye release.

4.3.4.2 Hydrophobic anchoring of soluble proteins

For protein conjugate encapsulation and release studies, we used a generic fluorescent streptavidin-biotin (SA-BT) reporter complex [122] as a model biomolecular cargo, which was immobilized at the oil/water interface via hydrophobic interactions. An acrylate-modified biotinylated peptide (Ac-BT) was obtained from Integrated DNA Technologies, and a 0.5 mM stock was prepared in TET (1X Tris-EDTA (TE) with 0.5% (v/v) Tween® 20) buffer. A fluorescent cyanine-conjugated streptavidin reporter (SA-Cy3) was obtained from Sigma Aldrich, and a 1 mM stock was prepared in 1x TET buffer.

For encapsulation and release by *weak* hydrophobic anchoring, tablet-shaped particles were synthesized from an unlabeled nanoemulsion prepolymer (ϕ = 0.20) and stored in TET buffer. Aliquots of the particle suspension were then transferred into a 5.0 μM Ac-BT solution in TET at a concentration of ~1 particle/μL and incubated overnight on a shaker plate (Biomega H5000-HC) at 45°C and 1500 rpm. The elevated temperature during incubation drives the partitioning of the weakly hydrophobic acrylate pendant groups to the oil-water interface [95]. The particles were then rinsed with neat TET at 45°C to remove excess Ac-BT in the supernatant, and subsequently centrifuged and re-suspended in 3.5 μM SA-Cy3 to initiate formation of Ac-BT-SA-Cy3 complexes. The suspension was then placed on a shaker plate again at 45°C and 1500 rpm for 4 hours, and then washed with neat TET buffer at 45°C to remove excess SA-Cy3. Aliquots of the resulting suspension were then dispensed on microscope slides and imaged using a temperature-controlled microscope stage (TSA02i, Instec Inc.). Particles were first imaged at 45°C to confirm encapsulation of Ac-BT-SA-Cy3 by hydrophobic anchoring using photoluminescence analysis. Subsequently, the temperature was quickly decreased to 15°C, and images were taken over time to observe changes in particle fluorescence.

To demonstrate *strong* hydrophobic anchoring, we obtained a short modified DNA oligonucleotide, 3'-Cholesteryl-TEG-AAAAA-PC-Biotin-5' (Chol-PC-BT, where PC represents a photo-cleavable spacer) from Integrated DNA Technologies (Coralville, IA, USA). The highly hydrophobic nature of the cholesterol group (Chol) allows biotin (BT) to irreversibly adsorb at the oil-water interface at elevated temperatures. We incubated tablet-shaped particles (~1

particle/μL 100x TE buffer) with 2.5 μM Chol-PC-BT overnight on a shaker plate at 45°C and 1500 rpm. Once loaded with Chol-PC-BT, the particles were washed four times with 100x TE buffer at 45 °C and incubated with 3.5 μM streptavidin-Cy3 (SA-Cy3) fluorescent reporter at 45°C and 1500 rpm for 4 hours. The photo-cleavable spacer (PC) is inserted between the cholesterol and biotin, to allow trigger release of the BT-SA-Cy3 complex upon UV irradiation. High resolution micrographs of the particles were taken at specific time points before and after 30 seconds of UV exposure.

Aside from hydrophobic anchoring at the interface, we note that soluble proteins can also be attached to the hydrogel backbone by covalent conjugation. To demonstrate, we diluted an Ac-BT stock solution (0.5 mM) 1:20 using TET buffer and added an unlabeled nanoemulsion prepolymer until the final biotin concentration was 2.5 μM. A 50 μL sample of tablet-shaped particles (~1 particle/μL) was incubated with 3.5 μM Streptavidin-Cy3 (SA-Cy3, Sigma Aldrich) for 4 hours at room temperature and 1500 rpm. After incubation, particles were washed four times with TET and imaged using a digital SLR camera.

4.3.5 Particle degradation studies

To demonstrate release of the fluorescently-labeled nanoemulsions via saponification and subsequent PEG-DA hydrogel degradation, triangle-shaped particles were synthesized using a prepolymer containing 10 μM Nile Red dye (ϕ = 0.33, P = 0.33, C_s = 100 mM, I = 0.02). The particles were rinsed and imaged in PBST buffer. Subsequently, particles were separated by centrifugation and re-suspended in 0.1 M NaOH in PBST buffer. The particles were then imaged over time in both bright-field and fluorescence modes.

4.4 Results

4.4.1 Uniformity of nanoemulsion loading

To synthesize nanoemulsion composite microgels, we used nanoemulsions containing low molecular weight silicone oil droplets stabilized by the surfactant sodium dodecyl sulfate (SDS), dispersed in an aqueous prepolymer containing poly(ethylene glycol) diacrylate (PEG-DA) monomer and photoinitiator (Darocur® 1173). The photopolymerization of the nanoemulsion prepolymer results in the formation of a chemically crosslinked hydrogel in the continuous phase. The crosslinkable nanoemulsions are produced by high-pressure homogenization [123], and can be readily prepared across a range of droplet sizes and continuous phase compositions [95]. Once formed, the nano-scale nature of the resulting emulsion droplets ($D < 100$ nm) provides the optical transparency essential for UV-induced photo-patterning via stop-flow lithography (Fig. 4.3A), whereas larger droplets inhibit FL due to light scattering [95].

To demonstrate successful encapsulation of the nanoemulsion within the microgels, we fluorescently labeled the entrapped oil droplets using a lipophilic carbocyanine dye, PKH26, which exhibits strong partitioning to the droplet interface. We employed an encoding strategy based on particle shape to denote key compositional differences among the particles used: disc-shaped particles initially contained nanoemulsions without PKH26, square-shaped particles contained PKH26 without nanoemulsion, and Z-shaped particles contained neither

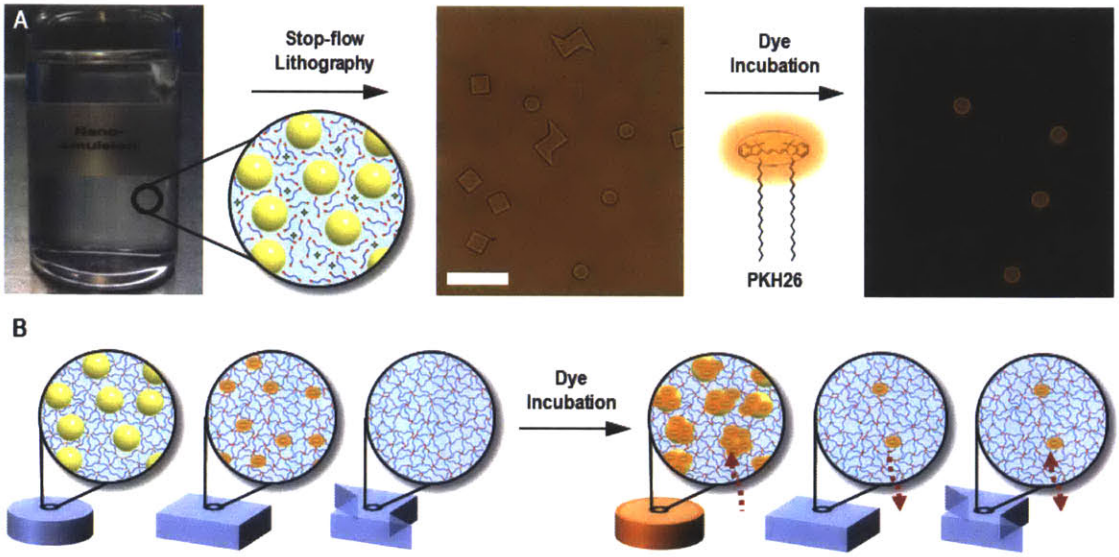

Figure 4.3 – Schematic of nanoemulsion encapsulation. (A) High pressure homogenization is used to produce optically transparent, photo-crosslinkable nanoemulsions (left). Stop-flow lithography allows the nanoemulsion to be photo-patterned into microgel particles with controlled size and shape (center). Incubation of microgel particles with a hydrophobic dye (PKH26) demonstrates successful encapsulation of the nanoemulsion (right). (B) Schematic depiction of the particles shown in the micrographs in A). As synthesized, the disc-shaped, square-shaped, and Z-shaped particles contain nanoemulsion without dye, dye without nanoemulsion, and neither dye nor nanoemulsion, respectively. Upon incubation with dye, dye is preferentially absorbed by the particles containing nanoemulsion, whereas it is not retained by particles without nanoemulsion. Arrows indicate the net flux of dye during incubation. Scale bar is 50 μm.

nanoemulsion nor PKH26. Upon PKH26 incubation, only disc-shaped particles remained fluorescent, demonstrating that PKH26 is preferentially loaded into the nanoemulsion droplets that are encapsulated within the hydrogel matrix (Fig. 4.3).

The demonstrated ability to confine nanoemulsions within a microgel can potentially be used to encapsulate hydrophobic active compounds. To test this hypothesis, we employ PKH26 as a model lipophilic active, where its fluorescence provides a convenient route for quantification of loading uniformity, the lack of which may reduce encapsulation efficiency and control over desired release characteristics. Here, PKH26 (5 μM) is incorporated directly into the prepolymer, without any additional dye incubation. Fig. 4.4A (left) shows a typical collection of monodisperse disc-shaped particles synthesized using SFL. Photoluminescence analysis indicates highly uniform fluorescence both across different particles (Fig. 4.4A, right) and within any given particle, where the fluorescence is uniform to sub-micron length scales (< 400 nm) corresponding to the resolution of the 40x microscope objective (Fig. 4.4C). To our knowledge, this high degree of homogenous and reproducible loading of the nanoemulsion, and consequently the active, outperforms commonly used particle synthesis techniques based on droplet microfluidics [120].

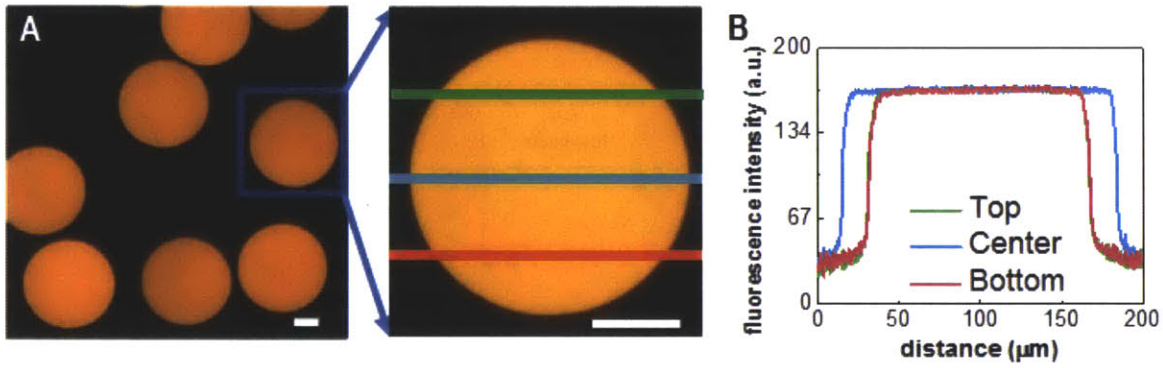

Figure 4.4 – (A) Fluorescent micrograph of monodisperse disc-shaped particles pre-loaded with PKH26. (B) Spatially resolved fluorescence intensity profiles (a.u. = arbitrary units) taken across three different lanes of the particle shown in (A, right). Scale bars are 50 μm.

To quantify polydispersity in loading within a population of composite particles, we measured the average in-plane fluorescence intensity of different particles ($n > 100$) using fluorescence microscopy. The coefficient of variation (COV) in fluorescence was calculated as the standard deviation divided by the corresponding mean. The COV, irrespective of particle geometry, varied from 4%-7% in fluorescence, and 1.7%-3.5% in size. The fluorescence intensity and size distribution results for the disc-shaped particles presented in Fig. 4.4 are shown below (Fig. 4.5).

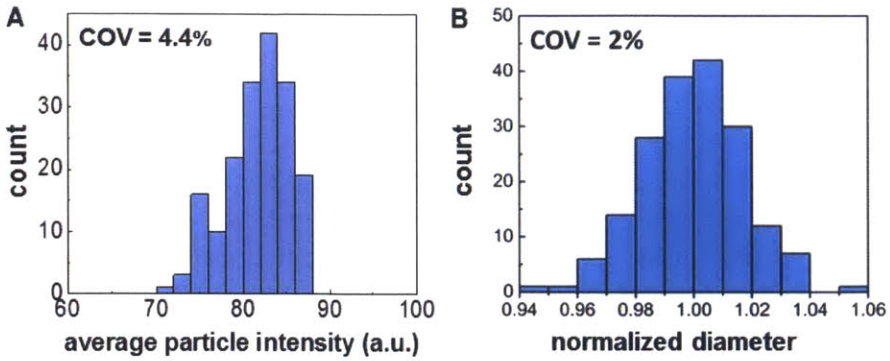

Figure 4.5 – Statistical distribution of (A) average fluorescence intensity and (B) normalized diameter of the disc particles ($\boldsymbol{n}$ = 181, diameter, $\boldsymbol{d}$ = 187 ± 4 μm) shown in Fig. 4.4.

4.4.2 Synthesis phase space

Interestingly, the nanoemulsion prepolymers undergo an abrupt thermo-reversible transition from a low viscosity Newtonian fluid to a solid-like viscoelastic gel caused by the temperature-induced inter-droplet bridging of PEG-DA [95]. The temperature at which this gelation process occurs is affected by many experimental parameters, including droplet diameter, silicone oil volume fraction, PEGDA volume fraction in the continuous phase and Darocur® 1173 concentration. In particular, the gel temperature decreases significantly as the value of any of the aforementioned compositional variables increases. To optimize particle feature resolution, droplet loading and ease of photo-patterning via SFL, one canonical recipe was chosen (ϕ = 0.20, P = 0.33, C_s = 100 mM, I = 0.02), although higher oil volume fraction, up to ϕ = 0.33, could also be used to fabricate composite microgel particles.

To demonstrate this, a fluorescently labeled nanoemulsion prepolymer sample was made (ϕ = 0.33, P = 0.33, C_s = 100 mM, C_{PKH26} = 5 μM) and then serially diluted with pure continuous phase (without any SDS) to achieve a range of oil volume fractions from ϕ = 0.05-0.25. The photoinitiator concentration was fixed at 2% v/v in all samples. Since the ratio of oil to dye is fixed in each dilute sample, a decrease in particle fluorescence intensity can purely be attributed to a reduction in nanoemulsion loading (Fig. 4.6).

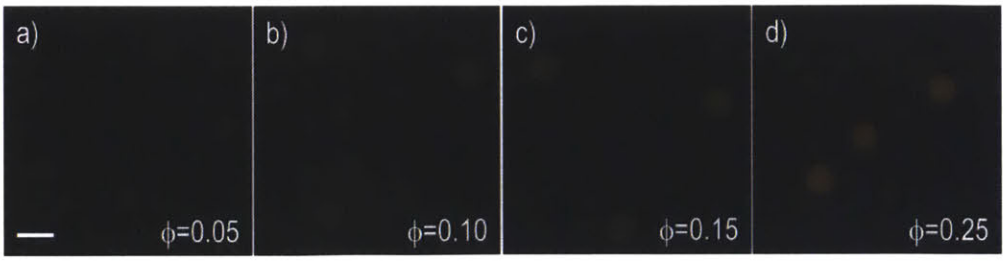

Figure 4.6 – Optical micrographs of disc-shaped particles ($\boldsymbol{d}$ = 40 ± 1 μm) containing varying volume fractions (ϕ) of fluorescently-labeled nanoemulsions: (A) ϕ = 0.05; (B) ϕ = 0.10; (C) ϕ = 0.15; (D) ϕ = 0.25. Scale bar is 50 μm.

4.4.3 Shape and chemical anisotropies

The delivery of microparticle-based vehicles *in vivo* has been shown to depend strongly on particle shape [56]. As such, the ability of SFL to generate morphologically complex particles in a high-throughput fashion yields distinct advantages over other fluidic methods [120, 124], which are limited to production of spheroidal particles. To show that we can pattern nanoemulsion composite microgels with arbitrary, micro-scale 2D-extruded shapes, we have synthesized various polygonal solids such as Z-shaped (Fig. 4.7B), square (Fig. 4.7C) and triangle (Fig. 4.7D) particles with characteristic sizes ranging from 30 μm – 180 μm. All of the particles show fidelity to the original mask shape and are uniform with respect to size and fluorescence intensity. These results show that the silicone oil nanoemulsions are compatible with a number of variants of SFL, and could be used to synthesize more sophisticated particle morphologies [116] and internal structures [125].

In addition to particles with shape anisotropy, SFL can generate microgels with sophisticated chemical anisotropy [18, 115]. In the context of our nanoemulsion microgel composites, this allows for the creation of particles with multiple compartments with different composition and properties. To do so, we synthesized Janus microgels by patterning tablet-shaped particles across the interface of two photopolymerizable co-flowing streams, one with and one without PKH26-labeled nanoemulsion, resulting in particles with a distinct compartment to which the nanoemulsion is confined (Fig. 4.7E, left). The sharp interface between the two halves of the particle persists for several days (Fig. 4.7E, right), indicating negligible mobility of the encapsulated nanoemulsion droplets within the hydrogel matrix.

Such compartmentalization of the nanoemulsion can be used as a facile method to generate multifunctional particles with spatially segregated chemistries containing different, potentially chemically incompatible, active compounds. To illustrate this, we synthesized dumbbell-shaped particles using five nanoemulsion-laden prepolymer streams, each labelled with red fluorescent PKH26 or green fluorescent $DiO(C_{18})_2$ dyes in an alternating fashion (Fig. 4.7F, left). The resulting particles demonstrate spatial segregation of actives on the same particle, with minimal interpenetration between neighboring domains (Fig. 4.7F, right). By adjusting the flow rate of prepolymer streams, we can easily shift location of the interfaces and make particles that contain variable proportions of different chemistries. By extension, more morphologically and chemically complex designer composite microgels could easily be created by flowing or stacking more concurrent laminar streams containing functional and functionalizable materials [34, 35, 40].

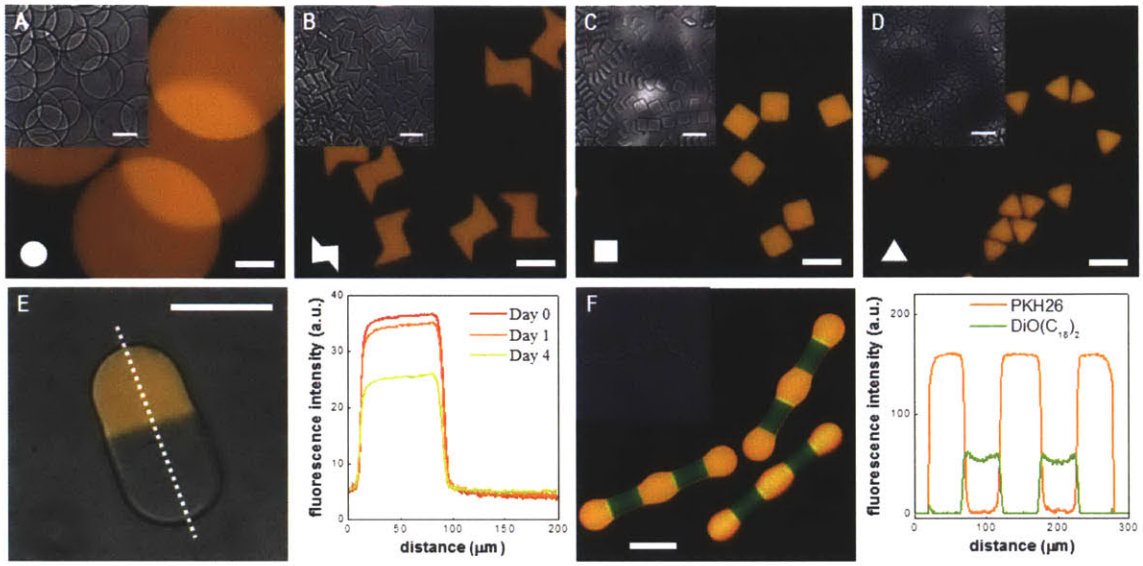

Figure 4.7 – Geometrically and chemically complex nanoemulsion-laden particles synthesized using SFL. All particles are made using a 20x microscope objective. As synthesized, the disc-shaped (A), Z-shaped (B), square-shaped (C), and triangle-shaped (D) particles have characteristic feature sizes of 180, 70, 50, and 30 μm, respectively. (A)-(D) each shows fluorescent and bright-field (upper left inset) micrographs of a particle array and the corresponding transparency mask feature (lower left inset) used during synthesis. (E) Overlaid fluorescent and DIC images of Janus particles, highlighting both nanoemulsion-laden (orange) and control (gray) sections (left). Time evolution of fluorescence intensity scans (right) along the long axis (dashed white line) of tablet-shaped Janus particles show in (E, left). The enduring sharpness of the Janus interface suggests minimal migration of the nanoscopic compartments over time. (F) Overlaid fluorescent micrographs demonstrating the co-encapsulation of two different hydrophobic dyes in five distinct regions of dumbbell-shaped particles (left). Spatially resolved intensity profiles of the orange (PKH26) and green ($DiO(C_{18})_2$) fluorescence in the multi-compartment particles shown in (F, left) demonstrate minimal interpenetration between neighboring compartments. Scale bars are 50 μm.

4.4.4 Encapsulation and release of active compounds

Having established the capabilities for producing nanoemulsion-laden microgels by SFL, we sought to prove their utility for controlled encapsulation and release of both hydrophobic and hydrophilic active compounds via a number of different motifs that take advantage of the homogeneous, nano-scale distribution of droplets within the particle. Specifically, we now show how encapsulation can be achieved either through solubility within the oil phase, through molecular anchoring at the oil-water (O-W) interface, or through the release of the nanoemulsion droplets themselves in concert with these motifs.

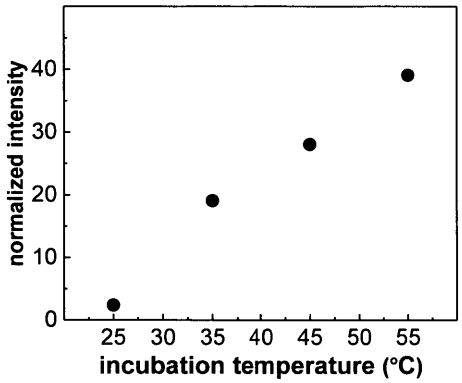

Figure 4.8 – PKH26 loading with increasing temperature during incubation.

The simplest method for encapsulation of hydrophobic species is solubility within the nanoemulsion. As shown previously using the lipophilic dyes PKH26 and DiO(C_{18})$_2$, loading of the microgels can be performed either before synthesis by introducing of the active into the prepolymer stream (Fig. 4.4) or after synthesis by partitioning of the active from an aqueous phase into the nanoemulsion (Fig. 4.3). The former method enables localization of the active to various compartments within the particle (Fig. 4.7F). However, the latter enables differential loading of the same particles. To demonstrate this, microgel discs containing ϕ = 0.20 nanoemulsion droplets without dye were incubated in PBST containing 5 μM PKH26 at different temperatures ranging from 25-55°C . The amount of PKH26 loaded into the particles varies significantly with incubation temperature, as shown by a ten-fold increase in fluorescence intensity of the dye-laden microgels with increasing temperature (Fig. 4.8). This is driven by the temperature dependence of the thermodynamic partitioning of the dye between the aqueous and oil phases.

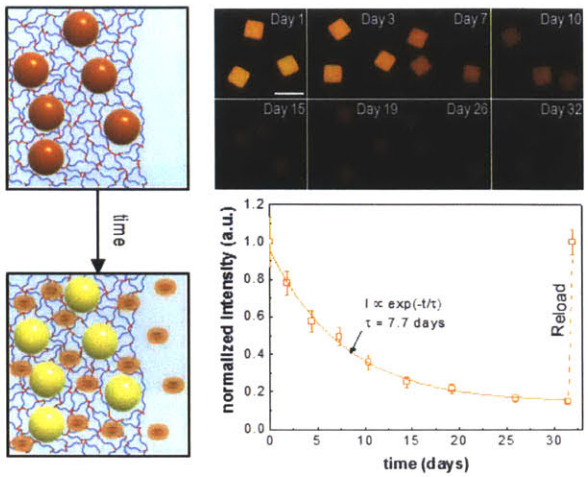

Figure 4.9 – Encapsulation of PKH26 within the nanoemulsion and subsequent sustained release due to limited solubility in the solution phase (left: schematic molecular workflow diagrams). Micrographs show elution of the active into dye-free buffer over a period of several weeks, with first-order release kinetics. The depleted particles can be stoichiometrically reloaded with dye (dotted orange line).

Release of actives from ordinary nanoemulsions into an aqueous phase typically occurs as a "burst" due to the high surface-to-volume ratio of the droplets [99]. By contrast, the release of hydrophobic species from nanoemulsion droplets encapsulated within microgel particles will be controlled by both the departure of the active from the O-W interface and subsequent diffusion through the crosslinked hydrogel into the supernatant phase [93]. This is demonstrated in Fig. 4.9, where the release of PKH26 from particles initially containing 5 μM PKH26 loaded at 25°C was monitored by quantifying the average particle fluorescence intensity over time. As shown, the release of PKH26 is sustained over a period of multiple weeks. Furthermore, the normalized fluorescence intensity decays as $I/I_0 \sim \exp(-t/\tau)$, where τ = 7.6 days is the characteristic time scale for release, suggesting that release of hydrophobic actives from the nanoemulsion can be described by simple first-order mass transfer kinetics. After a period of several weeks, the particles were re-incubated with an amount of PKH26 corresponding to the initial concentration within the particles, after which the observed particle fluorescence was identical to that initially measured for the as-prepared particles. Thus, the nanoemulsion remains stably encapsulated within the microgel for long periods of time, enabling sustained release as well as reloading on demand. In particular, we note the lengthy time for release compared to that for reloading suggests that the release process is primarily limited by desorption of the active compound from the O-W interface. In concert with the Janus motifs shown previously, these principles could be used to design composite microgel particles with sophisticated release profiles, whereby the barrier to release can be varied in a controlled fashion by tuning the materials (oil, surfactant, etc.) comprising the nanoemulsion.

In order to extend demonstrations for controlled encapsulation and release using our composite microgels to soluble biologics, we used a generic scheme for the attachment of biomolecules based on previous work [122], in which a biotinylated (BT) linker is incorporated into the composite microgels, and a streptavidin functionalized with cyanine dye (SA-Cy3) was used as a reporter and model soluble protein to be encapsulated. Because of the structure of the hydrogel-nanoemulsion composite scaffold, attachment of biotin moieties to the particle can be achieved

through a number of mechanisms, which identify several potential motifs for encapsulation and release of bioactives.

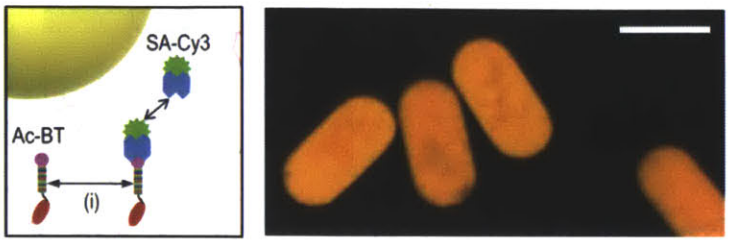

Figure 4.10 – Encapsulation of biomolecules by covalent conjugation to the hydrogel matrix. Ac-BT is incorporated into the PEG-DA hydrogel during particle synthesis, allowing for (i) controlled encapsulation of SA-Cy3 upon incubation (left). Micrograph shows particles becoming fluorescent after incubation with SA-Cy3, indicating the successful incorporation of Ac-BT and SA-Cy3 into the composite microgels. Scale bar is 50 μm.

One motif involves covalent attachment of an acrylate-functionalized biotinylated nucleotide (Ac-BT) to the crosslinked hydrogel network via photopolymerization, which can then bind SA-Cy3 during post-processing (Fig. 4.10). Though this scheme has been previously demonstrated for encapsulation and sensing of bioactives in microgels [122], we found that such a motif is not compromised by the presence of encapsulated nanoemulsions. Subsequent release of the SA-bound active (represented here by Cy3) could be achieved through hydrolytic degradation of the polymer network and resulting cleavage of the BT-SA-Cy3 complex [34].

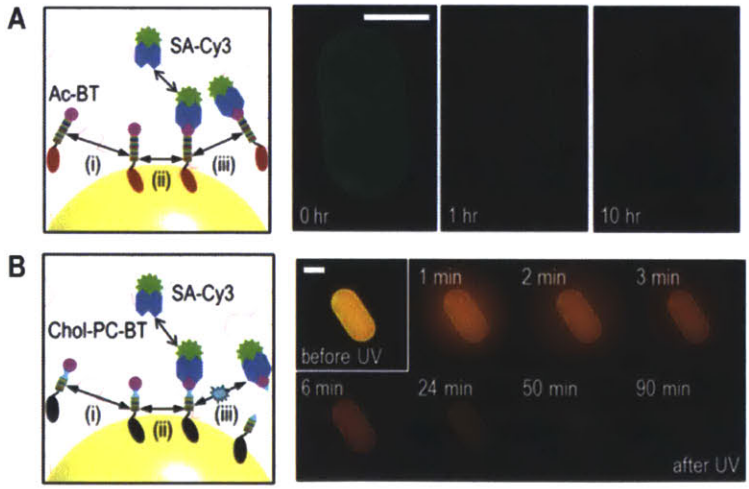

Figure 4.11 – (A) Encapsulation and release by reversible hydrophobic anchoring to the O-W interface. (i) Particles are incubated at 45°C with Ac-BT, which partition to the O-W interface, and (ii) monitored by SA-Cy3 reporter. (iii) A decrease in temperature to 15°C results in release of the Ac-BT-SA-Cy3 complex from the O-W interface. Micrographs show subsequent release of the reporter over several hours (color-enhanced to show detail). (B) Demonstration of irreversible hydrophobic anchoring and photo-triggered release of a model biomolecular complex from hydrogel-nanoemulsion composite microparticles: (i) particles are incubated with Chol-PC-BT, leading to encapsulation at the O-W interface. (ii) Particles are incubated with SA-Cy3 reporter, resulting in BT-SA-Cy3 complexation. (iii) UV exposure results in photolysis of Chol-PC-BT and subsequent rapid release of BT-SA-Cy3. Micrographs show a representative particle before and after 30 seconds of UV exposure at the times indicated. Scale bars are 50 μm.

Another possible scheme for controlled encapsulation and release of bioactives involves their functionalization with hydrophobes, enabling encapsulation within composite microgels by anchoring at the surface of nanoemulsion droplets. Depending on the hydrophobicity of the anchoring group, different strategies can be employed to release the attached biomolecular cargo.

To demonstrate weak (or reversible) hydrophobic anchoring, we utilize our previous observation that acrylic moieties exhibit temperature-induced partitioning at the O-W interface [95]. "Empty" tablet-shaped microgels containing nanoemulsion were incubated with 5 μM Ac-BT at 45°C to induce anchoring of the acrylic groups to the nanoemulsion droplets. The supernatant was then exchanged for buffer containing 3.5 μM SA-Cy3 reporter, and after washing, the particles exhibited significant fluorescence relative to control particles without nanoemulsion (Fig. 4.11A). Upon cooling the microgel suspension to 15°C, particles exhibited a significant decrease in fluorescence over a period of hours, indicating desorption of acrylic groups from the O-W interface and subsequent release of the Ac-BT-SA-Cy3 complex.

This encapsulation and delivery scheme is highly flexible, as the hydrophobe could be modified to achieve adsorption behavior ranging from reversible anchoring to semi-permanent, whereas the hydrogel microstructure (e.g., the crosslink density) can be independently controlled to modify the release kinetics. In particular, strong hydrophobic anchoring can result if we replace the acrylate linker with a cholesterol linker. To show this, we incubated tablet-shaped particles post-synthesis with a cholesterol-modified biotin (Chol-PC-BT) as a model bioactive, resulting in adsorption of the bioactive to the O-W interface. Hydrophobic anchoring was confirmed through an additional incubation with a streptavidin-Cy3 fluorescent reporter (SA-Cy3), which selectively binds to Chol-PC-BT, resulting in fluorescently labeled particles (Fig. 4.11B).

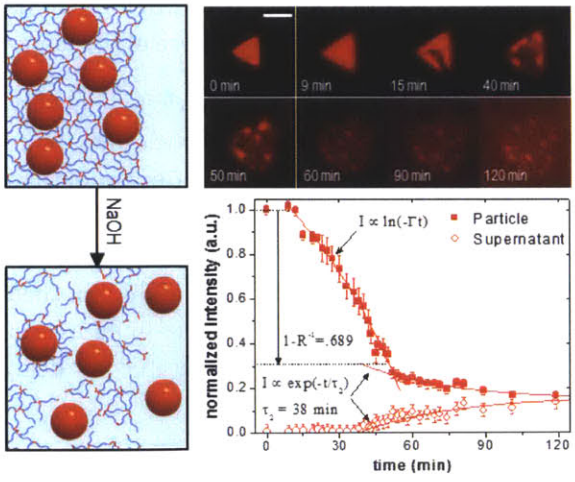

Figure 4.12 – Release of nanoemulsion droplets by degradation of the hydrogel matrix. Saponification at high pH first results in swelling of the particle at short times, followed by degradation of the particle and release of the nanoemulsion over a period of hours.

Once encapsulated, release of the BT-SA-Cy3 complex was achieved through UV photolysis of the photocleavable linker (PC), resulting in an initial burst-like release over a period of seconds followed by sustained release over a period of hours. Importantly, we note that because photolysis of the PC linker occurs at wavelengths comparable to those used in SFL, direct incorporation of PC-BT into hydrogels through photopolymerization would be infeasible.

Finally, we demonstrate a highly orthogonal motif of delivery by release of the nanoemulsion droplets themselves from the composite microgel particles, thereby liberating them as nanoparticle vehicles for further transport and delivery of lipophilic and hydrophobic actives. For our PEG-DA hydrogels, we achieve this through saponification and subsequent physical degradation of the hydrogel matrix by incubating the particles under basic pH conditions (Fig. 4.12). Triangle-shaped particles were synthesized using a nanoemulsion containing 10 μM of the hydrophobic dye Nile Red, resulting in composite microgels with initially uniform loading. The particles were purified into PBST buffer (pH = 7.0) and transferred into PBST with 0.1 M NaOH (pH = 12.4). The particles were then imaged over time at 23 °C, and photoluminescence analysis was performed to monitor both the particle and supernatant fluorescence during saponification (Fig. 4.12).

Upon transfer into high pH buffer, we observe two qualitatively different kinetic regimes in photoluminescence analysis of the particles. Initially, the particles swell appreciably over a period of 60 minutes. At short times (< 10 min), this swelling is uniform and isotropic, whereas at long times, defects appear to manifest in the fluorescence micrographs as dark-colored fractures in the particle surface. Over this time, we observe a significant decrease in particle fluorescence that is logarithmic in time such that $I/I_0 \sim \ln(-\Gamma t)$, where Γ is a characteristic rate of swelling that presumably depends on the kinetics of saponification. We note that the decrease in fluorescence intensity over this period is entirely accounted for by the volumetric swelling of the particle, characterized by a swelling ratio $R = 3.21$, such that $(1 - R^{-1}) = 0.689$ coincides with the loss of particle fluorescence over this period. Throughout this time, the supernatant solution exhibits no observable fluorescence. As such, we conclude that the initial decrease in intensity is due entirely to swelling of the particle, and not from release of the nanoemulsion droplets.

At long times (> 40 min), a qualitatively different behaviour is observed in which the particle exhibits no appreciable additional swelling, and the particle fluorescence decreases over time. By contrast to short times, however, the fluorescence of the supernatant phase increases at a rate similar to the decrease in particle fluorescence. We find that both the decrease in particle fluorescence and increase in supernatant fluorescence can be described by a single exponential where $I/I_0 \sim \exp(-t/\tau)$, with a single characteristic time of 38 min that quantitatively describes both processes. As such, we find that the observed changes in fluorescence at long times are due primarily to the release of nanoemulsion droplets liberated by degradation of the hydrogel matrix.

These results suggest the following mechanism of release of the nanoemulsion droplets during degradation of the PEG-DA matrix (Fig. 4.12). Saponification involves the cleavage of ethylene glycol units within the crosslinked PEGDA network, which decreases the crosslink density of the hydrogel matrix over time. Initially, this decrease is significant enough to give rise to significant swelling of the particle [126], but still mild enough that the droplets remain sterically trapped within the polymer network. However, after a critical time (~40 min for the results shown here), the hydrogel network is ultimately degraded to a point where the mesh size of the hydrogel increases beyond the size of the droplets, at which point they can freely diffuse throughout the

particle and into the supernatant. Assuming that pH regulation and saponification within the particle are not diffusion-limited, this critical time is homogeneous throughout the particle, and release of the nanoemulsion droplets thus follows a simple first-order kinetic model corresponding to diffusion of the droplets from the particle interior into a semi-infinite supernatant medium.

4.6 Conclusions

In summary, we have shown that crosslinkable nanoemulsions present a versatile new material platform for the production of designer hydrogels with hydrophobic compartments of controlled size and loading. Their combination with flow lithography enables the design of microgels with sophisticated shape and chemical anisotropies, as well as tunable microstructure. These properties have allowed us to develop a suite of capabilities (solubilization, covalent conjugation, hydrophobic anchoring, and matrix degradation) for the encapsulation and release of model compounds from a single particle, including both hydrophobic and hydrophilic species representing a broad class of actives ranging from small molecules to biologics. In particular, hydrophobic anchoring of actives presents an encapsulation method that is highly orthogonal to traditional routes of hydrogel encapsulation, and matrix degradation allows for the further use of the nanoemulsion droplets as deployable nanocarriers to potentially couple with targeted delivery strategies [127-129]. Furthermore, the measured release kinetics cover time scales ranging from an hour to several weeks depending on the release mechanism, thereby providing a highly flexible system for engineering materials for different applications from the same material platform. Future studies using these materials involving extension of actives used to more relevant therapeutics and nutrients, as well as rational control of the particle microstructure to tune release kinetics, will test their suitability in a wide range of applications including pharmaceuticals, multi-drug therapies, consumer products, and foods.

CHAPTER 5

Oxygen-carrying Compartmentalized Microparticles

5.1 Overview

In this chapter, we turn our attention to the synthesis of red blood cell-like, oxygen-carrying composite microparticles using crosslinkable perfluorocarbon oil (PFC)-in-water nanoemulsions. PFCs are the active component of many current emulsion-based artificial blood products (also known as oxygen therapeutics [130]). Unlike the silicone oil nanoemulsions we studied in the previous chapter, kinetic stability of the perfluorocarbon counterparts is low due to elevated solubility of the oil in the aqueous continuous phase. As a result, we focus on formulation development at first, with the goal of optimizing the shelf life of the nanoemulsion prepolymers. Then, for particle synthesis, we perform experiments under reduced oxygen atmosphere to counteract the deleterious effect of enhanced O_2 transport.

Here, we use oxygen-controlled SFL to lithographically photo-pattern compartmentalized microparticles with any 2D-extruded shape, down to the cellular length scale (~10 microns). The prepolymer solution consists of a UV crosslinkable perfluorodecalin-in-water nanoemulsion stabilized by Pluronic F-68. The nanoemulsions are generated using high pressure homogenization and stabilized by the trapped species method [131, 132]. The presence of PFC droplets increases the solubility and diffusivity of oxygen in the prepolymer solution, thereby enhancing the rate of O_2 inhibition during microparticle synthesis. We develop a simple model that successfully predicts the augmented O_2 mass transport, which agrees well with experimental data.

The results discussed in this chapter have been published in ref. [48].

5.2 Introduction

As mentioned in the introductory chapter, bio-inspired polymeric particles are promising vehicles for drug delivery and clinical diagnostics [1, 133, 134]. These particles are synthetic constructs engineered in the likeness of natural particulates, such as pathogens and mammalian cells, and can mimic one or more key functions or attributes of their biological counterparts. A variety of top-down and bottom-up synthesis methods have been used, including self-assembly [135], droplet microfluidics [16], photolithography [24, 25], non-wetting template molding [14], liquefaction and stretching [136], and electrohydrodynamic jetting [137], to manipulate the size, shape [138], mechanical stiffness [6] and internal structure of these biomimetic microcarriers. The ability to precisely vary the particle physical properties is especially desirable as it allows these particles to maneuver through biological barriers, avoid cellular capture [139], and even prolong circulation time [91] or alter biodistribution patterns *in vivo*. Therefore, versatile fabrication techniques that can provide independent control over critical particle design parameters are essential for modulating the interaction of these novel biomaterials with biological entities in biological environment [92].

Currently, a facile technique for patterning morphologically complex, compartmentalized microparticles down to the cellular length scale ($\sim$10 microns) is still largely missing. Compartmentalization is one of the universal architectural motifs seen abundantly in eukaryotic cells, and allows a multitude of biochemical reactions to occur in perfect synchronicity in order to perform certain desired macroscopic cellular functions. Traditional methods of generating compartments in polymeric particles often suffer from 1) a lack of geometric complexity (due to surface tension forces, for example [140]) or 2) lower feature resolution [52, 141]. The potential utility of multi-compartmental microparticles have already been demonstrated in several experiments: they can be used to efficiently co-encapsulate incompatible actives (e.g., drugs, imaging modalities, etc.) [52, 142], program delivery profiles and engineer different environmental release triggers (pH, temperature, light exposure, ultrasound, and external fields, etc.) [52, 143-146].

Here, we show the reproducible synthesis of oxygen-carrying microparticles from crosslinkable oil-in-water nanoemulsions via a modified stop-flow lithography (SFL) technique (Chapter 2). The dispersed phase consists predominantly of perfluorodecalin (PFD), the principal component in the first generation of perfluorocarbon (PFC)-based artificial blood products [130]. In general, PFCs are a class of biologically and chemically inert, highly hydrophobic, synthetic organic compounds. The inherent strength of the constituent C-F bonds, and therefore weak intermolecular forces, allow PFCs to efficiently solubilize respiratory gases (i.e., O_2, CO_2). For example, the equilibrium partition coefficient, K, for O_2 between perfluorodecalin and water is $\sim$ O(10) [147]. As such, PFCs are often used in artificial blood and cell culture [148] applications to enhance the rate of O_2 mass transfer.

Unlike our previous work involving silicone oil-based nanoemulsions, the PFD-based formulations are biocompatible but require further stabilization due to a finite solubility of oil in the aqueous continuous phase [144]. The PFC-laden composite microgels are structurally and functionally reminiscent of erythrocytes, which are long-circulating biological entities

responsible for oxygen delivery *in vivo*. Fabrication of these PFC solutions is challenging as they facilitate oxygen transport, which in turn inhibits free radical polymerization, and impedes bulk gelation. To generate these biomimetic, oxygen-carrying composite microparticles, we take a rational engineering approach to first slow the coarsening of the PFC nanoemulsion through variation in composition, and then lower the effective concentration of oxygen, a common radical scavenger during synthesis, using a purge chamber filled with an inert gas. This synthesis technique allows cell-sized, shape-anisotropic microparticles to be patterned in a semi-continuous fashion. One of the key advantages of this process is that the properties of the carrier particle and those of the encapsulated compartments can be optimized separately for a diverse set of biomedical applications.

5.3 Experimental Method

5.3.1 Materials and nanoemulsion preparation

The crosslinkable oil-in-water nanoemulsions used in these experiments contain perfluorinated oils: perfluorodecalin and perfluorotripropylamine (Oakwood Chemicals, Inc.) dispersed in an aqueous phase consisting of poly(ethylene glycol) diacrylate (PEG-DA, M_n = 700 g/mol) and non-ionic surfactant Pluronic F-68 (PF68). Additives included the photoinitiator 2-hydroxy-2-methyl-1-phenyl-propan-1-one (Darocur® 1173) and the lipophilic dye, PKH26 ($\lambda_{ex}/\lambda_{em}$ = 551/567 nm, Invitrogen) in ethanol. The latter was used to label the encapsulated oil nanodroplets for fluorescent imaging. Unless otherwise noted, all materials were obtained from Sigma Aldrich and used as supplied.

To prepare the nanoemulsions, a crude pre-emulsion was first generated by adding the perfluorinated oil(s) drop-wise to an aqueous continuous phase containing 36% (v/v) PEG-DA and 2-40 mM PF68 under constant agitation using a magnetic stirrer. The corresponding nanoemulsion was then created by high pressure homogenization (EmulsiFlex-C3, Avestin) at 5-20 kpsi for up to 20 passes. Prior to composite particle synthesis, 4% (v/v) Darocur® 1173 and 10 μM PKH26 (if necessary for imaging purposes) were added to aliquots of the nanoemulsion, followed by vortex mixing.

5.3.2 Particle synthesis

All of the particles shown in this chapter were prepared using a modified stop-flow lithography (SFL) technique in rectangular microfluidic channels (PDMS, Sylgard 184, Dow Corning). Channel heights ranged from 20 to 50 μm. The synthesis devices were placed inside a custom-made sealed chamber with an inert gas purge inlet. Briefly, the prepolymer mixture (degassed for 60 minutes under gentle argon flow, unless otherwise specified) was injected into a synthesis device using modified pipette tips (Molecular BioProducts) as delivery chambers under moderate forcing pressure (~3 psi). Cell-like composite microparticles were patterned by projecting mask-defined UV light from a Lumen 200 metal arc lamp (Prior Scientific) through a wide excitation UV filter set (11000v2 UV, Chroma Technology). A shutter system (VS25, Uniblitz) interfaced with a custom-written Python automation script precisely controlled the duration of UV exposure, which typically ranged from 150 to 800 ms depending on particle

shape and size. Microparticle formation was visualized using a cooled interline charge-coupled device camera (Clara, Andor).

Following polymerization, particles were transferred from the outlet reservoir of the microfluidic synthesis device to a clean 1.5 mL Eppendorf tube containing 600 µL PBST (1X phosphate buffered saline with 0.1% (v/v) Tween® 20). Particles were washed and re-suspended four times in PBST then stored at room temperature for imaging.

5.3.3 Nanoemulsion characterization

Nanoemulsion droplet sizes were measured via dynamic light scattering (DLS) using a Brookhaven Instruments BI-200SM multi-angle apparatus. Samples were diluted to $\varphi = 0.0005$ using a mixture of 33% PEG-DA700 in deionized water. Autocorrelation functions were measured at a scattering angle of 90° and 25°C. A Cumulant analysis was conducted on the data acquired to obtain the hydrodynamic droplet diameter $2R$. Coefficient of variation (COV) is defined here as the variance of the size distribution relative to the mean size.

5.3.4 Microparticle characterization

PKH26-labeled composite microparticles were harvested from the synthesis devices and stored in PBST buffer prior to imaging using a laser confocal scanning microscope (Zeiss LSM Meta 510) equipped with an argon laser (543 nm). Successive *x-y* scans were acquired at intervals of 0.1 µm in the z-direction through representative particles using a 100X oil objective. The images were analyzed using ImageJ (NIH).

Perfluorodecalin/water surface tension measurements were taken using the pendant droplet method on a DSA 10 tensiometer (Kruss). A calibration curve was prepared by measuring surface tension for a set of Pluronic F-68 standard solutions at room temperature.

5.4 Results

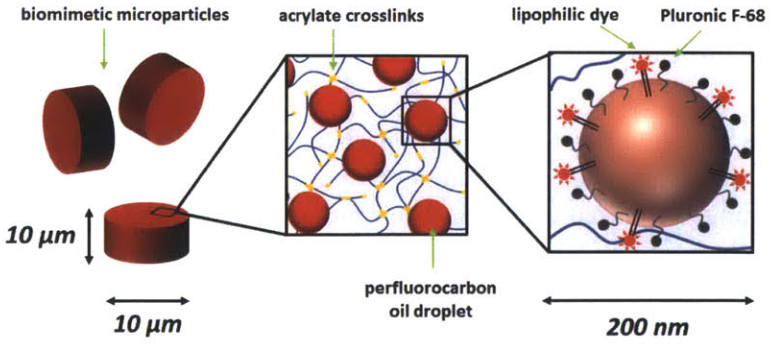

Figure 5.1 – Schematic depiction of biomimetic composite microparticles. Stop-flow lithography reproducibly generates these microparticles from UV-crosslinkable perfluorocarbon oil-in-water nanoemulsions. The nanometer-sized oil droplets contain a mixture of perfluorodecalin and perfluorotripropylamine, stabilized by a biocompatible nonionic surfactant, Pluronic F-68. The droplets are kinetically arrested within the gel network, as indicated by lipophilic dye labeling, and can facilitate oxygen transport, similar to red blood cells.

To synthesize RBC-like microparticles (Fig. 5.1), we use an oil-in-water (O/W) nanoemulsion composed of perfluorodecalin oil (MW = 462 g/mol) stabilized by Pluronic F-68, dispersed in an aqueous continuous phase containing 36% poly(ethylene glycol) diacrylate (PEG-DA, M_n = 700 g/mol) and 4% Darocur®1173. PEGDA and Darocur act as the crosslinker and photoinitiator, respectively. During UV exposure, Darocur undergoes photolysis and initiates polymerization of the acrylate end-groups on the PEG-DA molecules. This results in the formation of a crosslinked hydrogel network that kinetically traps the perfluorocarbon oil droplets.

5.4.1 Nanoemulsion formulation and stability

The crosslinkable O/W nanoemulsions are generated via a two-step emulsification process. In the first step, a pre-mix macroemulsion is generated using a magnetic stirring device, fixing the emulsion composition. Next, the pre-mix is transferred to a high pressure homogenizer and forced through an adjustable homogenizing valve at elevated pressures ($\leq$ 20 kpsi), during which droplets experience the elongational stress needed to overcome the significant Laplace pressure difference and to rupture down to the nanometer size scale [149]. It is worth noting that in the emulsion literature, there lacks a universally accepted cut-off below which a colloidal dispersion would be considered a nanoemulsion. Here, we define a nanoemulsion as a metastable suspension consisting of two incompatible phases, with the dispersed phase having diameter below 200 nm [149].

To assess the stability of the PFC nanoemulsions over time, we prepared an 8% (v/v) perfluorodecalin-in-water nanoemulsion containing 40 mM Pluronic F-68, and 36% PEG-DA700 (φ = 0.08, C_S = 42 mM, P = 0.36). The nanoemulsion is homogenized at 20 kpsi for 10 passes. The as-prepared sample has an initial droplet diameter of ~167 nm. A time course of the droplet volume growth at 4°C was tracked via DLS and shown in Fig. 5.2A. As expected, due to their nanoscopic size and non-zero polydispersity (defined here as the variance in droplet size over the mean), the droplets mainly coarsen via the Ostwald ripening mechanism, according to $\langle R\rangle^3 \sim \omega t$. Ostwald ripening is a process driven by molecular diffusion, whereby larger droplets grow at the expense of smaller ones in order to minimize the total interfacial area [132]. ω is the ripening rate, and can be analytically expressed as [131]:

$$\omega = \frac{8v^2 D_{oil} C_\infty \gamma}{9RT} \qquad (5.1)$$

where v, D_{oil}, and C_∞ are the molar volume, diffusion coefficient, and bulk solubility of oil through the continuous phase, respectively. γ is the surface tension, R is the universal gas constant, and T is the absolute temperature. The measured ripening rate (~600 nm^3/min) is much higher than that of the silicone oil formulations (~0.1 nm^3/min) we had previously studied, due to a finite solubility of perfluorodecalin in the aqueous continuous phase [144, 150].

To improve the stability of nanoemulsion prepolymer and to lengthen its shelf life for particle synthesis, we added minor amounts ($\leq$ 3% by volume) of perfluorotripropylamine (PFTPA) into an 8% perfluorodecalin nanoemulsion. PFTPA is an insoluble oil species with a moderate *in vivo* retention time of ~60 days, short in comparison to other commercially-available perfluorinated compounds with similar molecular weights (521 g/mol) [130]. PFTPA preferentially partitions to the oil droplet interior and exerts an osmotic pressure that counterbalances the forces that

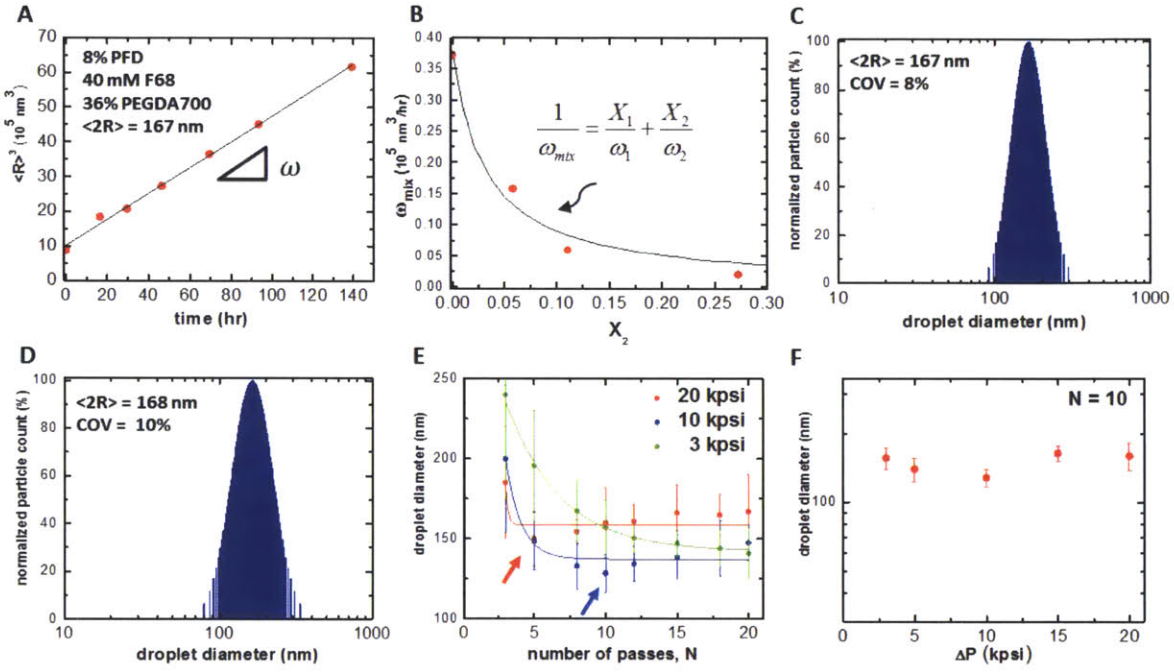

Figure 5.2 – Nanoemulsion formation and stability. (A) Time evolution of average droplet volume for an 8% v/v perfluorodecalin (PFD)-in-water nanoemulsion containing 36% poly(ethylene glycol) diacrylate (M_n=700 g/mol) and stabilized by 40 mM PF68. The initial droplet is 167 nm. The linear trend observed suggests that the dominant coarsening mechanism is Ostwald ripening, with characteristic rate ω. (B) Variation of ω with the addition of a high molecular weight 'trapped species' perfluorotripropylamine (PFTPA), which can counteract Ostwald ripening by creating an entropic barrier for de-mixing. The solid line shows theoretical prediction using Eq. (5.2). Normalized droplet size distributions were measured using dynamic light scattering for 8% perfluorodecalin-in-water nanoemulsions (P=0.36, C_s=40 mM) containing (C) 0% v/v PFTPA and (D) 0.5% v/v PFTPA. The nanoemulsion samples were prepared using high pressure homogenization at 20 kpsi for 10 passes. Addition of the oil stabilizer has minimal impact on the initial droplet diameter and monodispersity (upper left corner). (E) The evolution of average droplet diameter with the number of passes, N, through the homogenization device for an 8% PFD-in-water nanoemulsion (φ_2=0.005, P=0.36 PEGDA, C_s=40 mM) at three different pressures. Lines give fit to the exponential relationship suggested by Mason *et. al* [ref. [111]]. (F) The evolution of average droplet diameter with homogenization pressure for N=10.

cause Ostwald ripening [151]. Initial repartitioning of the mobile oil component between droplets due to Ostwald ripening creates an entropic barrier that retards further oil de-mixing.

As shown in Fig. 5.2B, ω decreases asymptotically with PFTPA addition. The overall growth trend is well predicted by the following mixing law [152]:

$$\omega_{mix} = \left(\frac{X_1}{\omega_1} + \frac{X_2}{\omega_2}\right)^{-1} \tag{5.2}$$

where X_1 and X_2 are the oil-based volume fractions of PFD and PFTPA, respectively. The ripening rate for a pure PFTPA nanoemulsion, ω_2, is approximated using previously reported values of aqueous bulk solubility (Table 5.1) according to:

$$\omega_2 \approx \omega_1 \frac{C_{\infty,2}}{C_{\infty,1}} \tag{5.3}$$

Table 5.1 – Summary of reported aqueous bulk solubilities of PFD (component 1) and PFTPA (component 2) and estimated ripening rates of the corresponding crosslinkable PFC-in-water nanoemulsions.

Parameter	Value	Units	Source
$C_{\infty,1}$	99	10^{-10} M	Ref. 29
$C_{\infty,2}$	2.8	10^{-10} M	Ref. 29
ω_1	37.2	10^3 nm^3/hr	Measured
ω_2	1.1	10^3 nm^3/hr	Calculated

Addition of the 'trapped species' has little effect on droplet size or coefficient of variation, as indicated by the similar droplet size distributions measured for two batches of 8% PFD-in-water nanoemulsions with 0% PFTPA (Fig. 5.2C) and 0.5% PFTPA by volume (Fig. 5.2D) prepared at 20 kpsi (N = 10).

To further demonstrate the instability of PFC nanoemulsions, we note the evolution in droplet size as a function of the number of passes, N, for a range of homogenization pressures (3-20 kpsi). Typically, we use the number of passes through the homogenizing device to tune the droplet polydispersity [144]. This is because the flow field near the homogenizing valve is highly nonhomogeneous and turbulent. Passing an emulsion sample through the device repeatedly allows droplets to experience similar strain histories, and lowers droplet polydispersity. Similarly, over time, the average droplet size tends to exponentially approach a final saturation value[111] (Fig. 4.2). In the case of PFC nanoemulsions, however, the droplet size trajectory passes through a minimum when pressures ≥10 kpsi (Fig. 5.2E, red and blue arrows) and then slightly increases with N. Within this pressure regime, the $\langle 2R \rangle$ vs. N trends are poorly described by the exponential relationship proposed by Mason and coworkers [111]. This suggests that the droplets may be undergoing re-coalescence during homogenization as it is difficult for off-the-shelf surfactants, such as Pluronic F-68, to effectively stabilize newly created O-W interfaces during droplet collisions. The re-coalescence behavior is further evidenced by the weak power-law dependence of droplet size on homogenization pressure ($D \propto \Delta P^{0.03}$, Fig. 5.2F).

5.4.2 PFC-laden composite particle synthesis

To synthesize cell-like microparticles, we use the canonical prepolymer formulation containing 8% PFD, 0.5% PFTPA (by volume) dispersed in an aqueous continuous phase of 36% PEG-DA700, 20 mM Pluronic F-68 and 4% photoinitiator (Darocur® 1173). Adjusting the surfactant concentration from 2 to 40 mM does not improve emulsion stability against ripening (**Fig. 5.3A**). Within this surfactant concentration regime, which is orders of magnitudes greater than the surfactant's critical micelle concentration (~0.04 mM as determined using the pendant drop method in 1X PBS buffer at room temperature, **Fig. 5.3B**), changes in surface tension, γ, is small, therefore it is not surprising the ripening rate doesn't vary dramatically (Eq. 5.1). The oil volume fraction can be arbitrarily lowered without causing droplet coalescence by diluting a concentrated emulsion stock with pure continuous phase containing the same concentration of PF68.

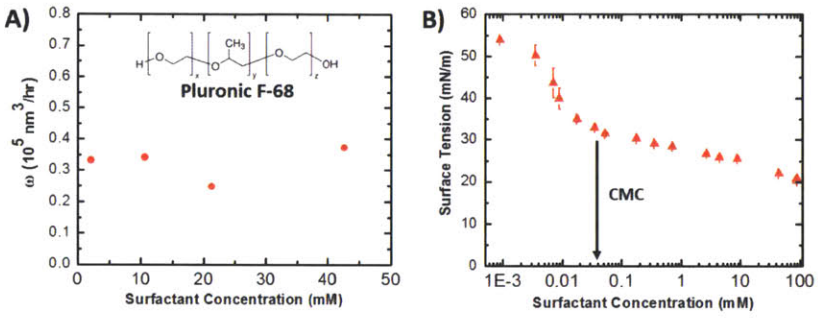

Figure 5.3 – Variations of (A) Ostwald ripening rate, ω and (B) perfluorodecalin/water surface tension with Pluronic F-68 concentration. PF68 is a common non-ionic triblock copolymer surfactant (structure shown in inset).

The high oxygen content of PFC-laden prepolymer solution is counterproductive towards particle photo-patterning via stop-flow lithography (SFL) [25, 37]. In traditional SFL, pulses of mask-defined UV light are projected through a microscope objective to generate free-standing gel structures within a microfluidic device, down to the micron-scale (Fig. 5.4, left). The ability to generate free-standing microparticles of potentially any 2D-extruded shape is intimately tied to oxygen transport; during particle synthesis, oxygen, a radical scavenger, rapidly diffuses through the porous walls of the polydimethylsiloxane (PDMS) device and inhibits the UV-initiated polymerization by reacting with propagating oligomers, forming chain-terminating peroxide species (Fig. 5.4, right) [37]. Typically, the level of O_2 must be reduced by at least three orders of magnitude before bulk gelation can occur [37]. Where the rate of oxygen diffusion balances that of oxygen inhibition near the channel periphery, lubricating layers of unpolymerized material, termed the inhibition layer, form above and below the crosslinked particles, and allow them to be advected downstream for collection. As the inhibition layer thickness (δ) approaches the channel height, as it does in the case of generating cell-sized composites, particle synthesis becomes proportionally more difficult. Using a one-dimensional reaction-diffusion model for photopolymerization within a PDMS microfluidic device, Dendukuri et al. [37] previously derived analytical scaling relationships for δ and τ (the time required to deplete the oxygen present and trigger crosslinking) and showed that both are inversely related to a Damköhler number, Da, which denotes the competition between the rate of oxygen inhibition to the rate of oxygen diffusion into the prepolymer:

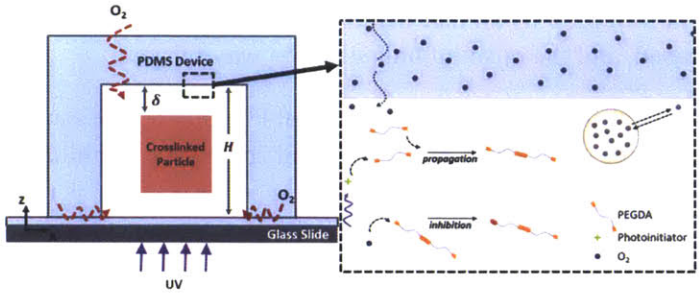

Figure 5.4 – Schematic of the cross-sectional view of a PDMS synthesis device showing the formation of a disc-shaped composite particle using stop-flow lithography. The particle is flanked on either side by films with thickness $\boldsymbol{\delta}$ of unpolymerized oligomers (left). O_2 rapidly diffuses through the PDMS side walls and partitions into the perfluorocarbon oil droplets (right). During polymerization, O_2 consumption in the continuous phase via inhibition reactions with propagating PEG oligomers leads to further O_2 release from the oil droplets.

$$Da = \frac{\psi \varepsilon I_0 [PI] H^2}{D[O_2]} \tag{5.4}$$

where ψ is the quantum yield of formation of the initiating radicals, $[PI]$ and ε are the photoinitiator concentration and molar extinction coefficient, respectively, I_0 is the incident intensity of UV light, H is the channel height, D is the oxygen diffusivity, and $[O_2]$ is the oxygen concentration in the prepolymer (for simplicity, the subscript "*eqb*" has been omitted). The use of PFCs in the prepolymer lowers the achievable feature resolution under similar exposure conditions, as compared to a pure PEGDA-based prepolymer, by increasing both the diffusivity and solubility of O_2.

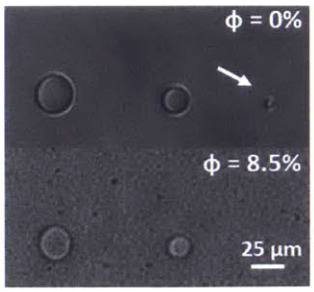

Figure 5.5 – Micrographs of a series of discs with decreasing feature size polymerized in a 15 μm tall device using prepolymers composed of 0% PFC (P=0.36, I=0.04) and 8.5% PFC ($\boldsymbol{\varphi_1}$=0.08, $\boldsymbol{\varphi_2}$=0.005, C_s=20 mM). The composite microparticles are consistently under-polymerized due to an increased effective O_2 concentration in the presence of PFC nanodroplets.

To demonstrate this qualitatively, we polymerized a series of discs of varying diameters ranging from 15 to 25 μm in a 20 μm tall PDMS device. Two types of prepolymers were used, only one of which contained the nominal 8.5% perfluorocarbon oil, the other containing none. Using the

same exposure duration (800 ms) and intensity, all of the disks formed in the nanoemulsion prepolymer stream were under-polymerized (**Fig. 5.5**); whereas the two largest discs fully polymerized in the PFC-free prepolymer. This was because PFC nanodroplets acted as point sources of oxygen and released O_2 almost instantaneously during UV exposure. As a result, the induction time increased, and the onset of bulk gelation was delayed.

To quantitatively evaluate the effect of the presence of PFC on the efficacy of particle patterning, we look at the channel cross-section (z-direction), and compare the inhibition layer thickness in the presence and absence of PFCs in the prepolymer solution [37]. It has been previously shown that $\delta \sim Da^{-1/2}$. Therefore, using similar polymerization conditions, the ratio of the two δ's - with and without PFCs - simplifies to:

$$\frac{\delta}{\delta_0} = \sqrt{\frac{D[O_2]}{D_0[O_2]_0}} \tag{5.5}$$

Here, the 'zero' subscript indicates the continuous phase (i.e., in the absence of PFCs). The ratio of the equilibrium oxygen concentrations can be estimated based on a simple volume average:

$$[O_2] = (1-\varphi)[O_2]_0 + \varphi[O_2]_{PFC} \tag{5.6}$$

Eq. (5.6) can be re-written by eliminating $[O_2]_{PFC}$ using the partition coefficient, $K = [O_2]_{PFC}/[O_2]_0$:

$$\frac{[O_2]}{[O_2]_0} = 1 + (K-1)\varphi \tag{5.7}$$

Substituting K = 16, a 8.5% by volume PFC nanoemulsion, the RHS of Eq. 5.7 equals ~2.2,[147] indicating a higher overall concentration of oxygen, though only oxygen present in the continuous phase can participate in the inhibition reaction.

Next, we derive a mean-field analytical expression for the effective oxygen diffusion coefficient, D, in the presence of PFC droplets. Here, for simplicity, we treat the emulsion prepolymer as a homogenous material, with D as the characteristic oxygen diffusivity that must be used to describe the mass transfer occurring on a length scale much greater than the average spacing between droplets. D is found by considering the far-field perturbation in the oxygen concentration field caused by the PFC oil droplets. A similar mean-field approach was taken by Deen to derive the effective conductivity of a particle suspension [153].

We model the nanoemulsion as a dilute suspension of spherical particles with a uniform number density of n, occupying a spherical volume of radius a sufficiently large to contain many particles. Far from this volume, the total oxygen concentration perturbation at r due to the oil droplet is:

$$C_p^{total}(r) = \frac{4\pi}{3}a^3 n C_p(r) \tag{5.8}$$

C_p represents the single-particle contribution derived from solving for the oxygen concentration field in a simple system consisting of a spherical particle (e.g., a PFC droplet) of radius R surrounded by a different material (e.g., the aqueous continuous phase). The droplet and the continuous phase have different oxygen diffusion coefficients, D_{PFC} and D_0, respectively. A constant mass flux, G, parallel to the z-axis (Fig. 5.4) is assumed far from the sphere due to an

imposed oxygen concentration gradient resulting from particle polymerization. The steady-state oxygen concentration outside the droplet, $\psi(r, \eta)$, is governed by mass conservation:

$$\frac{\partial}{\partial r}\left(r^2 \frac{\partial \psi}{\partial r}\right) + \frac{\partial}{\partial \eta}\left((1-\eta^2)\frac{\partial \psi}{\partial \eta}\right) = 0 \tag{5.9}$$

$$\frac{\partial \psi}{\partial z}(\infty, \eta) = G \tag{5.10}$$

Similarly, the concentration within the droplet, $\Lambda(r, \eta)$ is given by:

$$\frac{\partial}{\partial r}\left(r^2 \frac{\partial \Lambda}{\partial r}\right) + \frac{\partial}{\partial \eta}\left((1-\eta^2)\frac{\partial \Lambda}{\partial \eta}\right) = 0 \tag{5.11}$$

with a finite concentration at the center of the droplet. The two governing equations are coupled by the matching concentration and flux boundary conditions at the oil/water-PEG-DA interface.

$$\Lambda(R, \eta) = K\psi(R, \eta) \tag{5.12}$$

$$D_{\mathrm{PFC}} \frac{\partial}{\partial r}\Lambda(R, \eta) = D_0 \frac{\partial}{\partial r}\psi(R, \eta) \tag{5.13}$$

This system of coupled PDEs can be solved using Legendre polynomials and the finite Fourier transform method. The full solution appears in *Appendix C*. The O_2 concentration field outside the droplet is:

$$\psi(r, \eta) = A + Gr\eta + \left(\frac{1-\beta}{2+\beta}\right)\frac{R^3}{r^3} Gr\eta \tag{5.14}$$

with $\beta = D_{PFC}/D_0$ and A an arbitrary constant, undetermined due to the Neumann boundary condition imposed at $r = \infty$. From the final solution for the concentration field, it is seen that the effect of the droplet on the continuous phase oxygen concentration decays as r^{-2}. Equating the last term on the RHS of Eq. 5.14 to C_p, and inserting it into Eq. (5.8):

$$C_p^{total}(r) = \varphi a^3 \left(\frac{1-\beta}{2+\beta}\right)\left(\frac{G\eta}{r^2}\right) \tag{5.15}$$

where φ is the droplet volume fraction.

Finally, the effective diffusivity of oxygen in the nanoemulsion is found by comparing Eq. (5.15) with the case of a homogenous material characterized by diffusivity parameter, $\beta' = D/D_0$, occupying the same volume, i.e., setting $R = a$ in Eq. (5.14) and writing a second equivalent expression for C_p^{total} and solving for D:

$$D = D_0\left(1 + 3\left(\frac{\beta-1}{\beta+2}\right)\varphi + O(\varphi^2)\right) \tag{5.16}$$

This is analogous to the result derived for the conductivity of a particle suspension [153, 154]. If we neglect any particle-particle interactions (e.g., in the dilute regime), it is seen that the first correction to the diffusion coefficient is proportional to the oil volume fraction. Substituting representative values for D_{PFC} ($1.88\text{x}10^{-8}$ m^2/s) [155] and D_0 ($2.84\text{x}10^{-11}$ m^2/s) [37] into Eq. (5.16) for a 8.5% emulsion, D/D_0 is approximately equal to 1.3. Evaluating Eq. (5.5) using Eq. (5.7) and (5.16) gives theoretical predictions for δ/δ_0 for various oil volume fractions.

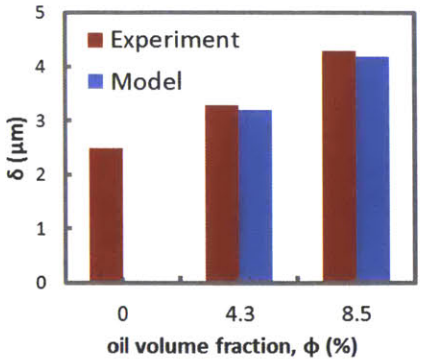

Figure 5.6 – Inhibition layer thickness, δ, grows with PFC content showing quantitative evidence for facilitated transport of O_2.

To compare the theoretical prediction with experimental data, we synthesized disc-shaped particles containing 0%, 4.3% and 8.5% PFC emulsion (C_s=20 mM) in a 50 μm tall device and estimated the inhibition layer thickness, δ, from the corresponding particle height measurements (**Fig. 5.6**). δ is assumed to be symmetric with respect to the channel center. The experimental estimates agree with model predictions to within 0.1 μm. It is seen that δ grows with φ, as a result of 1) faster O_2 transport and 2) greater O_2 solubility. The latter contribution is stronger, especially at higher oil volume fractions. In a PFC emulsion solution, oxygen can exist and freely diffuse between two different chemical environments, thereby increasing the overall effective concentration that must be overcome during synthesis in order to reproducibly generate composite microparticles.

One of the practical implications of the theoretical analysis presented above is that to achieve particle feature resolution on par with the cellular length scale (~10 μm), one must overcome the engineering challenge of controlling the oxygen environment in the immediate vicinity of the microfluidic device during particle synthesis. We note that other more direct methods of expediting polymerization kinetics, such as adding in more photoinitiator or crosslinker, result in droplet aggregation (**Fig. 5.7**).

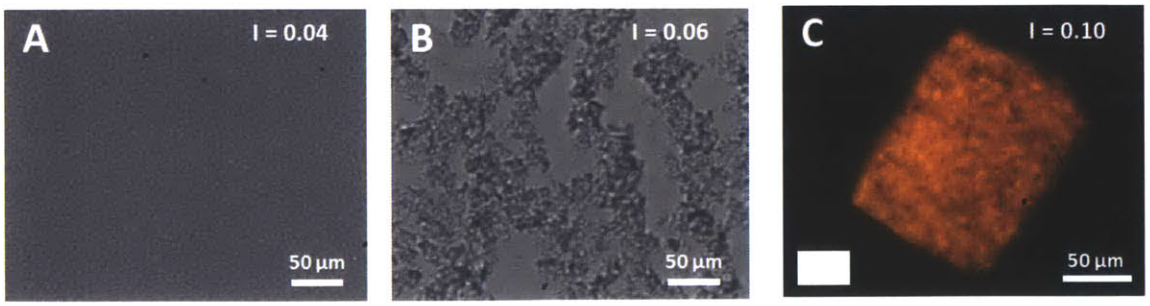

Figure 5.7 – Droplet aggregation. Micrographs of a 8.5% by volume PFC nanoemulsion (φ_1=0.08, φ_2=0.005, C=20 mM , P=0.36) of (A) 4% photoinitiator, (B) 6% photoinitiator, and (C) 10% photoinitiator made into a rectangle-shaped particle using SFL.

To demonstrate that we can generate RBC-like, 10 μm composite particles, we placed a synthesis device in a custom-made purge chamber. Use of the chamber afforded two distinct advantages: 1) it allowed particles to be patterned in a more controlled fashion, according to the *size and shape* of the lithographic photomask, and 2), it enabled us to alter the O_2 concentration using an inert gas (e.g., argon). Oxygen concentration is a crucial control parameter during the synthesis of cell-sized, geometrically-complex features (non-circular, or with internal cavities, for example). The modified SFL setup is shown schematically in **Fig. 5.8A**. The chamber was loosely sealed with side inlets for introducing argon and/or air. We degassed an 8.5% PFC emulsion prepolymer by slowly bubbling argon for 60 minutes prior to flowing it into the microchannel. This pre-synthesis treatment step lowered the oxygen concentration, and improved the particle resolution (**Fig. 5.8C**, *i*), though the disc-shaped particles remain underpolymerized, in the in-plane and out-of-plane (height) dimensions. To decrease $[O_2]$ further, we performed particle synthesis within the purge chamber under gentle influx (~1 psi) of argon. By polymerizing the same sequence of circles (**Fig, 5.8B**, right) using identical exposure conditions (800 ms) at discrete time points, we show that 10 μm (diameter) x 10 μm (height) composite microparticles can be made after 50 minutes of Ar purge (**Fig, 5.8C**, *iii*, white arrow). This timescale is dictated by the diffusion of argon through the PDMS device. To emphasize the deleterious effects of O_2 on polymerization kinetics, we let the PDMS device re-saturate with oxygen. ~40 minutes after the removal of the purge chamber (**Fig, 5.8C**, *iv*), the achievable feature resolution returned to the pre-purge state, again showing the inhibitory effects of oxygen.

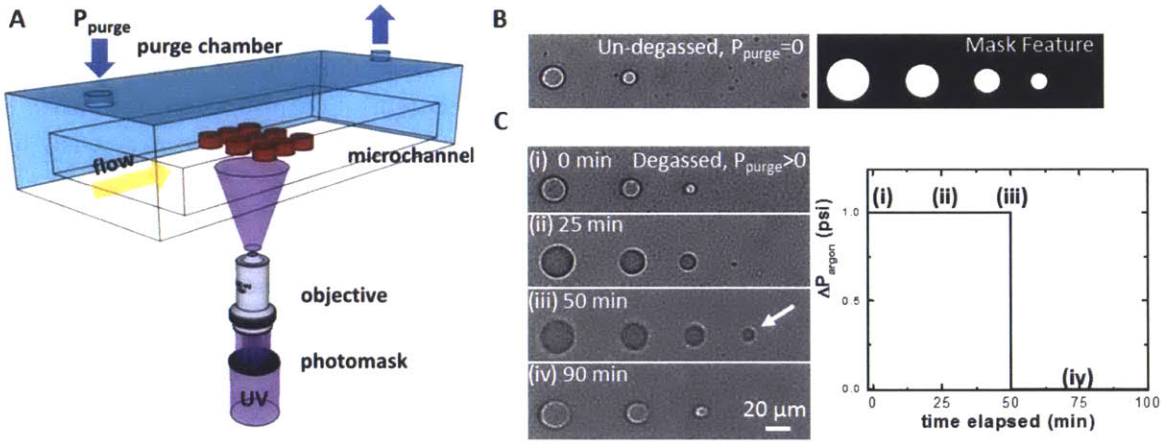

Figure 5.8 - Stop-flow lithography (SFL) experimental setup. (A) Schematic drawing showing the formation of an array of biomimetic composite disc-shaped particles using SFL. A prepolymer containing crosslinkable PFC-in-water nanoemulsions is flowed through a PDMS synthesis device and polymerized via controlled pulses of mask-defined UV light through a microscope objective. The gel particles are then advected downstream for collection. The synthesis device is enclosed in a custom-made purge chamber, which allows the exchange of an inert gas. Micrographs showing the polymerization of a series of circular mask features (B, right) in nanoemulsion prepolymer stream (φ_1=0.08, φ_2=0.005, C_S=20 mM , P=0.36, I=0.04) that is (B, left) un-degassed, at ambient conditions (no purge chamber), and (C) degassed for 60 min, and in the purge chamber under a constant influx of argon. The particle in-plane feature resolution improves over time. (iii) The 10 μm feature (white arrow) fully polymerizes after 50 min of Ar flow. (iv) 40 min after Ar flow has been turned off, the feature resolution returns to the initial configuration.

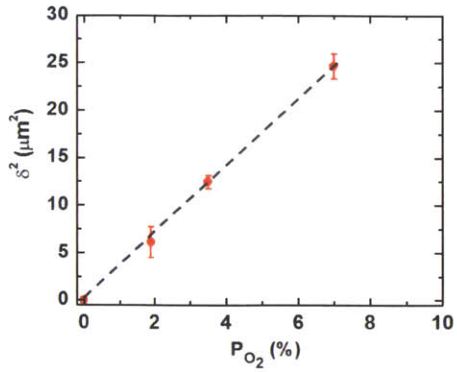

Figure 5.9 - Variation of inhibition layer thickness, δ, with oxygen partial pressure (P_{O2}). The linear trend observed in the δ^2 vs. P_{O2} space agrees well with the known scaling relationship Eq. (5.5) discussed previously. A dash line is drawn to guide the eye.

Interestingly, controlling the amount of oxygen present during particle synthesis presents a simple method to fabricate particles of different heights *within the same channel* without resorting to sheath flows above and below the prepolymer stream. To show this, we quantified the change of inhibition layer thickness as a function of the surrounding oxygen partial pressure in the purge chamber. The oxygen partial pressure was manipulated by controlling the inlet pressures of two purge gas streams: air (21% O_2) and argon (0% O_2). After the synthesis microfluidic device equilibrated with the surrounding gas mixture, we fabricated 25 μm (side) squares in a 30 μm tall device. To measure the inhibition layer thickness, we toppled the particles by temporarily applying a sharp pressure pulse (~ 1s), which caused them to fall onto their sides. The results are shown in Fig. 5.10. As the concentration of oxygen decreases, δ decreases sharply. Furthermore, we recover the known scaling, $\delta^2 \sim [O_2]$, derived previously by Dendukuri et al. [37].

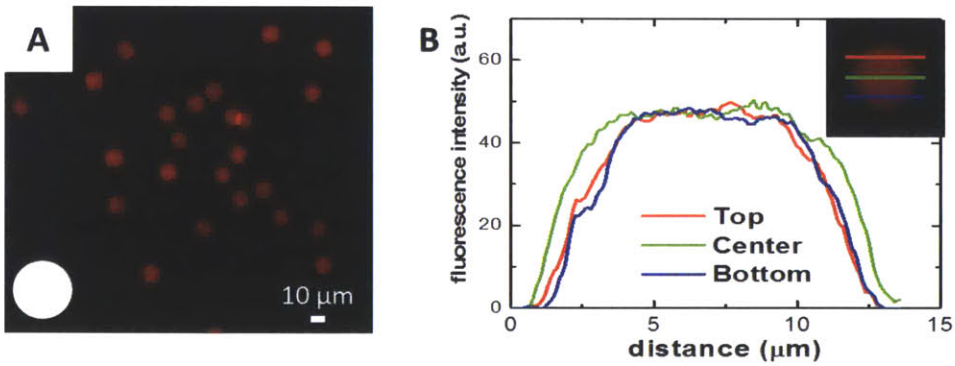

Figure 5.10 – (A) Fluorescent micrograph of 10 μm (diameter) by 10 μm (height) disc-shaped particles pre-loaded with PKH26. The transparency mask feature used during synthesis is shown in the lower inset. (B) Spatially resolved fluorescence intensity profiles (a.u. = arbitrary units) taken across three different lanes of the particle shown in the upper inset.

5.4.3 Composite particle analysis

A fluorescent micrograph of a typical collection of 10 μm (diameter) by 10 μm (height) PFC nanoemulsion composites is shown in **Fig. 5.10A**. We made these particles in a 20 μm-tall device using a degassed, PKH26-labeled prepolymer (10 μM) in the purge chamber, after ~60 minutes of Ar flow. PKH26 is a lipophilic dye that readily partitions to the droplet interface. Based on dimensions of the purge chamber (0.1 m x 0.1 m x 0.05 m), and an estimated Ar flowrate of $\sim 10^{-3}$ m^3/s under well-mixed conditions, the purging step reduced the oxygen concentration in the head space above the microfluidic device by $\sim 10^4$-fold. During synthesis, we turned off the purge stream to maintain the gas environment at pseudo-steady state. Excessive argon purge caused particles to adhere to the PDMS device due to the complete lack of O_2 inhibition. Photoluminescence analysis on individual particles indicated uniform droplet loading (**Fig. 5.10B**). We can also synthesize particles of other 2D-extruded shapes by using different photomasks. A triangle-shaped particle (φ_1=0.08, φ_2=0.005) is shown in **Fig. 5.11**.

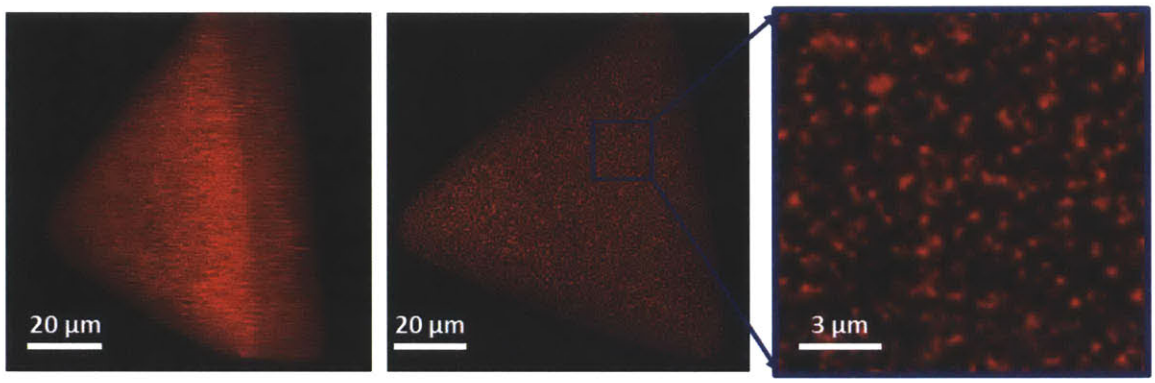

Figure 5.11 – A representative confocal micrograph of a large triangle-shaped particles (100 μm/side, $\boldsymbol{\varphi_1}$=0.08, $\boldsymbol{\varphi_2}$=0.005, C=20 mM , P=0.36, I = 0.04) synthesized using SFL. The average diameter of the encapsulated droplets is ~200 nm. The droplets, which are pre-labeled with 10 μM PKH26, are homogeneously distributed throughout the particle.

To ascertain that oil droplets did not undergo aggregation during particle synthesis, we synthesized 20 μm (diameter) by 10 μm (height) disks using a prepolymer containing 0.01% by volume nanoemulsion. The low oil volume fraction allowed us to distinguish individual emulsion droplets. Confocal images of higher volume fraction particles are shown in Fig. 5.12. The oil volume fraction was lowered by diluting the canonical prepolymer formulation using pure continuous phase without altering the bulk surfactant concentration. At such a low φ, using a 100x oil objective and imaging *z* slices at 100 nm intervals, we observed droplets randomly dispersed throughout the particle, kinetically arrested by the gel network. Two representative orthogonal optical sections are shown in Fig. 5.12. Furthermore, the volume fraction of encapsulated droplets matched that which was originally present in the prepolymer solution. In this analysis, we first identified the number of droplets in confocal *z* scans manually using ImageJ. We then estimated the volume fraction of the encapsulated droplets by using the initial average droplet diameter (197 nm) in the prepolymer solution, an estimated depth of focus (1.6 μm), and the diameter (20 μm) of the composite gel particle. The encapsulated oil volume fraction was found to be ~0.012% or 20% greater than φ in the prepolymer. This result is within the uncertainty of our measurement due to the polydispersity of the droplets. This suggests that the droplet loading remained unaffected by polymerization.

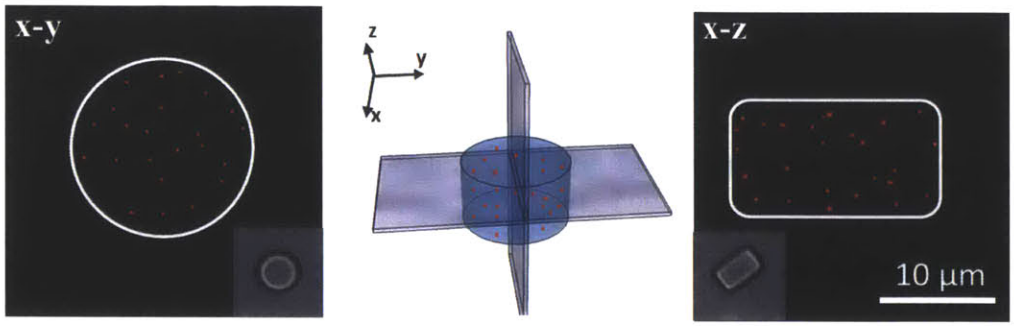

Figure 5.12 – Laser confocal images (left: x-y plane, right: x-z plane) of a 20 μm (diameter) x 10 μm (height) disc-shaped composite particle (φ=0.0001, C_S=20 mM, P=0.36, I=0.04) showing even dispersion of PKH26-labeled PFC nanodroplets. (Insets) The corresponding cross-sectional bright-field images. Schematic (center panel) marks the approximate locations of the representative confocal slices.

Finally, encapsulating PFC nanodroplets in the hydrogel network allows us to arbitrarily tune the bulk surfactant concentration by simple washing steps post-synthesis. Excess surfactant, orders of magnitude greater than the critical micelle concentration (CMC), is required to minimize the final droplet size by 1) lowering the surface free energy, and 2) stabilizing newly formed droplets against shear-induced coalescence during homogenization. However, for many cellular assays, having such a high concentration of surfactant is undesirable, as it may compromise membrane integrity and result in cell lysis and protein denaturation [156]. Studies have also shown that surfactants may cause skin irritation [157], or trigger immune responses (i.e., complement activation, anaphylactic-type reactions) *in vivo*, at low test doses [158]. Kinetically arresting the droplets in gel particles allows us to use centrifugation to quickly sediment the nanoemulsion composites and replace the surfactant-rich supernatant with pure buffer. To demonstrate this, we measured the surface tension of the displaced supernatant solution after a number of rinsing steps using the pendant drop method, and estimated the corresponding PF68 concentration from a calibration curve (Fig. 5.3B). As seen in Fig. 5.13, the surfactant concentration decreased by ~4 logs after 4 short (2-minute) rinse cycles. The washing procedure had a negligible effect on the stability of the encapsulated droplets (Fig. 5.12). We emphasize that it is not possible to generate small droplets ($\langle 2R \rangle$~200 nm) under nearly surfactant-free conditions *a priori* due to surface tension effects.

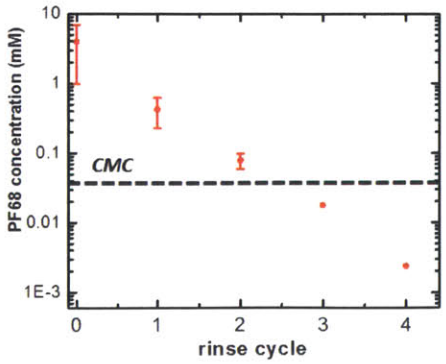

Figure 5.13 – Concentration of Pluronic F-68 (PF68) in the supernatant of particle storage solutions as a function of the number of rinse cycles. The dashed line indicates the experimentally determined critical micelle concentration (CMC) for PF68 in water at room temperature.

5.6 Conclusions

In summary, we presented a versatile microfluidic approach for photo-patterning PFC-laden nanoemulsion composites with resolution down to the cellular length scale (~10 μm). The PFC droplets are randomly distributed throughout the gel interior. We proposed a simple steady-state two-phase diffusion model to successfully predict the accelerated rate of O_2 mass transport in the presence of PFC nanodroplets. To minimize the impact of excess oxygen on polymerization, an enclosed chamber with a purge gas inlet was used to control the oxygen environment around the PDMS synthesis device.

The composite gels are a novel strategy of formulating nanoemulsions for biomedical applications. This approach alters the way biological entities perceive and interact with the nanodroplets. The physico-chemical properties of the gel network (i.e., chemical functionalization, size, shape, deformability of the particle) may be readily tuned to achieve the desired cellular interaction (via ligand binding, for example), circulation time, biodistribution pattern *in vivo*. The encapsulated oil droplets can be varied in size, loading and composition, depending on the 'cargo' of interest (e.g., chemotherapeutic drug or imaging agent, etc.) and the desired release rate and delivery profile. As a drug delivery platform, nanoemulsion composites provide a promising route to achieve the targeted and systemic delivery of fragile actives.

In particular, the PFC-laden composite gels could be used during cell culture to combat diffusion limitations on oxygen and essential nutrients. Conversely, the same microparticles could be used as devices for photodynamic therapy where, in the presence of excited photosensitizers (e.g., hydrophobic organic dyes), the PFC droplets act as reservoirs for the generation of singlet O_2, a cytotoxic agent known to inactivate tumor cells [159].

CHAPTER 6

Conclusions and Outlook

In this thesis, we devised a modified flow lithography technique based on SFL for synthesizing non-spherical, Brownian hydrogel microgels. Furthermore, we drew inspiration from an important architectural motif of eukaryotic cells – namely their compartmentalized structure - and created biomimetic composite microparticles from polymerizable oil-in-water nanoemulsions. These particles are candidate materials for variety of biomedical applications, such as controlled encapsulation and release of therapeutic cargoes.

The flow lithography family of techniques that have been developed recently is unique in that, unlike most current synthesis, particle size, shape, material chemistry, modulus and internal structure (the latter was the centerpiece for this thesis) can be independently tuned. Moving forward, an important upcoming milestone for FL is to be able to pattern soft hydrogel particles with precisely engineered interfacial properties (e.g., surface charge, surface chemistry) [4]. Studies have shown surface properties can influence particle interactions with biological systems (e.g., internationalization by epithelial cells, [160]).

To that end, layer-by-layer assembly (LbL) is a promising nanoscale film fabrication method that can be used. An unprecedented variety of different materials have been employed as constituents for multilayer films. Their assembly via LbL is most commonly driven by electrostatic attraction, hydrogen bonding or hydrophobic interactions [161]. However, synthesis of LbL-coated micro/nanoparticles to date has been limited in spheroidal shape and nonporous or inorganic polymer templates [7, 162-167]. Many more novel particle morphologies can be created by combining SFL with LbL as a streamlined process, including

ultra-soft, red blood cell-like hollow shells, and capsules containing nanoemulsion droplets and/or biological molecules. Erosion of non-spherical hydrogel core is achievable using hydrolysis or degradable polymers. Laminar coflow at the microscale and advanced flow lithography methods (e.g., hydrodynamic FL) can also be leveraged to create 'patchy' multifunctional particles.

Equally important to the synthesis of biomimetic particles is the study of their flow in microvascular networks. Kamm and coworkers recently developed cell-lined, microfluidic vascular networks (μVNs) [68] that recapitulates key structural elements of natural blood vessels. This biomimetic platform is a novel method for systematically investigating the transport, margination and adhesion of non-spherical microparticles *in vitro*. Results from these experiments complement existing *in vivo* data and can serve as a guide for planning new studies on small animal models. Earlier, we presented proof-of-concept demonstrations that show the successful passage of colloidal discs through vascularized region of μVN microfluidic devices. More work should be done with the goal of gaining detailed, mechanistic insight on shape, deformability and surface charge effects.

In terms of *in vivo* studies, a handful of studies completed within the past decade stressed the importance of particle-based carrier attributes (i.e., size [55], shape [10], deformability [91], etc) on prolonged circulation. Although PEG-based microparticles are generally accepted as ideal biocompatible vehicles for the targeted delivery of valuable therapeutic payloads and imaging modalities, understanding of their distribution and clearance remains largely phenomenological and limited to a small repertoire of particle shapes. This is a fertile area that deserves systematic consideration. We performed preliminary experiments in mice (*Appendix B.1*), with help from Dr. Kathryn Whitehead and managed to detect the particles using a whole-body imaging system. In the future, large-scale contact flow lithography synthesis is ideal for rapidly generating mL sample quantities to form a particle library for *in vivo* experimentation.

In reality, the joint power of the photolithography and microfluidics extends beyond synthesizing anisotropic microparticles. One can also utilize this combination to create a controlled microenvironment and interrogate particle mechanical properties. Well-characterized microflows (i.e., shear and elongational) have historically been used to study the force-extension of model polymers, such as DNA, in single-molecule studies [168-170]. Thus far, similar studies that probe the flow response of deformable hydrogel microparticles have seldom been reported [7, 27]. An interesting and under-explored facet of this project centers on the development of novel on-chip mechanical tests for soft hydrogel microparticles. The flow assay results should ideally complement that of traditional and more established particle characterization techniques, such as AFM.

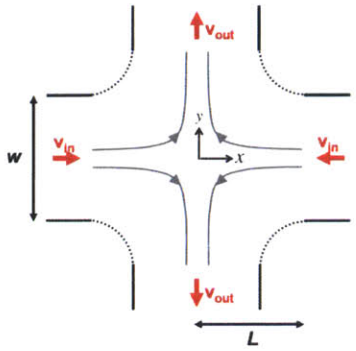

Figure 6.1 – Schematic diagram (adopted from ref. [171]) of a cross-slot channel, with four converging streamlines (shown in gray). This device has two inlets and two outlets. The shape of the sidewalls can be described by $\boldsymbol{xy = wL/2}$, where $\boldsymbol{x}$ is the distance away from the center of the channel (stagnation point). The contour of the sidewalls matches the streamlines in a planar homogeneous elongational field so as not to disrupt the region of uniform strain rate achieved near the stagnation point of the device.

In addition to the entry flow-based characterization methods (*Appendix A.2*), *in-situ* synthesis (akin to setting the initial conditions for computational simulations) and flow characterization of sterically-pinned hydrogel microstructures in cross-slot microchannels (Fig. 6.1) is another promising route worth pursuing. Whereas the kinematics of contraction flows tend to compress, bend and/or twist the deformable particles, flow dynamics in cross-slot channels near the stagnation point leads to particle stretching. The concept of investigating the flow-extension properties of immobile soft hydrogel particles arises naturally from previous work done on in situ fabrication of functional hydrogel microstructures, including anchored flow sensors and pH-responsive valves [172, 173]. Two possible *in situ* flow testing configurations are described below.

- Micro-springs (e.g., in the shape of folded ribbons) parameterized by width a, radius curvature r and resting length l can be synthesized using PEG-DA chemistry around prefabricated posts near the stagnation point of a cross-slot device, with the two free ends pointing toward the outlet reservoirs. The sterically-pinned nature of the resulting hydrogel microparticles allows one to bypass manual trapping of mobile particles at the stagnation point for subsequent stretching experiments. Particle flow characterization (e.g., relative extension vs. flow rate for a range of particle heights) can be performed in the same channel once the excess prepolymer solution containing unreacted monomers and photo-initiators is flushed out.

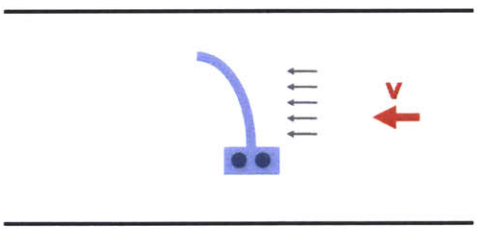

Figure 6.2 – Schematic diagram of a 'micro-beam' deforming under steady flow in a straight microfluidic device.

- Steady hydrodynamic flows can also be used to obtain material properties such as the elastic modulus E and bending stiffness B ($B = EI$, where I is the area moment of inertia) of hydrogel microparticles. The elastic modulus of linear micro-beams with length l, width w, and height h can be estimated using flow-induced beam deflection measurements in simple microfluidic devices (consider also, alternative geometries, i.e., tapered or curved beams). The micro-beams can be anchored on one side around stationary PDMS blocks, while the free end is subjected to bending forces/moments due to the presence of a steady flow in the transverse direction (Fig. 6.2).

APPENDIX A

Tips and Tricks

A.1 Synthesizing thin, Brownian particles using O_2-controlled SFL

The order in which you add ingredients in the prepolymer is important, especially the photoinitiator (Darocur® 1173) and aqueous buffer since the former is almost completely immiscible in water. Try to add PEG-DA700 first, followed by PEG200 (if necessary, this is often used as a porogen) and vortex for at least 10 seconds. Then add Darocur® 1173 (for making sub-micron particles, at least 10% v/v is required) and vortex for another 10 seconds. Finally, add any aqueous buffer and/or fluorescent dye (e.g., rhodamine-acrylate) stock solution and vortex. Vortexing is important to make sure you have a single phase solution rather than an emulsion. I typically prepare 200 μL of prepolymer solution (this will allow you to run at least two experiments, in case your first try fails, due to channel malfunction, for example).

The final channel design that I used is a two-layer device with inlet and outlet regions that are 35 μm tall and a set of 4 parallel 200 μm wide, 1.4 mm long, and 2 μm tall channels in the center bridging the inlet and outlet reservoirs. The flow and stop times for the final channel design are reasonably fast, $\sim O(1\text{s})$.

Generally speaking, for thin particle synthesis, the channel height is the critical dimension but just as important is the channel length and width. In the polymerization region, the channel must be as short as possible to minimize flow and stop times and it must be narrow enough to

prevent sagging. Outside of the polymerization region, any channel height, width, or length can be used as long as the flow resistance is smaller than in the polymerization region.

The channel will fill slowly so you have to wait about 15-20 minutes at moderate driving pressures (~5 psi) until there is a sliver of pink (from the dye) in the outlet/collection reservoir. You can watch the filling process through the eyepiece on the microscope (5x objective) to make sure there are no problems (clogs or air bubbles). Once the entire system is connected fluidically, turn on the argon/air taps and wait for the system to equilibrate.

While the channel is filling, place the photomask into the first position of the filter slider. First, put a circular glass cover slip into the filter holder and then drop in the photomask. Then place the rubber O-ring into the filter holder and press it down firmly with a pair of tweezers to ensure it is flush against the photomask. Finally, rotate the photomask until it is in the correct orientation to align with the polymerization channel walls.

Typical settings on the Uniblitz controller for polymerization cycles are: Hold = 500 ms, Exposure = 100 ms, Stop = 1500 ms, Flow = 1500 ms but they can be varied as needed for each individual polymerization run. I set the magnification at 20x (the corresponding de-magnification factor is 7.8; this should be taken into account when designing particle masks). 40x will also work, but is harder to use since the depth of field is very shallow.

I typically align the masks by polymerizing once near the channel outlet, and note the location of the particle array on the computer monitor with colored tape afterward. I then focus on the edge of the polymerization channel and optically zoom in (using the camera software) on the viewing window, as these particles are too small/faint to see otherwise. The two middle channels in the polymerization section usually work the best. Below 10% O_2 (and above ~3%), I have noticed empirically that particles won't begin to stick to the PDMS until at least 20-25 minutes of continuous polymerization.

After I have enough particles, I turn off the fluorescence shutter and turn on a constant flow (~6-8 psi). Under these conditions, it takes about 60 minutes to flush out the channel. I watch the inlet reservoir (under the modified pipette) until I see an air-prepolymer interface appear and begin to move down into the channel. I lower the pressure to 4 psi and allow air to flush through the channel into the outlet vial. I then remove the channel from the microscope stage and detach the outlet vial while it is being bubbled with air.

To rinse the particles, I place the sample vial in the desktop centrifuge for ~10 minutes. The long spin time is necessary since the particles are small and almost neutrally buoyant, even in aqueous buffer (for larger particles, ≥ ~100 μm, the vacuum suction/filter setup may come in handy). I replace the supernatant fluid (leaving about 75-100 μL at the bottom) with 600 μL of fresh PBST buffer, and vortex the vial for ~10 seconds before centrifuging for another 10 minutes. I repeat this process at least 5 times.

A.2 Flow Testing for Thin Particles

To test the flexibility of the thin, red blood cell-like particles, my predecessor, Ramin Haghgooie, designed a device containing parallel contractions through which the particles are squeezed. The channel design is simple, with a 1.6 mm x 200 μm approach channel from the inlet, 5 parallel

4 μm-wide contractions, and a large 1 mm x 1 mm exit region with support posts to keep it from sagging. This method of characterizing particle deformability was motivated by the *in vivo* microvasculature.

In this section (adopted from a report written by Ramin), I will discuss preparing the channels for an experiment, running the experiment, and analyzing the results.

Preparing the flow test channels

I punch holes in the inlet and outlet regions of the channel and bond the channel to a clean glass coverslip via oxygen plasma. I prepare a 200 μL modified pipette tip to be the inlet reservoir and attach tubing to the back end. I then fill the pipette tip with about 50 μL of the particle suspension and then I pull in another 10-20 μL of PBST. I place the pipette tip in the inlet reservoir and connect the tubing to the pressure source. I set the pressure to ~3 psi and then open the solenoid valve to turn on the flow. The channel fills with buffer and I watch the inlet reservoir at 10x magnification until I start seeing particles flow towards the entrance of the channel. I then stop the flow and set the desired pressure.

Running the flow test channels

For a given pressure drop across the channel, I open the solenoid valve to begin flowing the particles through the contractions. I observe the channel at 10x so that I can see the entrance region, the contractions, and part of the exit region. It is usually important to see all three regions because typically, the particles move very fast through the actual channel and contractions so they are hard to see in those regions. Generally, I count the number of particles entering the channel from the entrance region and then I count how many are exiting through the exit region. I then note the fraction of particles that pass through the contractions. If too many particles are getting stuck in the contractions I stop the flow, increase the pressure, and resume flow for a very short time (a pressure pulse) to push them through. The pressure pulse required to push trapped particles through the contractions can be fairly large (larger than what is necessary to push them through when they are not stuck). I try to collect data for at least 20 particles entering the channel for each pressure drop.

At very high pressure drops (>5 psi), the particles move through the channel very quickly and it is impossible to see them actually inside the channel. In this case, I focus the viewing window on the outlet reservoir (where the particles slow down as they exit the device). I allow the sample to flow for 10-15 seconds during which I count how many particles (they will appear more or less as bright streaks) are entering the outlet reservoir. When I stop the flow, I zoom in on the contractions and count how many particles are stuck (if any). I repeat this process as necessary until I gather enough data points.

Calculating the pressure drop in the contractions

After gathering the raw data (percent passage vs. overall channel pressure drop), it has to be recast in terms of percent passage as a function of the pressure drop across the contractions. To

do so, I used COMSOL to calculate the flow field within the channel (see sample numerical results below).

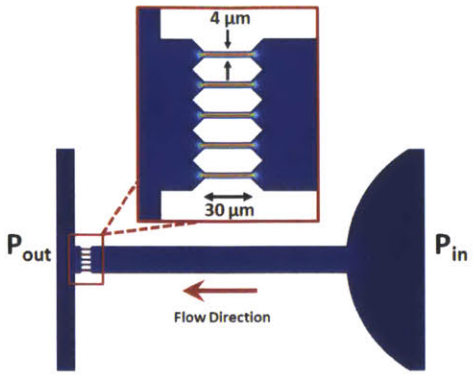

Figure A.1 – Fluid velocity profile inside the contraction device as calculated using COMSOL;

I used the MEMS module with the microfluidics package and general laminar flow conditions (Fig. A.1). I set constant pressure boundary conditions at the inlet and outlet of the channel. The resulting flow and pressure profiles were calculated for several different pressure drops across the entire channel, and are in close agreement to Ramin's data. From the pressure profile, I was able to determine that the pressure drop across the contractions is *23% of the total* across the entire device.

A.3 Functionalizing Particles with Acrylic Acid

Acrylic acid can be added to the prepolymer so that the final particles will be functionalized with carboxyl groups, which enables layer-by-layer assembly, conjugation of biomolecules, as well as the creation of field-responsive particles. In a 30 μm tall channel, particles can be made easily using 20% PEG-DA700, 30-40% AA (acrylic acid) and 5% Darocur® 1173, by volume.

A.4 Partitioning of Photoinitiator to PDMS

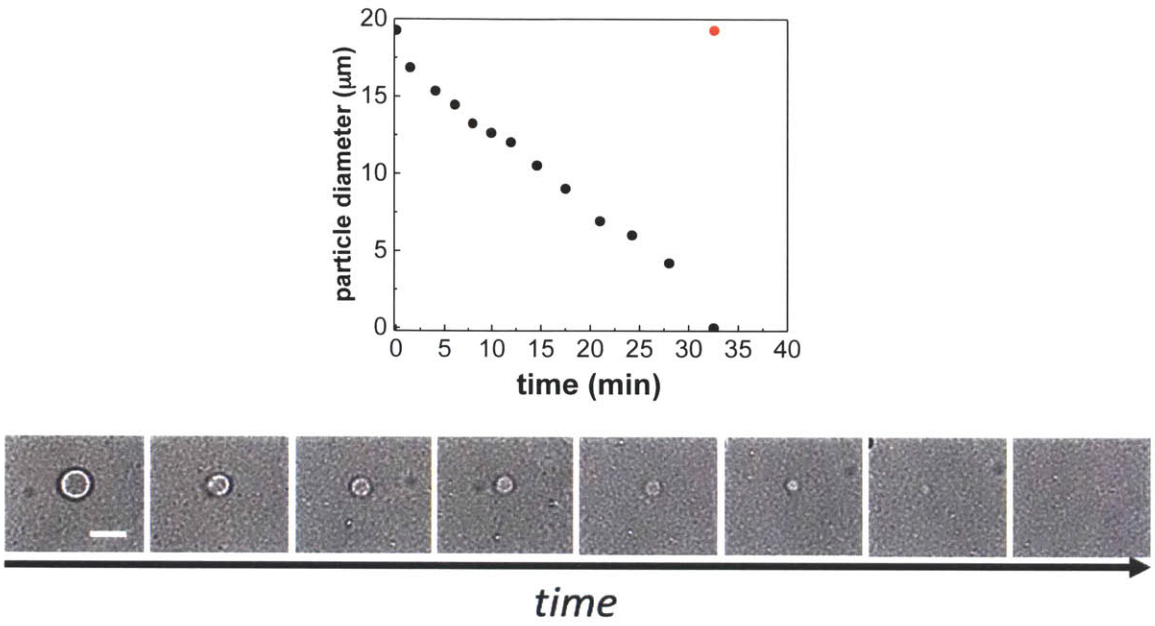

Figure A.2 – Feature resolution deteriorates over time due to partitioning of the photoinitiator to PDMS. The original/unperturbed state can be recovered by flowing in fresh prepolymer. Scale bar is 20 μm.

Note that the photoinitiator (e.g., Darocur® 1173) partitions, presumably to the confining PDMS walls, at long times, ~O(30 min). As a result, the practical feature resolution during synthesis steadily decreases over time. Fig. A.2 shows changes in the in-plane dimension of 18 μm (diameter) disc-shaped composite particles (the out-of-plane, i.e., height, dimension also diminishes). To recover the original feature resolution, simply flow in new prepolymer (Fig. A.2, red circle).

A.5 Using Autocad

- You can download Autocad for free at *http://students.autodesk.com/*
- There are a series of short video tutorials on how to use Autocad posted on the group Dropbox.
- I recommend the "classic" layout option, in which the four toolbars of interest to you to satisfy basic mask design needs (for particle synthesis and wafer fabrication) are clearly laid out:
    - *Draw* (left): create lines, circles, and polygons, etc.
    - *Modify* (right): manipulate objects (e.g., move, rotate, copy, scale, array, mirror)

- *Layer properties* (top): toggle layer on/off, or locks them
- *Object snaps* (bottom): automatically select a specific point or place on an object (e.g., endpoint, intersection, midpoint, tangent, center, etc). You can turn different osnap options on/off using this toolbar. This is a useful feature in Autocad to help you improve your drawing precision, especially when it comes to drawing composite shapes.

- Always read the messages displayed in the command prompt, follow the instructions given
- Useful commands: *trim*, and *pedit* (modify grouped lines/arcs in several ways, i.e., join)

A.6 Using ImageJ

Fluorescence analysis

- Re-scale intensities in all fluorescence images (*image -> adjust -> brightness/contrast*)
- Create a duplicate (*image -> duplicate*) for each image, and convert them to 8-bit grayscale (*image -> type*). Set threshold (*image -> adjust -> threshold)* to define particle mask (Fig. A.3).

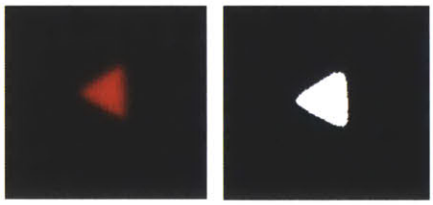

Figure A.3 – Re-scaled fluorescence image of a triangle-shaped particle (left) and its mask (right).

- Where fluorescence threshold masking is not possible, a mask can be manually drawn using the corresponding bright-field image (Fig. A.4).

Figure A.4 – Re-scaled fluorescence image of a decomposed triangle-shaped particle (left), its corresponding bright-field image (center), from which a particle mask (right) can be extracted using the freehand selection tool.

- Calculate mean intensities : I_p = average pixel intensity in particle (white in mask) and I_b = average pixel intensity in supernatant (black), and compute
    - Normalized particle intensity: $\left(I_p(t) - I_b(0)\right) / \left(I_p(0) - I_b(0)\right)$
    - Normalized background: $\left(I_b(t) - I_b(0)\right) / \left(I_p(0) - I_b(0)\right)$

  using *analyze –> set measurements* (redirect to re-scaled image), followed by *analyze –> analyze particles.*

- This is a good way to obtain fluorescence and size information from a population of particles. You will need to image a stage micrometer using the appropriate objective to obtain the desired pixel to micron conversion factor.

Generating 3D renderings from confocal images

- Use the 3D viewer (downloadable on the internet) to assemble 3D particle renderings (e.g., Fig. 3.4B) from confocal image stacks. For publishable results, particles to need to remain perfectly still during image acquisition. This could be a problem if the particles are Brownian, in which case, consider increasing the viscosity of the storage buffer (i.e. by adding glycerol).

Creating FL/bright-field composite images

- Import images or stacks separately and use the *merge channels* option under the *image* pull-down menu. This procedure is helpful for showcasing particles with multiple chemistries (see, for example, Fig. 4.7E).

A.7 Preparing Oil-in-water Nanoemulsions

Prepare the pre-emulsion:

1) Prepare the continuous (aqueous) phase.

2) Aliquot desired volume of aqueous phase into bottle using disposable pipette. Place large stir bar in bottle.

3) Aliquot desired volume of oil into burette using disposable pipette (note: for consistency, base volume measurements on the disposable pipette, not the burette). Mount burette on stir plate.

4) Place bottle on stir plate below burette, and set stir plate to 750 rpm (or some other value). Leave at room temperature.

5) Slowly open stopcock of burette until oil drips steadily from tip.

6) Drip oil until burette is empty, then continue stirring at 750 rpm for 5 minutes.

7) Sonicate pre-emulsion for 5 minutes to consolidate air bubbles.

8) Using a disposable pipette, transfer any foam from pre-emulsion to a waste container.

Homogenization:

9) Load pre-emulsion into sample cylinder and prime pump.

10) Homogenize at desired pressure. While homogenizing, monitor both the sample cylinder (to ensure the homogenizer does not draw in air) and the collection bottle (for some compositions, e.g., silicone oil-in-water/PEGDA, samples may form a gel, and become too viscous to homogenize further).

11) After the desired number of passes (typically 15-20), collect product into a clean 50 mL centrifuge tube(s).

12) Place the collected sample in sonicating bath for 5 minutes immediately after collection to consolidate/eliminate air bubbles. Remove and let cool to room temperature. Place in refrigerator if necessary.

Storage and handling:

13) If dilution of the emulsion is necessary, dilute using continuous phase of the same PEGDA concentration *without* any surfactant. This may result in the coalescence of a small fraction of droplets, resulting in a slightly turbid suspension. If so, a syringe filter can be used to successfully eliminate the population of large droplets.

A.8 Using the EmulsiFlex-C3 Homogenizer

Before turning on the C3:

1) Ensure that all air supply hoses are connected correctly, and that the three pressure gauges on the air manifold and front of the C3 read 0 psi (consult manual for details).

2) Ensure that the red "STOP" button on the front of the C3 is pushed in.

3) Ensure that all check valves and fittings are properly installed. If one or more of the fittings has been recently removed/inserted, check to make sure it is firmly tightened.

Initializing the C3:

4) Open the high pressure air supply valve on the wall (yellow lever), and check the pressure gauge on the air manifold. The pressure reading should be at least 75 psi.

5) Initialize power to the C3 by turning the yellow knob on the back of the instrument to the vertical "ON" position. After several seconds, the red "STOP" button on the front of the C3 should light up. Wait at least 30 seconds to allow the power transformer to warm up.

6) Attach the sample cylinder (if not already attached) by first ensuring that the rubber seal is properly seated, then attaching and tightening the collar. For sample volumes less than 40 mL, or for air-sensitive samples, see the C3 instrument contact for use of the sample syringe fittings.

Preparing the C3 for homogenization:

7) Pour the sample (*Appendix A.7*) to be homogenized into the sample cylinder. Make sure the sample is well mixed before pouring. Place a sample collection container below the C3 outlet tubing.

8) Ensure that the homogenization valve is fully open by turning the "AIR REGULATOR" knob counter-clockwise until it turns freely.

9) Prime the homogenizer pump: turn the red "STOP" button clockwise until it pops out, and then press the green "START" button. The pump will begin to stroke and flow sample through the unit. Watch the outlet tubing. The pump is fully primed once no air bubbles can be seen passing through the outlet tubing. Once the pump is primed, press the red "STOP" button.

10) Close the homogenization valve by slowly turning the "AIR REGULATOR" knob clockwise until the "AIR PRESSURE" gauge reads ~35 psi.

Homogenizing the sample:

11) Turn the "STOP" button clockwise, then press the green "START" button, and watch the large homogenization pressure gauge. After several strokes, the device should begin homogenizing at a peak pressure of 5-10 kpsi. If not, continue to slowly increase the air regulator pressure until it does. (Note: you can press the red "STOP" button to stop the pump at any time)

12) Adjust the "AIR REGULATOR" knob until the desired homogenization pressure is achieved. It can take several strokes for changes in the air pressure to produce changes in the homogenization pressure. Once the desired homogenization pressure has been reached, you may wish to stop the pump to collect the material that has already been homogenized before starting again.

13) Continue homogenizing the sample at the desired pressure. During the first few strokes, the homogenization pressure may vary significantly as the sample heats and becomes more (or less) viscous. If so, adjust the "AIR REGULATOR" knob as needed to adjust the homogenization pressure back to the desired reading. For highly viscous or yield stress fluids, pressurization of the sample cylinder may be required. Consult the manual or the C3 instrument contact for details.

14) Collect the sample into an appropriate container. If heating/cooling of the sample is desired, see the C3 instrument contact for use of the heat exchange coil.

15) As the sample is being homogenized, watch the fluid level in the sample cylinder. Before the fluid level reaches the bottom of the conical section, press the red "STOP" button. *Do not allow the C3 to draw in air while homogenizing, as this can cause both foaming of the sample and damage to the homogenization valve.*

16) If multiple passes through the C3 are desired, pour the contents of the sample collection container back into the sample cylinder, and repeat steps 11-15.

17) After the final pass through the device, collect the remaining sample holdup. While the C3 is stopped, open the "AIR REGULATOR" knob until the "AIR PRESSURE" gauge reads zero, then start the homogenization pump. The remaining material will flow out the outlet tubing. You may wish to collect this material separately from the remaining sample, as it will most likely contain air bubbles.

Cleaning the C3 after use:

18) After all material has been collected from the C3, press the "STOP" button, and return the air pressure to 0 psi.

19) Remove the sample cylinder, and clean the inside thoroughly with a solvent compatible with your sample (e.g., water, soapy water, ethanol, or methanol). Also, wipe the rubber seal for the sample cylinder fitting as well as the outlet tubing with appropriate solvent. Re-attach the sample cylinder to the C3.

20) Load ~100 mL of cleaning solvent into the sample cylinder. Prime the pump with cleaning solvent. Run cleaning solvent for several strokes at 0 psi, then increase the air pressure until the homogenization pressure is equal to or greater than the homogenization pressure used for the sample. Wait for 10-20 strokes, then decrease the air pressure back to 0 psi. Repeat this procedure several times in order to flush the sample out of all orifices and seals.

21) Repeat step 20 as needed until the cleaning solvent coming out of the outlet tubing is transparent. Perform a final wash through with ethanol, and leave ~5-10 mL of ethanol in the homogenizer. This will prevent the pump from locking due to fouling or solidification of any material in the homogenizer.

Shutting down the C3:

22) Turn the "AIR REGULATOR" knob until the "AIR PRESSURE" and homogenization pressure gauges both read 0 psi.

23) Turn the yellow power knob on the back of the C3 to the horizontal "OFF" position. After several seconds, the red "STOP" button on the front of the C3 should go out.

24) Close the high pressure air supply valve. Make sure that the pressure gauge on the air manifold goes all the way to 0 psi.

A.9 Extracting Particle Dynamics from Video Microscopy Data

I used MATLAB code written by Maria Kilfoil to find and track round features (typical of spheres and discs). Here are some websites that might be helpful for understanding what the code is doing:

3D particle tracking using IDL -- John C. Crocker and Eric R. Weeks
http://www.physics.emory.edu/faculty/weeks//idl/three.html

Kilfoil Lab - software research tools
http://people.umass.edu/kilfoil/downloads.html

APPENDIX B

Miscellaneous Preliminary Data

In this section, I will present bits and pieces of interesting data from some preliminary experiments, and at the same time, highlight some experimental difficulties and provide potential solutions or suggestions on how to move forward.

B.1 *In Vivo* Distribution of Cylindrical Particles

I collaborated with Dr. Katherine Whitehead (a former post-doc from the Anderson Group) on *in vivo* biodistribution experiments in mice. I synthesized cylindrical hydrogel particles, 16 μm in diameter and 27 μm in height (Fig. B.1)

The particles are composed of 20% PEG-DA700, 44% PEG200, 15% Darocur® 1173, 11% 3x TE buffer and 10% rhodamine-acrylate (stock concentration = 10 mg/mL PEG200), by volume. Note that the fluorescence signal of the particles increases linearly with the amount of dye present in the prepolymer. I tried to add as much as 15% rhodamine-acrylate in order to maximize the particle brightness for tracking.

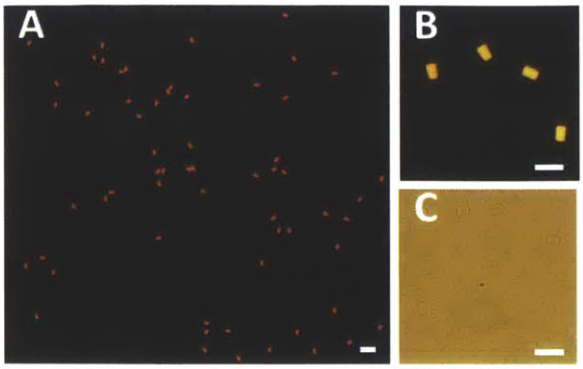

Figure B.1 – (A)-(B) Fluorescence and (C) bright-field images of cylindrical hydrogel particles, 16 μm (diameter) by 27 μm (height), synthesized using SFL. Scale bars are 50 μm.

Katie injected the particles into the tail veins of several mice and tracked them over time using an IVIS Spectrum whole-body imaging system. The particles mostly accumulated in the lymph nodes, which is likely due to uptake by macrophages or other immune cells (Fig. B.2). Much work still remains to be done to understand shape, aspect ratio, and surface charge effects on particle dissemination.

Generally, in order to obtain measurable signals using IVIS, a rule of thumb is that there needs to be at least *~1 nmol* of conjugated dye. For the cylindrical particles I synthesized, this corresponds to roughly ~500,000 counts (or ~10-20 hours of continuous polymerization using SFL). Therefore, flow lithography under contact mode may be a better alternative to traditional SFL, since throughput scales as the area available for polymerization. *In vivo* experiments in the future should be conducted in triplicates to account for any inherent biological variability from one animal to the next.

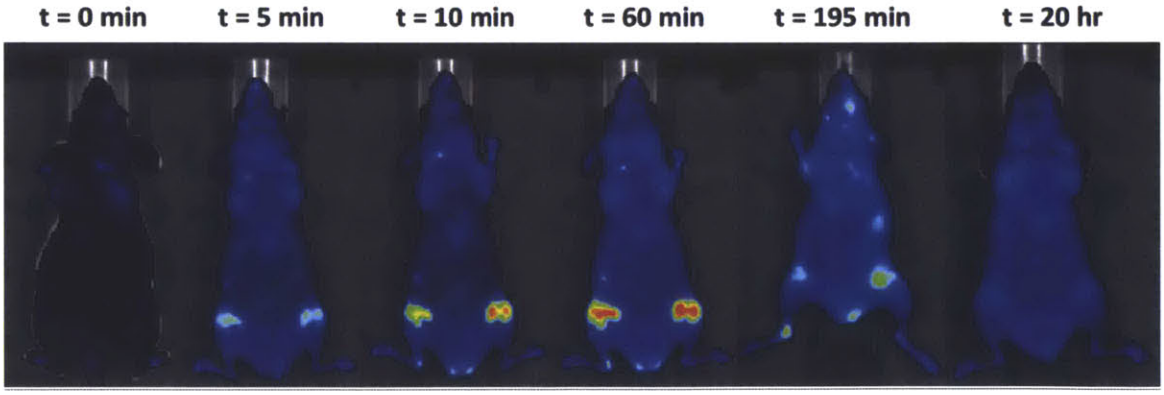

Figure B.2 – Representative time-lapsed whole-body images of a mouse before and after receiving an injection of a small dose of rhodamine-labeled cylindrical particles.

B.2 Flow Testing Microparticles with Complex Polymeric Architectures

As a direct extension of the work on red blood cell particle-mimics, I started to examine the molecular weight effect (i.e. contour length, L) of 2 μm thick (feature width) x 2 μm tall (height)

particles (Fig. B.3). The canonical prepolymer formation contains 20% PEG-DA700, 44% PEG200, 15% Darocur® 1173 and 1% rhodamine-acrylate, by volume. The elementary repeating unit is in the shape of an 'S', which has previously been shown to be particularly flexible. The critical pressure differential (at which 50% of the particle would pass through the contraction) grew approximately as $\sim L^4$.

Figure B.3 – Bright-field and fluorescent (upper inset) images of S-shaped hydrogel particles (feature width for these particles is 2 μm). The photo-mask used in each experiment is shown in the lower inset. Scale bars are 10 μm and 25 μm (upper inset).

A dimensional analysis of the magnitude of the competing elastic and hydrodynamic forces yields valuable information on effect of various experimental parameters (such as particle and channel geometry) on particle deformation in flow. The elastic force scales as $F_{el} \sim EI/L^2$, where L is the contour length of the particle, E is the Young's modulus, $I = \int x^2\, dA$ is the moment of inertia of the cross section; it is an area-weighted integral of the squared distance from an axis. Since the particles have rectangular cross sections (perpendicular to the flow direction) of dimensions h and b, $I \sim h^3 b$. In other words, there is a preferred bending direction. A macroscopic example of this phenomenon involves the bending of a ruler, an action which can be accomplished much more readily widthwise (along the shorter dimension) than lengthwise (along the longer dimension).

The hydrodynamic drag forces exerted by the moving fluid on the particles scales linearly with velocity, $F_d \sim \gamma v$, where $\gamma \sim \mu L$ is the drag coefficient, μ is the fluid viscosity and v is the characteristic velocity. Taking the ratio of the two forces, F_{el} and F_d, one obtains a key dimensionless group, S (which is related to the Sperm number, Sp):

$$S = \frac{\mu v L^3}{E h^3 b}$$

Therefore, it is clear that particles with micrometer-sized features will undergo large deformations in flow. Preliminary flow experiments show that ~1 μm tall discs (diameter = 8 μm) synthesized using oxygen-controlled SFL require much lower driving pressure to pass through 4 μm x 4 μm contractions than their ~2 μm tall counterparts. The numerical results are in qualitative agreement with theory (note the cubic dependence of S on h).

B.3 Depletion-driven Assembly of Non-spherical Colloids

I briefly studied the aggregation of non-spherical colloidal particles in dilute aqueous dispersion, induced by surfactant micelles. By adjusting the micelle concentration, which controls the strength of the short-ranged (~size of the micelle) depletion attraction, particles can potentially aggregate to give rise to unique anisotropic macrostructures.

I suspended ~ 100,000 platelet (~1 μm tall) particles in a sealed observation chamber (see section 3.3.3.1 for chamber construction protocol) containing ~500 mM SDS (>> CMC). The particles were synthesized using 7.5% O_2. I imaged the sample periodically. Number of particle clusters didn't noticeably increase over the course of 3 days. Beyond that, drying became an issue. Under these conditions, the interaction energy, which can be easily estimated for flat interfaces (see [174], for example), is much greater than kT for all dimers observed (Fig. B.6C-E). Note that 3 μm diameter PS microspheres aggregated within minutes under these conditions.

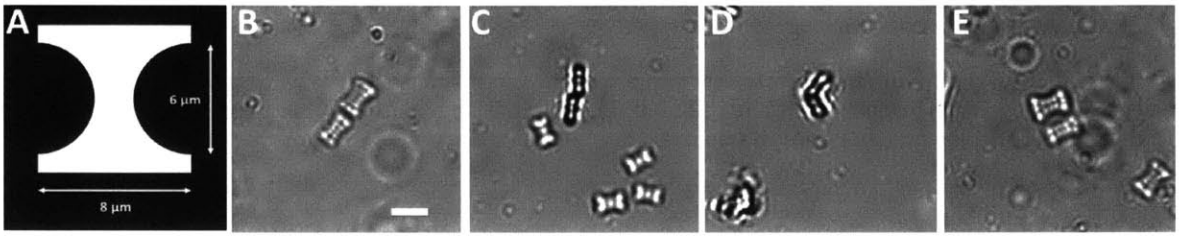

Figure B.4 – Depletion-driven assembly of colloidal platelet particles. (A) Photomask used during particle synthesis. (B)-(E) Bright-field images of platelet dimers, arranged in approximate order of decreasing interaction energy. The dimers formed in the presence of surfactant micelles. Scale bar is 10 μm.

I suspect the lack of large-scale clustering of particles can be partially attributed to insufficient particle count. In addition, SDS may not be the best depletant/crowder (i.e., too small) to use in this situation, since depletion forces could be attenuated by roughness on the particle surface [175]. Other possible choices include Ficoll (a mixture of nonionic polymers), dextran (commonly used to induce aggregation of red blood cells, e.g., [176], and high molecular weight PEG.

APPENDIX C

Effective Oxygen Diffusivity: Model Derivation

We use a simple mean-field approach to find the effective diffusivity of oxygen, D, in a dilute oil-in-water emulsion. D captures the O_2 mass transport that occurs on a length scale much greater than the distance between neighboring oil droplets, and allows us to treat a heterogeneous suspension as a homogeneous composite material.

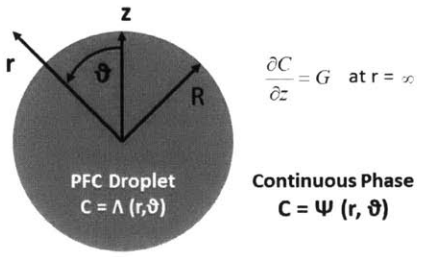

Figure C.1 – Model setup. A perfluorocarbon oil droplet of radius R is dispersed in a semi-infinite continuous phase. C denotes the oxygen concentration everywhere in this problem. There is a constant oxygen concentration gradient far from the droplet as a result of the radical polymerization reaction in SFL.

We derive D from the disturbance in the O_2 concentration field far away from an oil droplet. **Fig. C.1** shows the model geometry: a perfluorocarbon oil droplet is surrounded by an aqueous continuous phase. The oxygen concentration C, is broken down into two distinct regions, separated by the droplet interface.

In spherical coordinates with the origin situated at the center of the droplet, the field variables inside and outside the droplet, respectively, are:

$$\Lambda = f(r, \theta)$$

$$\psi = g(r, \theta)$$

We can write mass conservation equations for O_2 in this system at steady-state, without any volumetric reaction (consumption) terms as:

$$\frac{\partial}{\partial r}\left(r^2 \frac{\partial \Lambda}{\partial r}\right) + \frac{1}{\sin\,\theta}\frac{\partial}{\partial \theta}\left(\sin\,\theta \frac{\partial \Lambda}{\partial \theta}\right) = 0$$

$$\frac{\partial}{\partial r}\left(r^2 \frac{\partial \psi}{\partial r}\right) + \frac{1}{\sin\,\theta}\frac{\partial}{\partial \theta}\left(\sin\,\theta \frac{\partial \psi}{\partial \theta}\right) = 0$$

This set of PDEs captures the diffusive mass transfer after particle gelation has occurred during stop-flow lithography. To expedite the solution procedure, it is easier to make a variable change from θ to η:

$$\eta = \cos\theta$$

η varies from -1 (when θ=180°) to 1 (when θ=0°). The two PDEs above can then be re-written as:

$$\frac{\partial}{\partial r}\left(r^2 \frac{\partial \Lambda}{\partial r}\right) + \frac{\partial}{\partial \eta}\left((1-\eta^2) \frac{\partial \Lambda}{\partial \eta}\right) = 0$$

$$\frac{\partial}{\partial r}\left(r^2 \frac{\partial \psi}{\partial r}\right) + \frac{\partial}{\partial \eta}\left((1-\eta^2) \frac{\partial \psi}{\partial \eta}\right) = 0$$

Subject to the following four boundary conditions:

At $r = R$, continuity in O_2 concentration and flux dictates:

$$\Lambda(R, \eta) = K\psi(R, \eta)$$

where K is the partition coefficient; and

$$D_{PFC}\frac{\partial}{\partial r}\Lambda(R, \eta) = D_0 \frac{\partial}{\partial r}\psi(R, \eta)$$

Let $\beta = D_{PFC}/D_0$.

At the droplet center ($r = 0$):

$$\Lambda(0, \eta) = finite$$

And finally, far away from the droplet ($r = \infty$), there is a constant concentration gradient (due to the polymerization reaction, i.e. bulk consumption of O_2 in the microfluidic device):

$$\frac{\partial}{\partial z}\psi(\infty, \eta) = G$$

Or equivalently, since $z = r\cos\theta = r\,\eta$:

$$\frac{\partial}{\partial r}\psi(\infty,\eta) = G\eta$$

Using the Finite Fourier Transform (FFT) method, and η as the (only) finite dimension, we can transform the governing equations term-by-term using:

$$\Lambda_n = \int_{-1}^{1} \Phi_n(\eta)\Lambda(r,\eta)d\eta$$

$$\psi_n = \int_{-1}^{1} \Phi_n(\eta)\psi(r,\eta)d\eta$$

with $\Phi_n(\eta)$ as the basis functions obtained from Legendre polynomials. Transforming the second-derivative term in r is straightforward, but the term associated with η requires using integration by parts:

$$\int_{-1}^{1} \Phi_n \frac{\partial}{\partial\eta}\left((1-\eta^2)\frac{\partial\Lambda}{\partial\eta}\right)d\eta = (1-\eta^2)(\Phi_n\frac{\partial\Lambda}{\partial\eta} - \Lambda\frac{\partial\Phi_n}{\partial\eta})\Big|_{\eta=-1}^{\eta=1} - n(n+1)\Lambda_n$$

where n = 0, 1, 2... . $n(n+1)$ is the eigenvalues associated with the FFT problem in η.

The transformed governing equations are therefore:

$$\frac{d}{dr}\left(r^2\frac{d\Lambda_n}{dr}\right) - n(n+1)\Lambda_n = 0$$

$$\frac{d}{dr}\left(r^2\frac{d\psi_n}{dr}\right) - n(n+1)\psi_n = 0$$

These are ordinary, second-order differential equations with a generic solution of the form:

$$\Lambda_n = r^m$$

Substituting this into the transformed concentration equation above, we get a quadratic characteristic equation:

$$m^2 + m - n(n+1) = 0$$

which when solved, we obtain:

$$m = n \qquad \text{or} \qquad m = -(n+1)$$

In other words, the general solution for the concentration inside the droplet is:

$$\Lambda_n = A_n r^n + B_n r^{-(n+1)} \qquad\qquad \text{n = 0, 1, 2...}$$

where A_n and B_n are series of constants we need to determine using the boundary conditions. Since $[O_2]$ must be finite at the center of the droplet, B_n = 0.

Similarly, for the continuous phase:

$$\psi_n = C_n r^n + D_n r^{-(n+1)} \qquad n = 0, 1, 2...$$

To find A_n, C_n, and D_n, we start by transforming the BC far away at $r = \infty$,

$$\frac{d}{dr}\psi_n(\infty) = \int_{-1}^{1} \Phi_n(\eta)\frac{\partial}{\partial r}\psi(\infty,\eta)d\eta$$

$$\frac{d}{dr}\psi_n(\infty) = G\int_{-1}^{1} \Phi_n(\eta)\eta d\eta = \sqrt{2/3}\,G\int_{-1}^{1} \Phi_n(\eta)\sqrt{3/2}\,\eta d\eta$$

$$\frac{d}{dr}\psi_n(\infty) = \sqrt{2/3}\,G\delta_{n1}$$

In the last step, we invoked the orthogonality condition (i.e., only the first basis function is required to satisfy the concentration gradient far away). We can analytically express the gradient using the general solution for ψ_n as:

$$\frac{d\psi_n}{dr} = nC_n r^{n-1} - (n+1)D_n r^{-(n+2)}$$

For $n = 1$ and $r = \infty$:

$$C_1 = \sqrt{2/3}\,G$$

$C_n = 0$ for all $n \geq 2$.

From the BCs at $r = R$:

$$A_n R^n = K(C_n R^n + D_n R^{-(n+1)})$$

$$\beta\, nA_n R^{n-1} = nC_n R^{n-1} - (n+1)D_n R^{-(n+2)}$$

Solving this set of algebraic equations, we get:

$$A_0 = KC_0$$

$$A_1 = \left(\frac{3K}{2+\beta}\right)C_1$$

$$D_1 = \left(\frac{1-\beta}{2+\beta}\right)R^3 C_1$$

All other constants are zero. Assembling the overall concentration profile:

$$C(r,\eta) = \begin{cases} A(r,\eta) = \dfrac{KC_0}{\sqrt{2}} + \left(\dfrac{3K}{2+\beta}\right)Gr\eta & 0 \leq r \leq R \\ \psi(r,\eta) = \dfrac{C_0}{\sqrt{2}} + Gr\eta + \left(\dfrac{1-\beta}{2+\beta}\right)\dfrac{R^3}{r^2}G\eta & R < r < \infty \end{cases}$$

Replacing $C_0/\sqrt{2}$ with A, we arrive at Eq. (5.14). C_0 is an arbitrary constant since only a gradient BC is used in this problem. We can see from the expression for ψ, that a PFC droplet of radius R

will cause a dipolar disturbance, far away in the O_2 concentration in the surrounding fluid by an amount equal to C_p :

$$C_p(r) = \left(\frac{1-\beta}{2+\beta}\right)\frac{R^3}{r^2}G\eta$$

The total, additive perturbation, then due to a collection of droplets with a number density, n in an arbitrary spherical volume V, of radius a (where $a >> R$):

$$C_p^{total}(r) = nVR^3\left(\frac{1-\beta}{2+\beta}\right)\frac{G\eta}{r^2} = \varphi a^3\left(\frac{1-\beta}{2+\beta}\right)\frac{G\eta}{r^2}$$

where $\varphi = n\,{}^{4\pi}/_{3}\,R^3$ is the oil volume fraction.

Finally, to derive an expression for D, we compare the equation above with the analogous result obtained by assuming that V is occupied by a homogenous composite material, characterized by diffusivity parameter β'. According to the equation for C_p, a homogenous sphere of radius a will perturb the O_2 concentration in the surrounding fluid by:

$$C_p^{total}(r) = \left(\frac{1-\beta'}{2+\beta'}\right)\frac{a^3}{r^2}G\eta$$

We equate the two equations for C_p^{total} and solve for β':

$$\left(\frac{1-\beta'}{2+\beta'}\right) = \varphi\left(\frac{1-\beta}{2+\beta}\right)$$

Let B = $\left(\frac{1-\beta}{2+\beta}\right)$,

$$1-\beta' = \varphi B(2+\beta') = 2\varphi B + \varphi B\beta'$$

$$\beta' = \frac{-2\varphi B + 1}{\varphi B + 1}$$

Using Taylor expansion in φ, for a dilute emulsion:

$$\beta' = \frac{D}{D_0} = 1 - 3B\,\varphi + O(\varphi^2) = 1 - 3\left(\frac{1-\beta}{2+\beta}\right)\varphi + O(\varphi^2)$$

Slight rearrangement and ignoring higher order terms, yields Eq. (5.16).

$$D = D_0\left(1 + 3\left(\frac{\beta-1}{\beta+2}\right)\varphi\right)$$

Bibliography

1. Duncanson, W.J., et al., *Microfluidic synthesis of advanced microparticles for encapsulation and controlled release.* Lab Chip, 2012. **12**(12): p. 2135.
2. Pregibon, D.C. and P.S. Doyle, *Optimization of Encoded Hydrogel Particles for Nucleic Acid Quantification.* Anal. Chem., 2009. **81**(12): p. 4873.
3. Pregibon, D.C., M. Toner, and P.S. Doyle, *Multifunctional encoded particles for high-throughput biomolecule analysis.* Science, 2007. **315**(5817): p. 1393.
4. Mitragotri, S. and J. Lahann, *Physical approaches to biomaterial design.* Nature Materials, 2009. **8**(1): p. 15.
5. Shemin, D. and D. Rittenberg, *The life span of the human red blood cell.* J. Biol. Chem., 1946. **166**(2): p. 627.
6. Haghgooie, R., M. Toner, and P.S. Doyle, *Squishy Non-Spherical Hydrogel Microparticles.* Macromol. Rapid Commun., 2010. **31**(2): p. 128.
7. Doshi, N., et al., *Red blood cell-mimicking synthetic biomaterial particles.* PNAS, 2009. **106**(51): p. 21495.
8. Merkel, T.J., et al., *Using mechanobiological mimicry of red blood cells to extend circulation times of hydrogel microparticles.* PNAS, 2011. **108**(2): p. 586.
9. Kozlovskaya, V., et al., *Internalization of Red Blood Cell-Mimicking Hydrogel Capsules with pH-Triggered Shape Responses.* ACS Nano, 2014. **8**(6): p. 5725.
10. Geng, Y., et al., *Shape effects of filaments versus spherical particles in flow and drug delivery.* Nat Nanotechnol, 2007. **2**(4): p. 249.
11. Yoo, J.W., et al., *Bio-inspired, bioengineered and biomimetic drug delivery carriers.* Nature Reviews Drug Discovery, 2011. **10**(7): p. 521.
12. Sacanna, S., et al., *Shaping colloids for self-assembly.* Nat Commun, 2013. **4**: p. 1688.
13. Discher, D.E. and F. Ahmed, *Polymersomes.* Annu Rev Biomed Eng, 2006. **8**: p. 323.
14. Rolland, J.P., et al., *Direct Fabrication and Harvesting of Monodisperse, Shape-Specific Nanobiomaterials.* JACS, 2005. **127**(28): p. 10096.

15. Bhaskar, S., et al., *Towards Designer Microparticles: Simultaneous Control of Anisotropy, Shape, and Size.* Small, 2010. **6**(3): p. 404.
16. Shah, R.K., et al., *Designer emulsions using microfluidics.* Mater. Today, 2008. **11**(4): p. 18.
17. Kozlovskaya, V., et al., *Shape switching of hollow layer-by-layer hydrogel microcontainers.* Chem. Commun., 2011. **47**(29): p. 8352.
18. Helgeson, M.E., S.C. Chapin, and P.S. Doyle, *Hydrogel microparticles from lithographic processes: novel materials for fundamental and applied colloid science.* Curr Opin Colloid Interface Sci, 2011. **16**(2): p. 106.
19. Hernandez, C.J. and T.G. Mason, *Colloidal Alphabet Soup: Monodisperse Dispersions of Shape-Designed LithoParticles.* The Journal of Physical Chemistry C, 2007. **111**(12): p. 4477.
20. Wang, Y.P., et al., *Generation of a Library of Particles Having Controlled Sizes and Shapes via the Mechanical Elongation of Master Templates.* Langmuir, 2011. **27**(2): p. 524.
21. Champion, J.A., Y.K. Katare, and S. Mitragotri, *Making polymeric micro- and nanoparticles of complex shapes.* PNAS, 2007. **104**(29): p. 11901.
22. Choi, C.H., et al., *Surface-tension-induced synthesis of complex particles using confined polymeric fluids.* Angew. Chemie., 2010. **49**(42): p. 7748.
23. Shum, H.C., J.W. Kim, and D.A. Weitz, *Microfluidic fabrication of monodisperse biocompatible and biodegradable polymersomes with controlled permeability.* JACS, 2008. **130**(29): p. 9543.
24. Dendukuri, D., et al., *Continuous-flow lithography for high-throughput microparticle synthesis.* Nature Materials, 2006. **5**(5): p. 365.
25. Dendukuri, D., et al., *Stop-flow lithography in a microfluidic device.* Lab Chip, 2007. **7**(7): p. 818.
26. Panda, P., et al., *Stop-flow lithography to generate cell-laden microgel particles.* Lab on a Chip, 2008. **8**: p. 1056.
27. Ramin, H., T. Mehmet, and S.D. Patrick, *Squishy non-spherical hydrogel microparticles.* Macromol. Rapid Commun., 2010. **31**(2): p. 128.
28. Bong, K.W., S.C. Chapin, and P.S. Doyle, *Magnetic barcoded hydrogel microparticles for multiplexed detection.* Langmuir, 2010.
29. Hwang, D.K., et al., *Stop-flow lithography for the production of shape-evolving degradable microgel particles.* JACS, 2009. **131**(12): p. 4499.
30. Diao, Y., et al., *Gel-induced selective crystallization of polymorphs.* JACS., 2012. **134**(1): p. 673.
31. Panda, P., et al., *Stop-flow lithography to generate cell-laden microgel particles.* Lab Chip, 2008. **8**(7): p. 1056.
32. Tan, W.S., et al., *Hierarchical assembly of viral nanotemplates with encoded microparticles via nucleic acid hybridization.* Langmuir, 2008. **24**(21): p. 12483.
33. Bong, K.W., S.C. Chapin, and P.S. Doyle, *Magnetic barcoded hydrogel microparticles for multiplexed detection.* Langmuir, 2010. **26**(11): p. 8008.
34. Hwang, D.K., et al., *Stop-flow lithography for the production of shape-evolving degradable microgel particles.* JACS., 2009. **131**(12): p. 4499.
35. Shepherd, R.F., et al., *Stop-Flow Lithography of Colloidal, Glass, and Silicon Microcomponents.* Adv. Mater., 2008. **20**(24): p. 4734.
36. Suh, S.K., et al., *Synthesis of nonspherical superparamagnetic particles: in situ coprecipitation of magnetic nanoparticles in microgels prepared by stop-flow lithography.* JACS, 2012. **134**(17): p. 7337.
37. Dendukuri, D., et al., *Modeling of Oxygen-Inhibited Free Radical Photopolymerization in a PDMS Microfluidic Device.* Macromolecules, 2008. **41**(22): p. 8547.
38. Cheng, Y., et al., *Bioinspired Multicompartmental Microfibers from Microfluidics.* Adv. Mater., 2014.
39. Bhaskar, S., et al., *Multicompartmental microcylinders.* Angew. Chemie., 2009. **48**(25): p. 4589.
40. Bong, K.W., et al., *Hydrodynamic Focusing Lithography.* Angewandte Chemie., 2010. **49**(1): p. 87.
41. Dendukuri, D., et al., *Continuous-flow lithography for high-throughput microparticle synthesis.* Nature Materials, 2006. **5**(5): p. 365.

42. Jagadeesan, D., et al., *Microgels for the encapsulation and stimulus-responsive release of molecules with distinct polarities.* Macromol Biosci, 2011. **11**(7): p. 889.
43. Adams, L.L.A., et al., *Single step emulsification for the generation of multi-component double emulsions.* Soft Matter, 2012. **8**(41): p. 10719.
44. Kim, S.-H. and D.A. Weitz, *One-Step Emulsification of Multiple Concentric Shells with Capillary Microfluidic Devices.* Angew. Chemie., 2011. **50**(37): p. 8731.
45. Choi, C.-H., D.A. Weitz, and C.-S. Lee, *One Step Formation of Controllable Complex Emulsions: From Functional Particles to Simultaneous Encapsulation of Hydrophilic and Hydrophobic Agents into Desired Position.* Adv. Mater., 2013. **25**(18): p. 2536.
46. McClements, D.J. and J. Rao, *Food-grade nanoemulsions: formulation, fabrication, properties, performance, biological fate, and potential toxicity.* Crit. Rev. Food Sci. Nutr., 2011. **51**(4): p. 285.
47. Srinivas, R.L., S.C. Chapin, and P.S. Doyle, *Aptamer-functionalized microgel particles for protein detection.* Anal. Chem., 2011. **83**(23): p. 9138.
48. An, H.Z., et al., *Synthesis of biomimetic oxygen-carrying compartmentalized microparticles using flow lithography.* Lab Chip, 2013. **13**(24): p. 4765.
49. Chen, K., et al., *Low Modulus Biomimetic Microgel Particles with High Loading of Hemoglobin.* Biomacromolecules, 2012. **13**(9): p. 2748.
50. Modery-Pawlowski, C.L., et al., *Approaches to synthetic platelet analogs.* Biomaterials, 2013. **34**(2): p. 526.
51. Doshi, N., et al., *Platelet Mimetic Particles for Targeting Thrombi in Flowing Blood.* Adv. Mater., 2012. **24**(28): p. 3864.
52. An, H.Z., M.E. Helgeson, and P.S. Doyle, *Nanoemulsion Composite Microgels for Orthogonal Encapsulation and Release.* Adv. Mat., 2012. **24**(28): p. 3838.
53. Kim, S.H., et al., *Multiple Polymersomes for Programmed Release of Multiple Components.* JACS, 2011. **133**(38): p. 15165.
54. Champion, J.A., A. Walker, and S. Mitragotri, *Role of particle size in phagocytosis of polymeric microspheres.* Pharm. Res., 2008. **25**(8): p. 1815.
55. Merkel, T.J., et al., *The effect of particle size on the biodistribution of low-modulus hydrogel PRINT particles.* J. Controlled Release, 2012. **162**(1): p. 37.
56. Champion, J.A., Y.K. Katare, and S. Mitragotri, *Particle shape: A new design parameter for micro- and nanoscale drug delivery carriers.* J. Controlled Release, 2007. **121**(1-2): p. 3.
57. Kolhar, P. and S. Mitragotri, *Polymer Microparticles Exhibit Size and Shape Dependent Accumulation around the Nucleus after Endocytosis.* Adv. Funct. Mater., 2012. **22**(18): p. 3759.
58. Yoo, J.W., N. Doshi, and S. Mitragotri, *Endocytosis and Intracellular Distribution of PLGA Particles in Endothelial Cells: Effect of Particle Geometry.* Macromol. Rapid Commun., 2010. **31**(2): p. 142.
59. Herlihy, K., et al., *Soft Lithography-Based Hydrogel Particles and the Effect of Shape and Size on Biodistribution.* Nanotech Conference & Expo 2009, Vol 2, Technical Proceedings, 2009: p. 60.
60. Shum, H.C., et al., *Droplet Microfluidics for Fabrication of Non-Spherical Particles.* Macromol. Rapid Commun., 2010. **31**(2): p. 108.
61. Appleyard, D.C., et al., *Bar-coded hydrogel microparticles for protein detection: synthesis, assay and scanning.* Nat Protoc, 2011. **6**(11): p. 1761.
62. Bong, K.W., et al., *Compressed-air flow control system.* Lab on a Chip, 2011. **11**(4): p. 743.
63. Ramamoorthy, R., P.K. Dutta, and S.A. Akbar, *Oxygen sensors: Materials, methods, designs and applications.* Journal of Materials Science, 2003. **38**(21): p. 4271.
64. Papkovsky, D.B. and R.I. Dmitriev, *Biological detection by optical oxygen sensing.* Chem. Soc. Rev., 2013. **42**: p. 8700.
65. Shiku, H., et al., *Oxygen permeability of surface-modified poly(dimethylsiloxane) characterized by scanning electrochemical microscopy.* Chem. Lett., 2006. **35**(2): p. 234.
66. Brandao, L., L.M. Madeira, and A.M. Mendes, *Mass transport on composite dense PDMS membranes with palladium nanoclusters.* J. Membr. Sci., 2007. **288**(1-2): p. 112.
67. Denn, M.M., *Process fluid mechanics.* 1980, Prentice-Hall.
68. Whisler, J.A., M.B. Chen, and R.D. Kamm, *Control of Perfusable Microvascular Network Morphology Using a Multiculture Microfluidic System.* Tissue Eng Part C Methods, 2013. **20**(7): p. 543.

69. Chen, M.B., et al., *Mechanisms of tumor cell extravasation in an in vitro microvascular network platform.* Integr Biol (Camb), 2013. **5**(10): p. 1262.
70. Bow, H., et al., *A microfabricated deformability-based flow cytometer with application to malaria.* Lab Chip, 2011. **11**(6): p. 1065.
71. Pelletier, V., et al., *Microrheology of microtubule solutions and actin-microtubule composite networks.* Phys Rev Lett, 2009. **102**(18): p. 188303.
72. Savin, T. and P.S. Doyle, *Static and dynamic errors in particle tracking microrheology.* Biophys. J., 2005. **88**(1): p. 623.
73. Eral, H.B., et al., *Biocompatible Alginate Microgel Particles as Heteronucleants and Encapsulating Vehicles for Hydrophilic and Hydrophobic Drugs.* Cryst Growth Des, 2014. **14**(4): p. 2073.
74. Suh, S.K., et al., *Using stop-flow lithography to produce opaque microparticles: synthesis and modeling.* Langmuir, 2011. **27**(22): p. 13813.
75. Kızılel, S., V.H. Pérez-Luna, and F. Teymour, *Mathematical Model for Surface-Initiated Photopolymerization of Poly(ethylene glycol) Diacrylate.* Macromol. Theory Simul., 2006. **15**(9): p. 686.
76. Decker, C. and A.D. Jenkins, *Kinetic approach of oxygen inhibition in ultraviolet- and laser-induced polymerizations.* Macromolecules, 1985. **18**(6): p. 1241.
77. Lin, H. and B.D. Freeman, *Gas Permeation and Diffusion in Cross-Linked Poly(ethylene glycol diacrylate).* Macromolecules, 2006. **39**(10): p. 3568.
78. Lecamp, L., et al., *Influence of UV radiation wavelength on conversion and temperature distribution profiles within dimethacrylate thick material during photopolymerization.* Polymer, 2001. **42**(21): p. 8541.
79. Goodner, M.D. and C.N. Bowman, *Development of a comprehensive free radical photopolymerization model incorporating heat and mass transfer effects in thick films.* Chem. Eng. Sci., 2002. **57**(5): p. 887.
80. Park, S., et al., *Controlling uniformity of photopolymerized microscopic hydrogels.* Lab Chip, 2014. **14**(9): p. 1551.
81. Gervais, T., et al., *Flow-induced deformation of shallow microfluidic channels.* Lab Chip, 2006. **6**(4): p. 500.
82. Crocker, J.C. and B.D. Hoffman, *Multiple-particle tracking and two-point microrheology in cells.* Method Cell Biol, 2007. **83**: p. 141.
83. Hansen, S., *Translational friction coefficients for cylinders of arbitrary axial ratios estimated by Monte Carlo simulation.* J. Chem. Phys., 2004. **121**(18): p. 9111.
84. Ortega, A. and J.G. de la Torre, *Hydrodynamic properties of rodlike and disklike particles in dilute solution.* J. Chem. Phys., 2003. **119**(18): p. 9914.
85. Huang, P. and K.S. Breuer, *Direct measurement of anisotropic near-wall hindered diffusion using total internal reflection velocimetry.* Phys Rev E, 2007. **76**(4) 046307.
86. Sacanna, S., et al., *Lock and key colloids.* Nature, 2010. **464**(7288): p. 575.
87. Chakrabarty, A., et al., *Brownian motion of boomerang colloidal particles.* Phys Rev Lett, 2013. **111**(16): p. 160603.
88. Kim, M.U., et al., *Hydrodynamic force on a plate near the plane wall. Part I: plate in sliding motion.* Fluid Dyn Res, 2001. **29**(3): p. 137.
89. Flicker, S.G., J.L. Tipa, and S.G. Bike, *Quantifying Double-Layer Repulsion between a Colloidal Sphere and a Glass Plate Using Total Internal-Reflection Microscopy.* J. Colloid Interface Sci., 1993. **158**(2): p. 317.
90. Bevan, M.A. and D.C. Prieve, *Hindered diffusion of colloidal particles very near to a wall: Revisited.* J. Chem. Phys., 2000. **113**(3): p. 1228.
91. Merkel, T.J., et al., *Using mechanobiological mimicry of red blood cells to extend circulation times of hydrogel microparticles.* PNAS, 2011. **108**(2): p. 586.
92. Mitragotri, S. and J. Lahann, *Physical approaches to biomaterial design.* Nat Mater, 2009. **8**(1): p. 15.
93. Hoare, T.R. and D.S. Kohane, *Hydrogels in drug delivery: Progress and challenges.* Polymer, 2008. **49**(8): p. 1993.

94. Kolishetti, N., et al., *Engineering of self-assembled nanoparticle platform for precisely controlled combination drug therapy.* PNAS., 2010. **107**(42): p. 17939.
95. Helgeson, M.E., et al., *Mesoporous organohydrogels from thermogelling photocrosslinkable nanoemulsions.* Nature Materials, 2012. **11**(4): p. 344.
96. Peppas, N.A., et al., *Hydrogels in pharmaceutical formulations.* Eur. J. Pharm. Biopharm., 2000. **50**(1): p. 27.
97. Hoffman, A.S., *Hydrogels for biomedical applications.* Adv. Drug Del. Rev., 2002. **54**(1): p. 3.
98. Muller-Goymann, C.C., *Physicochernical characterization of colloidal drug delivery systems such as reverse micelles, vesicles, liquid crystals and nanoparticles for topical administration.* Eur. J. Pharm. Biopharm., 2004. **58**(2): p. 343.
99. McClements, D.J., *Edible nanoemulsions: fabrication, properties, and functional performance.* Soft Matter, 2011. **7**(6): p. 2297.
100. Couture, O., et al., *Ultrasound internal tattooing.* Med. Phys., 2011. **38**(2): p. 1116.
101. Jeong, B., Y.H. Bae, and S.W. Kim, *Drug release from biodegradable injectable thermosensitive hydrogel of PEG-PLGA-PEG triblock copolymers.* J. Controlled Release, 2000. **63**(1-2): p. 155.
102. Langer, R. and D.A. Tirrell, *Designing materials for biology and medicine.* Nature, 2004. **428**(6982): p. 487.
103. Jenning, V., et al., *Vitamin A loaded solid lipid nanoparticles for topical use: occlusive properties and drug targeting to the upper skin.* Eur. J. Pharm. Biopharm., 2000. **49**(3): p. 211.
104. Chen, P.C., et al., *Injectable microparticle-gel system for prolonged and localized lidocaine release. II. In vivo anesthetic effects.* Journal of Biomedical Materials Research Part A, 2004. **70A**(3): p. 459.
105. Gao, X.Y., et al., *The growth of complex nanostructures: Synergism of dipolar force and stacking-defects in anisotropic self-assembly.* Adv. Mater., 2008. **20**(9): p. 1794.
106. Gulsen, D., C.C. Li, and A. Chauhan, *Dispersion of DMPC liposomes in contact lenses for ophthalmic drug delivery.* Curr. Eye Res., 2005. **30**(12): p. 1071.
107. Yan, H. and K. Tsujii, *Potential application of poly(N-isopropylacrylamide) gel containing polymeric micelles to drug delivery systems.* Colloids and Surfaces B-Biointerfaces, 2005. **46**(3): p. 142.
108. Lapitsky, Y. and E.W. Kaler, *Surfactant and polyelectrolyte gel particles for encapsulation and release of aromatic oils.* Soft Matter, 2006. **2**(9): p. 779.
109. Gulsen, D. and A. Chauhan, *Dispersion of microemulsion drops in HEMA hydrogel: a potential ophthalmic drug delivery vehicle.* Int. J. Pharm., 2005. **292**(1-2): p. 95.
110. McClements, D.J., *Emulsion Design to Improve the Delivery of Functional Lipophilic Components*, in *Annual Review of Food Science and Technology, Vol 1*, M.P. Doyle and T.R. Klaenhammer, Editors. 2010. p. 241.
111. Meleson, K., S. Graves, and T.G. Mason, *Formation of Concentrated Nanoemulsions by Extreme Shear.* Soft Materials, 2004. **2**(2-3): p. 109.
112.Geng, Y. and D.E. Discher, *Visualization of degradable worm micelle breakdown in relation to drug release.* Polymer, 2006. **47**(7): p. 2519.
113. Discher, B.M., et al., *Polymer vesicles in various media.* Current Opinion in Colloid & Interface Science, 2000. **5**(1-2): p. 125.
114. Brackman, J.C. and J. Engberts, *Polymer micelle interactions - physical organic aspects.* Chem. Soc. Rev., 1993. **22**(2): p. 85.
115. Dendukuri, D. and P.S. Doyle, *The Synthesis and Assembly of Polymeric Microparticles Using Microfluidics.* Adv. Mater., 2009. **21**(41): p. 4071.
116. Bong, K.W., D.C. Pregibon, and P.S. Doyle, *Lock release lithography for 3D and composite microparticles.* Lab Chip, 2009. **9**(7): p. 863.
117. Appleyard, D.C., S.C. Chapin, and P.S. Doyle, *Multiplexed Protein Quantification with Barcoded Hydrogel Microparticles.* Anal. Chem., 2011. **83**(1): p. 193.
118. Kim, S.-H., et al., *Multiple Polymersomes for Programmed Release of Multiple Components.* JACS, 2011: p. doi:10.1021/ja205687k.
119. Sun, B.J., et al., *Microfluidic Melt Emulsification for Encapsulation and Release of Actives.* Acs Appl Mater Inter, 2010. **2**(12): p. 3411.

120. Jagadeesan, D., et al., *Microgels for the Encapsulapsulation and Stimulus-Responsive Release of Molecules with Distinct Polarities.* Macromol. Biosci., 2011. **11**(7): p. 889.
121. Kim, S.H., J.W. Shim, and S.M. Yang, *Microfluidic Multicolor Encoding of Microspheres with Nanoscopic Surface Complexity for Multiplex Immunoassays.* Angew. Chemie., 2011. **50**(5): p. 1171.
122. Chapin, S.C., et al., *Rapid microRNA Profiling on Encoded Gel Microparticles.* Angew. Chemie., 2011. **50**(10): p. 2289.
123. Mason, T.G., et al., *Nanoemulsions: formation, structure, and physical properties.* J Phys-Condens Mat, 2006. **18**(41): p. R635.
124. Shum, H.C., et al., *Multicompartment Polymersomes from Double Emulsions.* Angew. Chemie., 2011. **50**(7): p. 1648.
125. Jang, J.-H., et al., *A Route to Three-Dimensional Structures in a Microfluidic Device: Stop-Flow Interference Lithography.* Angew. Chemie., 2007. **46**(47): p. 9027.
126. Peppas, N.A., et al., *Hydrogels in biology and medicine: From molecular principles to bionanotechnology.* Adv. Mater., 2006. **18**(11): p. 1345.
127. Nie, S.M., et al., *Nanotechnology applications in cancer*, in *Annu. Rev. Biomed. Eng.* 2007. p. 257.
128. Davis, M.E., Z. Chen, and D.M. Shin, *Nanoparticle therapeutics: an emerging treatment modality for cancer.* Nature Reviews Drug Discovery, 2008. **7**(9): p. 771.
129. Brannon-Peppas, L. and J.O. Blanchette, *Nanoparticle and targeted systems for cancer therapy.* Adv. Drug Del. Rev., 2004. **56**(11): p. 1649.
130. Riess, J.G., *Understanding the Fundamentals of Perfluorocarbons and Perfluorocarbon Emulsions Relevant to In Vivo Oxygen Delivery.* Artif. Cells Blood Substit. Biotechnol., 2005. **33**(1): p. 47.
131. Kabalnov, A.S. and E.D. Shchukin, *Ostwald ripening theory: applications to fluorocarbon emulsion stability.* Adv. Colloid Interface Sci., 1992. **38**(0): p. 69.
132. Kabalnov, A., *Ostwald Ripening and Related Phenomena.* J. Dispersion Sci. Technol., 2001. **22**(1): p. 1.
133. Balmert, S.C. and S.R. Little, *Biomimetic Delivery with Micro- and Nanoparticles.* Adv. Mater., 2012. **24**(28): p. 3757.
134. Yoo, J.-W., et al., *Bio-inspired, bioengineered and biomimetic drug delivery carriers.* Nat Rev Drug Discov, 2011. **10**(7): p. 521.
135. Geng, Y., et al., *Shape effects of filaments versus spherical particles in flow and drug delivery.* Nat Nano, 2007. **2**(4): p. 249.
136. Champion, J.A., Y.K. Katare, and S. Mitragotri, *Making polymeric micro- and nanoparticles of complex shapes.* Proceedings of the National Academy of Sciences, 2007. **104**(29): p. 11901.
137. Bhaskar, S., et al., *Multicompartmental Microcylinders.* Angew. Chemie., 2009. **48**(25): p. 4589.
138. Champion, J.A., Y.K. Katare, and S. Mitragotri, *Particle shape: A new design parameter for micro- and nanoscale drug delivery carriers.* J. Controlled Release, 2007. **121**(1–2): p. 3.
139. Champion, J.A. and S. Mitragotri, *Role of target geometry in phagocytosis.* PNAS, 2006. **103**(13): p. 4930.
140. Wang, W., et al., *Controllable microfluidic production of multicomponent multiple emulsions.* Lab Chip, 2011. **11**(9): p. 1587.
141. Jagadeesan, D., et al., *Microgels for the Encapsulation and Stimulus-Responsive Release of Molecules with Distinct Polarities.* Macromolecular Bioscience, 2011. **11**(7): p. 889.
142. Choi, C.-H., D.A. Weitz, and C.-S. Lee, *One Step Formation of Controllable Complex Emulsions: From Functional Particles to Simultaneous Encapsulation of Hydrophilic and Hydrophobic Agents into Desired Position.* Adv. Mat., 2013: p. n/a.
143. Shah, R.K., et al., *Fabrication of monodisperse thermosensitive microgels and gel capsules in microfluidic devices.* Soft Matter, 2008. **4**(12): p. 2303.
144. Helgeson, M.E., et al., *Mesoporous organohydrogels from thermogelling photocrosslinkable nanoemulsions.* Nature Materials, 2012. **11**(4): p. 344.
145. Chu, L.-Y., et al., *Controllable Monodisperse Multiple Emulsions.* Angew. Chemie., 2007. **119**(47): p. 9128.

146. Amstad, E., S.-H. Kim, and D.A. Weitz, *Photo- and Thermoresponsive Polymersomes for Triggered Release.* Angew. Chemie., 2012. **51**(50): p. 12499.
147. Lowe, K.C., M.R. Davey, and J.B. Power, *Perfluorochemicals: their applications and benefits to cell culture.* Trends Biotechnol., 1998. **16**(6): p. 272.
148. Chin, K., et al., *Hydrogel-Perfluorocarbon Composite Scaffold Promotes Oxygen Transport to Immobilized Cells.* Biotechnol. Progr., 2008. **24**(2): p. 358.
149. Mason, T.G., et al., *Nanoemulsions: formation, structure, and physical properties.* Journal of Physics: Condensed Matter, 2006. **18**(41): p. R635.
150. Weers, J.G. and B.P.E. Binks, *Modern Aspects of Emulsion Science.* 1998: p. 292.
151. Delmas, T., et al., *How To Prepare and Stabilize Very Small Nanoemulsions.* Langmuir, 2011. **27**(5): p. 1683.
152. Weers, J.G. and R.A. Arlauskas, *Sedimentation Field-Flow Fractionation Studies of Ostwald Ripening in Fluorocarbon Emulsions Containing Two Disperse Phase Components.* Langmuir, 1995. **11**(2): p. 474.
153. Deen, W.M., *Analysis of Transport Phenomena.* Analysis of Transport Phenomena, 2012.
154. Maxwell, J.C., *Treatise on Electricity and Magnetism.* Treatise on Electricity and Magnetism, Vol. 1, 1954.
155. Fraker, C.A., et al., *Optimization of perfluoro nano-scale emulsions: The importance of particle size for enhanced oxygen transfer in biomedical applications.* Colloids Surf. B. Biointerfaces, 2012. **98**(0): p. 26.
156. Brown, R.B. and J. Audet, *Current techniques for single-cell lysis.* Journal of The Royal Society Interface, 2008. **5**(2): p. S131.
157. Rosen, M.J. and J.T. Kunjappu, *Surfactants and Interfacial Phenomena.* Surfactants and Interfacial Phenomena, 2012.
158. Riess, J.G., *Fluorocarbon-Based in vivo Oxygen Transport and Delivery Systems.* Vox Sang., 1991. **61**(4): p. 225.
159. DeRosa, M.C. and R.J. Crutchley, *Photosensitized singlet oxygen and its applications.* Coord. Chem. Rev., 2002. **233–234**(0): p. 351.
160. Gratton, S.E., et al., *The effect of particle design on cellular internalization pathways.* PNAS, 2008. **105**(33): p. 11613.
161. Yan, Y., M. Bjonmalm, and F. Caruso, *Assembly of Layer-by-Layer Particles and Their Interactions with Biological Systems.* Chem. Mater., 2014. **26**(1): p. 452.
162. Morton, S.W., et al., *Scalable Manufacture of Built-to-Order Nanomedicine: Spray-Assisted Layer-by-Layer Functionalization of PRINT Nanoparticles.* Adv. Mater., 2013. **25**(34): p. 4707.
163. De Geest, B.G., et al., *Self-rupturing and hollow microcapsules prepared from bio-polyelectrolyte-coated microgels.* Adv. Funct. Mater., 2007. **17**(4): p. 531.
164. Costa, E., et al., *Tuning Smart Microgel Swelling and Responsive Behavior through Strong and Weak Polyelectrolyte Pair Assembly.* Langmuir, 2012. **28**(26): p. 10082.
165. Pan, H.M., et al., *Inwards Interweaving of Polymeric Layers within Hydrogels: Assembly of Spherical Multi-Shells with Discrete Porosity Differences.* Adv. Funct. Mater., 2013. **23**(41): p. 5108.
166. Yashchenok, A., et al., *Polyelectrolyte multilayer microcapsules templated on spherical, elliptical and square calcium carbonate particles.* J Mater Chem B, 2013. **1**(9): p. 1223.
167. Lisunova, M., et al., *Assembly of the anisotropic microcapsules in aqueous dispersions.* Soft Matter, 2013. **9**(13): p. 3651.
168. Smith, D.E., H.P. Babcock, and S. Chu, *Single-Polymer Dynamics in Steady Shear Flow.* Science, 1999. **283**(5408): p. 1724.
169. Smith, D.E. and S. Chu, *Response of Flexible Polymers to a Sudden Elongational Flow.* Science, 1998. **281**(5381): p. 1335.
170. Tang, J., D.W. Trahan, and P.S. Doyle, *Coil and stretch transition of DNA molecules in slitlike confinement.* Macromolecules, 2010. **43**(6): p. 3081.
171. Pipe, C.J. and G.H. McKinley, *Microfluidic rheometry.* Mechanics Research Communications, 2009. **36**(1): p. 110.
172. Attia, R., et al., *Soft microflow sensors.* Lab Chip, 2009. **9**(9): p. 1213.

173. Beebe, D.J., et al., *Functional hydrogel structures for autonomous flow control inside microfluidic channels.* Nature, 2000. **404**(6778): p. 588.
174. Mason, T.G., *Osmotically driven shape-dependent colloidal separations.* Phys Rev E Stat Nonlin Soft Matter Phys, 2002. **66**(6 Pt 1): p. 060402.
175. Zhao, K. and T.G. Mason, *Directing colloidal self-assembly through roughness-controlled depletion attractions.* Phys. Rev. Lett., 2007. **99**(26).
176. Neu, B. and H.J. Meiselman, *Depletion-mediated red blood cell aggregation in polymer solutions.* Biophys. J., 2002. **83**(5): p. 2482.